
POLITECNICO DI MILANO
DEPARTMENT OF ELECTRONICS, INFORMATION AND BIOENGINEERING
DOCTORAL PROGRAMME IN INFORMATION TECHNOLOGY

---

# DEVELOPMENT AND APPLICATION OF A TEST SUITE FOR RADIATION DETECTORS CHARACTERIZATION OVER A WIDE RANGE OF CHARGE INJECTION LEVELS

Doctoral Dissertation of:
**Giuseppe Vito Montemurro**

Advisor:
**Prof. A. Castoldi**

Tutor:
**Prof. A. Geraci**

The Chair of the Doctoral Program:
**Prof. C. Fiorini**

2013 – XXVI

# Abstract

NEW techniques aimed at the direct characterization of the response of semiconductor detectors and of the associated front-end electronics are an essential factor for the successful development of a new generation of detection systems compatible, for example, with the present and future high brightness Free Electron Laser sources of X-rays because of their unprecedented beam properties which demand to the detector side the ability to handle high charge levels (up to $10^7$ electron-hole pairs per pixel), a dynamic range up to 1:10000 and ultra-fast readout speed. Even higher levels of charge generation are expected in the planned detection arrays for the upcoming nuclear physics experiments which require suitable techniques and instrumentation for calibration and diagnostics in such non-standard operating conditions. To this aim we investigated two techniques, based (i) on the use of mono-energetic proton bunches, available at the DEFEL beam-line at LABEC (LAboratorio di tecniche nucleari per i BEni Culturali), Italy, for high levels of charge injection and (ii) on a table-top pulsed IR laser system, suitable for low and medium injections levels (up to $\sim 10^5$ electrons). In addition to the optimization and expansion, with the introduction of new instrumentation, of the pulsed IR laser facility, the activity has been focused on the improvement and qualification of the performance of the DEFEL proton beam line at LABEC. We upgraded the beam line performance in terms of spatial resolution of the proton beam with novel remotely controlled in-vacuum hi-resolution profiling slits and with a CMOS imager as 2D beam monitor. Up to now a beam spot down to about $60\ \mu$m $\times$ $40\ \mu$m has been achieved and potentially can be fur-

ther improved. The time jitter of the proton bunches is better than 0.5 ns opening the way to probe also the transport dynamics of the charge carriers with accurate time resolution. A great effort has been also devoted to the implementation of a novel general purpose multi-channel data acquisition (DAQ) system, 500 Msample/s 12 bit, capable of full shape digitization of the output signals coming out from multi-channel devices under test. We present the development of the DAQ system, including the dedicated C language-based acquisition control software, and the functionality tests carried out with the system developed so far. We probed the test suite through qualification campaigns on two relevant case studies: we report (i) the characterization, with monochromatic protons, of the Double Sided Silicon Strip Detectors (DSSSDs) used as first and second detection stages of the telescopes that constitute the FARCOS (Femtoscope Array for COrrelations and Spectroscopy) array and (ii) a detailed qualification, carried out at low and medium levels of charge generation with the laser test suite, of a pixel matrix with DePFET (Depleted P-Channel Field Effect Transistor) readout, that is a first prototype of the DePFET-based pixel detector developed by the DSSC consortium (DePFET Sensor with Signal Compression), a collaboration aimed at the development of a large area 2D X-Ray imaging pixel detector for the new European XFEL.

# Contents

CHAPTER 1

# Introduction

## 1.1 Toward the $4^{th}$ generation of X-ray light sources

Synchrotron light sources have revolutionized X-ray experiments in many field of science, like X-ray imaging, material characterization, medical applications, archaeological microanalysis and many others. The most advanced generation, called the $3^{rd}$, combine storage rings with the extensive use of undulator magnets to generate high brilliance X-ray radiation from a relativistic electron beam.

The brilliance of the radiation is a figure of merit for many experiments, so the main reason for the improvement of light sources is the optimization of this parameter. In the most modern synchrotron light sources high brilliance is achieved with the use of undulators and with the reduction of the horizontal and vertical emittance of the electron beam (a measure of the size and collimation of the beam, related to corresponding attributes of the irradiated photons).

However the reduction of the emittance in storage rings is limited because of the random recoil given to the electron by every photon emission. Moreover these facilities have another fundamental limitation, the minimum X-ray pulse length is about some tens of picoseconds. Shorter pulses

can only be achieved at the expense of dramatic reductions of the radiated intensity, limiting the timescales that can be explored by time-resolved experiments. Access to the atomic scale of motion requires a high intensity photon beam focused on a sample as small as a molecule and, at the same time, sub-picosecond pulse length.

In the last few years a novel radiation source has been actualized, based on the principle of the Free Electron Laser (FEL). The first FEL was built by John Madey and his collaborators at Stanford University in 1976. Many information about the FEL principle can be found in literature [1], [2]. Very briefly a free electron laser is basically a linear accelerator, where an electron beam is accelerated to relativistic energy, followed by an undulator magnet. Electrons traversing the undulator are forced in a sinusoidal path and thus to radiate photons. Thanks to a phenomenon of self-organization of the relativistic beam, known as *FEL collective instability*, the emitted radiation affects the electrons position, thus the phase, causing them to emit with high coherence. This is a positive feedback process and an initially small electromagnetic field source can be amplified by many orders of magnitude before the process saturates. This process can be activated by an external laser beam, however there is a limitation because not all the wavelength values are available for conventional laser, especially at X-ray energies. The FEL collective instability can start also from the random radiation noise produced by the electron beam at the entrance of the undulator magnet, a *Self-Amplified Spontaneous Emission* [3] (SASE) process. This process was theoretically identified many years ago, long before electron beams of sufficient density and quality were technologically feasible.

Until recently FELs have been operating at infrared or near UV wavelengths, technological advances have made possible their extension to the X-ray region exploiting the SASE process, opening the way to the X-ray FEL, the $4^{th}$ generation of light sources. These revolutionary machines can deliver extremely intense, coherent and very short-pulsed X-ray radiation, increasing approximately 10 order of magnitude the peak brightness from the $3^{rd}$ generation sources. The main properties of an X-ray free electron laser are summarized in Table 1.1, which shows a comparison with an advanced $3^{rd}$ generation synchrotron light source.

The first X-ray FEL was the Free electron LASer at Hamburg (FLASH [4]), at DESY, in Hamburg (D), in the range of the soft X-rays; while the Linac Coherent Light Source (LCLS [5]), in Stanford, California obtained the first beam at $\lambda = 0.15$ nm (8.3 keV) in April 2009 and is welcoming users since late 2009, opening the era of the hard X-ray FELs. Up to now many X-ray FEL machines around the world are operational, under

**Table 1.1:** *Comparison between $3^{rd}$ generation synchrotron and Free Electron Laser light sources. Average and peak brightness are in $(\frac{photons}{s \cdot mm^2 \cdot mrad^2 \cdot 0.1\%BW})$. Data taken from [1].*

| | $3^{rd}$ Generation | SASE-FEL | Short pulse SASE-FEL |
|---|---|---|---|
| Wavelength range (nm) | 1 - 0.1 | 1 - 0.1 | 1 - 0.1 |
| Emittance (nm·rad) | 2 | 0.03 | 0.03 |
| Pulse length (ps) | 15 - 30 | 0.06 | 0.01 |
| Average brightness | $10^{20}$ | $10^{22}$ | $10^{21}$ |
| Peak brightness | $10^{23}$ | $10^{33}$ | $10^{33}$ |
| Peak power (W) | $10^{3}$ | $10^{10}$ | $10^{10}$ |

construction or designed (Table 1.2).

**Table 1.2:** *Current X-ray FEL facilities that are either operational (O), under construction (C) or undergoing advanced technical design work (D). Data referred to 2010, taken from [2].*

| Name | Location | Status | Energy (GeV) | $\lambda_{min}$ (nm) | Max. pulses/s |
|---|---|---|---|---|---|
| LCLS | USA | O | 14 | 0.12 | 120 |
| FLASH | Germany | O | 1.2 | 4.45 | $8 \cdot 10^3$ |
| XFEL | Germany | C | 17.5 | 0.1 | $27 \cdot 10^3$ |
| XFEL/Spring-8 | Japan | C | 8 | 0.1 | 60 |
| FERMI@ELETTRA | Italy | C | 1.7 | 4 | 50 |
| SwissFEL | Switzerland | D | 6 | 0.1 | 100 |
| PAL XFEL | Korea | D | 10 | 0.1 | 60 |
| LCLS-II | USA | D | 14 | 0.6 | 120 |
| SPARX | Italy | D | 2.4 | 0.6 | 100 |
| FLASH-II | Germany | D | 1.2 | 4 | 10 |

It must be specified that, being the data in Table 1.2 of three years ago, the status of the machines is not updated. In particular the Japan FEL (Spring-8 Angstrom Compact free-electron LAser - SACLA) is operative since 2011 and open to public since 2012. Also the FERMI@ELETTRA construction is complete.

Thanks to the main features of these new generation sources, like unprecedented high brilliance, time structure ranging from continuous to pulsed regime, the energy tunability and coherence, X-ray FELs open the way to great opportunities in many field of science. As an example the European X-ray Free Electron Laser [6] (European XFEL), which will be opened to the scientific users in 2015, has foreseen six instruments which will allow to perform several experiments [7]:

- hard X-rays:

  - Material Imaging and Dynamics (MID): use the coherence of the beam to explore dynamic fluctuations in matter, accessing unprecedented length and time scales;
  - X-ray Femtosecond Experiments (FXE): explore ultra-fast phenomena in the physics and chemistry of solids, liquids and soft-matter system;
  - Single-Particle, Cluster and Biomolecular Imaging (SPB): structural studies in non-periodic systems;
  - High Energy-Density Science (HED): use the FEL pulses to bring a target to extremely high values of temperature, in order to access regions of the phase diagram not easily accessible in the laboratory;

- soft X-rays:
  - Small Quantum Systems (SQS);
  - Soft X-ray Coherent Scattering and Spectroscopy (SCS): multipurpose instrument, on which different end-stations can be mounted for a variety of techniques in the soft X-ray analysis of materials.

While these new machines promise exciting scientific possibilities, their properties also pose extreme challenges to the experimental instrumentation and in particular on the requirement that the detector must satisfy to fully exploit the capabilities of these light sources.

Despite the basic concepts of these machines are identical, the practical realization and the operational schemes are quite different. As an example LCLS is 3 kilometers long and operate at a constant repetition rate up to 120 Hz. Another example is given by SACLA, the Japan facility with beam parameters similar to LCLS and a repetition rate of 60 Hz, but much more compact with a length of 750 m. Finally the European XFEL is a 3.4 kilometers long facility (Figure 1.1 shows an aerial photo of the European XFEL site) and will have a photon bunch structure: every 100 ms 2700 photon pulses (27000 flashes per second), equally spaced in time by 220 ns, will be generated (burst mode operation).

All these differences reflects on the detector requirements, thus, different kind of detectors must be developed, tailored on the particular source and on the experiment considered.

### 1.1.1 The challenge of detectors development and characterization

The dynamics of a fluctuating system in equilibrium can be observed with coherent X-rays by analyzing the temporal correlations between photons


**Figure 1.1:** *XFEL site, Hamburg (D). Picture taken from [6].*

scattered by the material. This technique is known as X-ray Photon Correlation Spectroscopy (XPCS). The timescale involved ranges from femtoseconds to seconds. Slow processes (t > 1 $\mu$s) are accessible via XPCS at $3^{rd}$ generation synchrotron light sources while the study of fast dynamics is restricted to energy domain techniques. The advent of X-ray FEL radiation offers the great advantages of high spatial coherence, extremely high brilliance and and sub-picosecond time resolution. For the first time it will be possible the study of fast dynamics in the time domain.

However the efficient application of the XPCS technique depends crucially upon the availability of 2-D detectors requiring high spatial resolution, high framing rates, high quantum efficiency and low noise. Table 1.3 summarizes a base-set of requirements for 2-D detectors suitable for XPCS experiments with a X-ray free electron laser light source.

More generally speaking, the relevant parameters can be summarized in two different kind of requirements:

- FEL dependent requirements:
  - Energy Range;
  - Frame rate/repetition rate;
  - Signal rate/pixel/bunch;

**Table 1.3:** *Key parameters for XPCS 2-D detector. Data taken from [8].*

| Parameter | Base requirement | Option |
|---|---|---|
| Single photon resolution | Yes | - |
| Photon energy range (keV) | 8-12 | 3-15 |
| Quantum efficiency | > 0.8 | 1 |
| Radiation hardness | yes | - |
| Number of Pixels | 1k × 1k | 5k × 5k |
| Preprocessing | no | yes |
| Pixel Size ($\mu$m) | 50-80 | $\leq$ 50 |
| Signal rate/pixel/bunch | few up to 100 | up to 1000 |
| Timing | 10 Hz (bunch train) | 30 Hz (bunch train) |

  - Radiation Tolerance.

- application specific requirements:

  - Single Photon Resolution;
  - Number of Pixels;
  - Pixel Size;

A relevant set of required performance parameters for applications at the new X-ray laser sources are summarized in Table 1.4. From the reported

**Table 1.4:** *Experimental requirements for the 2-D detectors. Data taken from [9].*

| Parameter | 2-D imager requirements for FLASH, LCLS, SCSS and XFEL |
|---|---|
| Single photon resolution | Yes |
| Energy range | 0.05 to 24 keV |
| Signal rate/pixel/bunch | $10^3$ ($10^5$) |
| Quantum efficiency | > 0.8 |
| Number of Pixels | > 512 × 512 |
| Pixel Size | < 100 × 100 $\mu m^2$ |
| Frame rate/repetition rate | 5 Hz to 120 Hz (except XFELs 4.5 MHz operation) |
| Readout noise | < 150 electrons |

data is evident the very demanding requirement of a high dynamic range ($10^4$ X-ray photons per pixel expected), even more critical as coupled with a high resolution down to single photon. In the following will be discussed the practicality of the parameters in Table 1.4 and the consequence they have in the development and characterization of suitable radiation detectors. High dynamic range is discussed in 1.3.2, in the wider context of the issues related to the high charge injection levels.

#### 1.1.1.1 Time structure of the light signal

It must be noticed that each X-ray pulse is a new experiment and the detector system must be able to read, digitize and record the data before the next incoming pulse.

At LCLS or Spring8, with continuous wave operation, there are evenly spaced pulses and this is not a critical operating condition. Critical conditions arise when the repetition frequency is much higher, this is the case for the pulsed burst operation mode foreseen at the European XFEL source, which is showed in Figure 1.2.

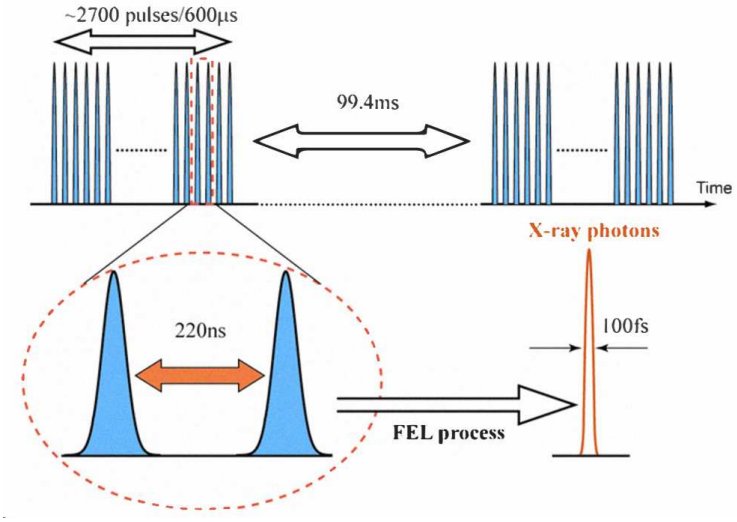


**Figure 1.2:** *European XFEL burst operation mode. [10]*

The frequency of operation is 10 Hz, but every period is composed of a train of ∼2700 X-ray pulses (pulse length ∼100 fs) equally spaced with a challenging time separation of 220 ns (4.5 MHz burst frame rate), followed by a 99.4 ms of long silent gap, exploitable for off-chip data transfer. The development of a detector capable to accomplish the operations of read-digitize-store the data in this very short time requires fast charge collection times and therefore a careful qualification of transport dynamics with nanosecond time resolution, as a function of the injection position within the single pixel and of the injected charge.

#### 1.1.1.2 Energy range and quantum efficiency

The wide energy range of 3 orders of magnitude (10 eV - 10 keV) cannot be covered by a single detector technology. Taking the silicon as the reference

material, Figure 1.3 reports the attenuation length of photons in the energy range of interest. With regard to the soft X-rays ($E < 1$ keV, highlighted

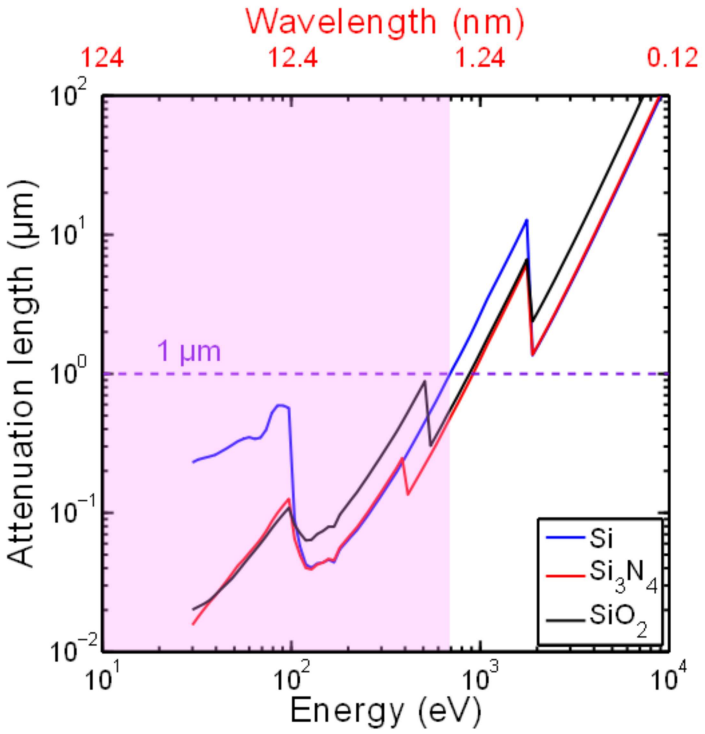


**Figure 1.3:** *Attenuation length of photons in $Si$, $Si_3N_4$, $SiO_2$ as a function of the energy (bottom axis) and of the wavelength (top axis). Data taken from [11] X-ray database.*

with the pink area) we can observe an attenuation length less than 1 $\mu$m. In this case the performance, in terms of quantum efficiency (QE), is limited by the entrance window (e.g. a 50 nm thickness of $SiO_2$ means a loss of 25% of 250 eV photons). At this low energy also the electronic noise is a critical issue, as discussed in 1.3.2.

In the hard X-ray range (3 - 15 keV) the QE in 450 1$\mu$m-thick silicon is high for energies up to 10 keV, but the high generated charge has a negative impact on the detector performances (discussed in 1.3.1).

### 1.1.2 Detectors needed for the foreseen experiments

There is a wide spectra of foreseen experiments at the free electron laser facilities and in general every experiment may require a specific detection system. The discussion is here focused on area detectors for imaging experiments.

Two representative technologies, suitable for the development of devices compatible with the free electron lasers requirements, are briefly presented. It must be noticed that none of these technologies, at present, is capable to satisfy all the requests summarized in Table 1.4:

- fully depleted pn Charge Coupled Devices (pnCCDs [12]): similar to the metal-oxide-silicon based MOS CCDs, the pnCCDs are based on high resistivity n-type silicon (typ. 5000 $\Omega$cm) and a manufacturing process that makes use of both wafer surfaces for the sensor and electronics circuitry. This enables the full depletion of the entire silicon volume and, thus, makes use of the full depth as sensitive volume. A n-channel JFET can be integrated on the pnCCD chip and connected to the anode. The pnCCDs features very low noise, high quantum efficiency in the energy range 100 eV - 10 keV and a capacity of $\sim 10^6$ electrons, but full frame rates limited to the order of $\sim$100 Hz. A detector developed for X-ray FEL facilities based on the pnCCD is the CAMP chamber [9];

- hybrid pixel detectors: in these devices the detector and the front-end electronics are optimized separately and then connected with bump-bonding. The advantage is a greater active area on the detector chip surface (not used for readout) and, at the same time, the possibility to develop a complex front-end electronics, both analog and digital, very close to the detector. Cons are the pixel size and capacitance limited by the minimum size of the bump-bond and the electronic noise, which is higher if the on-chip transistor is not available. An example of hybrid pixel detector, currently under development for the European XFEL source, is discussed in 1.1.3.

### 1.1.3 New detector developments at the European XFEL: the DSSC project

As enlightened, the detector performance requirements of the X-ray FEL facilities are extremely demanding and difficult to realize. To make optimal use of the unprecedented capabilities of the European XFEL, the European XFEL GmbH started a detector R&D program in 2006. The technology concepts of the detectors system presently under development are complementary in their performance and will cover the performance requirements of a large fraction of scientific envisaged applications.

In particular three consortia have been selected to develop pixel detector systems:

- Adaptive Gain Integrating Pixel Detector [13], [14] - AGIPD consortium;
- Large Pixel Detector [15] - LPD consortium;
- DePFET (Depleted P-Channel Field Effect Transistor) Sensor with Signal Compression - DSSC consortium.

The attention will be focused on DSSC in the following, a consortium consisting of the MPI Semiconductor Lab in Munich (coordinator), DESY-Hamburg, Politecnico di Milano, Heidelberg University, Bergamo University and Siegen University.

The DSSC system is based on hybrid pixel detectors with DePFET readout. In a standard DePFET [16] the electrons generated by absorbed photons flow toward a buried n-implantation, named *internal gate*, underneath the gate of a FET transistor, hence the stored charge has a steering effect on the transistor current. The DePFET is therefore a natural building block for a pixel detector as it combines the properties of detector, amplifier and storage cell in a simple structure. After the measurement of the transistor current, the charge stored in the internal gate has to be removed by means of pixel-level dedicated contact. A characterization of a first prototype of a DSSC DePFET matrix will be presented in Chapter 4.2.

The first advantage of the integrated detector/amplifier DePFET structure is the low noise performance, making it suitable for low energy X-ray experiments.

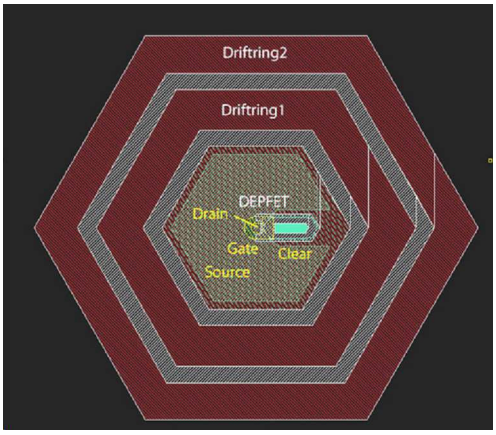


**Figure 1.4:** *The DSSC pixel cell with in-pixel drift rings. Image taken from [17]*

In addition in the the DSSC design pixel [17] a small drift chamber surround the DePFET, that is located in the middle of the pixel structure

(Figure 1.4). This feature allows fast and complete collection of the charge at the buried gate. The challenge of providing excellent charge resolution (single photon detection) with the very high dynamic range capability is accomplished providing a strongly non-linear current-charge characteristic, by mean of an internal gate implantation structure suitable for the intrinsic signal compression .

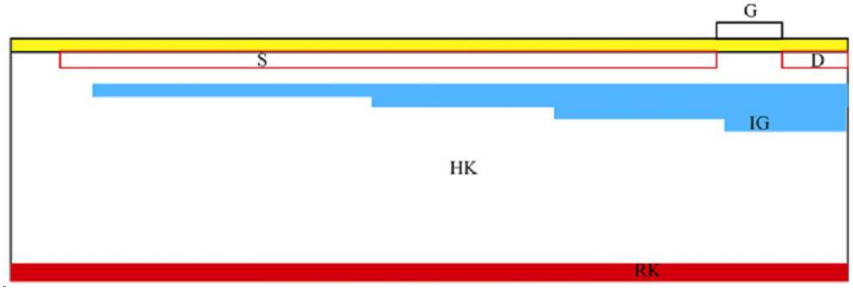


**Figure 1.5:** *Detail of the DSSC DePFET design of the internal gate (light blue area) for analog signal compression. Image taken from [17]*

The mechanism act as follows: contrary to a standard DePFET the internal gate extends beyond the gate region (Figure 1.5) below the source, at low level of charge injection the small signal charges are stored right below the transistor channel, being fully effective in steering the transistor current; on the other hand at higher level of charge generation the electrons will be distributed between transistor channel and source region, having a reduced effect on the transistor current.

The focal plane, currently under development, is showed in Figure 1.6. It consists of a large 1 Mega-pixel X-ray imager with a size of approximately 210 $\times$ 210 mm$^2$ [10], subdivided in 128 $\times$ 256 pixel blocks, each block bump bonded to 8 readout ASICs. The signals coming from the sensor are processed by the ASIC and locally stored in an SRAM, which is able to record at least 640 frames/macro-bunch. The data are transferred off during the dead time of 99.4 ms (refer to Figure 1.2 for the European XFEL bunch structure). The key properties of the system are summarized in Table 1.5

The discussion about the DSSC project enlightens how demanding is the implementation of Free Electron Laser source suitable devices, as should be evident from the particular features implemented in a standard DePFET pixel to cope with the European XFEL performance requirements. On the other hand also the characterization of the device is a severe issue and needs advanced techniques of precise qualification and calibration in a wide range

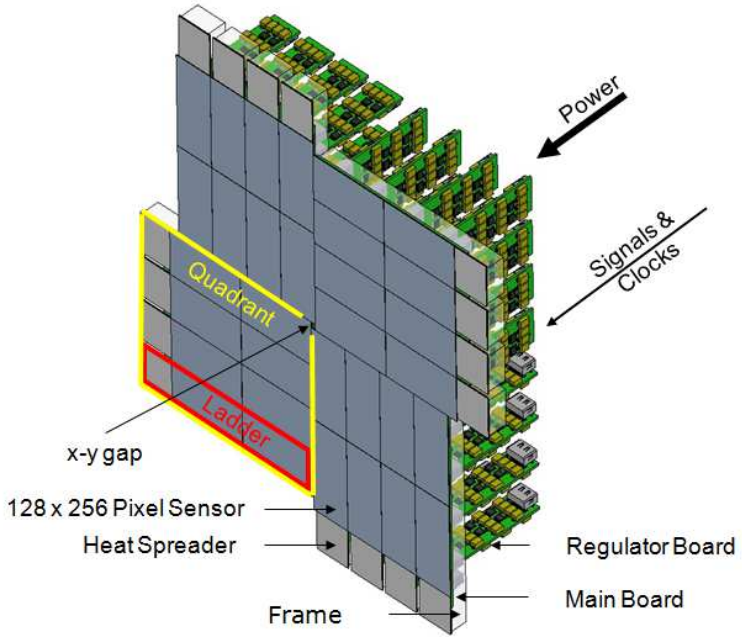


**Figure 1.6:** *Sketch of the DSSC final system. Image taken from [18]*

**Table 1.5:** *DSSC system main parameters. Data taken from [10]*

| | |
|---|---|
| Energy | 0.5 keV $\leq$ 20 keV<br>(optimized for 0.5 keV $\leq$ 6 keV |
| Number of pixels | 1024 $\times$ 1024 |
| Sensor pixel shape | Hexagonal |
| Sensor pixel pitch | $\sim$204 $\times$ 236 $\mu$m$^2$ |
| Dynamic range (photons/pulse/pixel) | > 10000 photons |
| Resolution | Single photon detection also @ 0.5 keV |
| Frame rate | 0.9 - 4.5 MHz |
| Stored frames per macro-bunch | $\geq$ 640 |
| Mean power consumption | $\sim$ 400 W in vacuum |
| Operating temperature | -20 Â°C optimum<br>room T possible |

of charge generation levels. The intrinsic signal compression feature, implemented to achieve high dynamic range and single photon resolution, makes the amplitude response of the pixel strongly non-linear, requiring a careful calibration in a wide range of charge generation levels with great accuracy for not degrading the single photon resolution. Not to mention also the high frequency of the XFEL burst mode operation, i.e. only 220 ns are available for the readout of the pixel, as previously discussed in 1.1.1.1.

Within this short time the charge is collected at the internal gate and, after the readout, must be removed with dedicated contacts (reset operation), hence both the collection and the reset operations require a careful characterization of charge transport dynamics.

## 1.2 Detectors for particles identification in Nuclear Physics experiments

Radioactive isotopes, since the discovery of radioactivity, have been essential for fundamental Nuclear Physics (NP) research. Developments over the last decades for the production and study of radioactive ion beams (RIBs) all over the world [19], [20], [21], [22], allow to study nuclei and their many energy states, not easily found in nature, far from the valley of stability. In nuclear physics multi-fragmentation experiments the radioactive ion beam is accelerated and used to bombard a target, interacting with the nuclei of the atoms that make up the target itself. Heavy-ion collisions at intermediate energies produce a large variety of particles and fragments in a single experiment, reaction products span from light charged particles (LCP) to intermediate mass fragments (IMF, $3 \leq Z \leq 20$). The identification of all the reaction products (in charge Z and in mass A) on an event-by-event basis and the measurement of their reciprocal correlations allows quantitative understanding of the reaction dynamics and probing space-time properties of emitting sources.

Even at the most advanced rare isotope facilities the beam intensity is low, in addition two, or more, particle correlation measurements require large statistics, obtained widening the solid angular coverage. The identification must be carried out with high energy resolution ($\leq 1\%$) for isotopic identification of intermediate mass fragments and high angular resolution ($\leq 1^{\circ}$) in order to investigate multi-particle correlations. The detection systems are large detector arrays covering a wide solid angle in order to increase the detector geometrical efficiency. The array consist of individual telescopes, stacks of silicon detectors (thickness from tens of $\mu$m to $\sim$1 mm) and scintillators (thickness of few cm). A silicon photo-detector is usually used to convert the scintillation light to an electric signal. The use of semiconductor detectors is mandatory with the discussed requirements of energy and angular resolution. In the most recent detector systems the silicon detector stage is based on silicon strip technology and the telescopes evolve toward multi-segmented detectors with increasingly granularity, in order to enhance the system angular resolution.

A significant example is HiRA [23] (High Resolution Array), a collab-

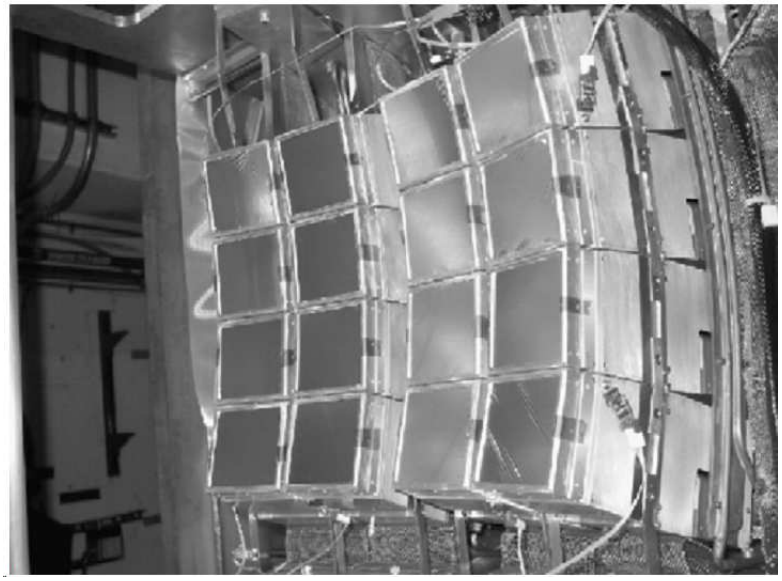

**Figure 1.7:** *Photograph of 16 Hira telescopes. Image taken from [23].*

orative effort between Indiana University, Michigan State University and Washington University, funded by the National Science Foundation's Major Research Instrumentation in 1999. HiRA is a modular array that consist of 20 identical telescopes (Figure 1.7), each telescope is a stack of a 65 $\mu$m-thick single sided silicon strip detector with 32 strips, a 1.5 mm-thick double sided silicon strip detector (DSSSD) with 32 $\times$ 32 strips and four trapezoidal CsI(Tl) crystals (3.5 cm $\times$ 3.5 cm on the front and 3.9 cm $\times$ 3.9 cm in the rear with a thickness of 4 cm) forming a 2 $\times$ 2 matrix. The active area of the silicon detectors is 6.25 $\times$ 6.25 cm$^2$ with a strip pitch of 1.95 mm and an inter-strip gap of 25 $\mu$m on the front and 45 $\mu$m on the back. Hira shares many features with its predecessor LASSA [24] (Large Area Silicon Strip Array). Each of the nine individual telescopes of LASSA was composed of a Si-Si-CsI(Tl) stack, the silicon detector stages was comprised of a 65 $\mu$m-thick Si strip detector backed by a 500 $\mu$m-thick DSSSD, both with 16 strips and an active area of 5 $\times$ 5 cm$^2$ (pitch 3 mm with an inter-strip isolation of 100 $\mu$m), performing an angular resolution $\Delta\theta$ $\sim$0.9°.

Another silicon strip detector based array is MUST [26] (MUr à STrips), developed by a collaboration between the IPN-Orsay, DAPNIA-SPhN Saclay and DPTA-SPN Bruyères le Châtel, a modular array consisting, in the first version, of 8 silicon strip-Si(Li)-CsI telescopes. The first stage is a 300 $\mu$m-thick double sided silicon strip detector, with 60 vertical and 60

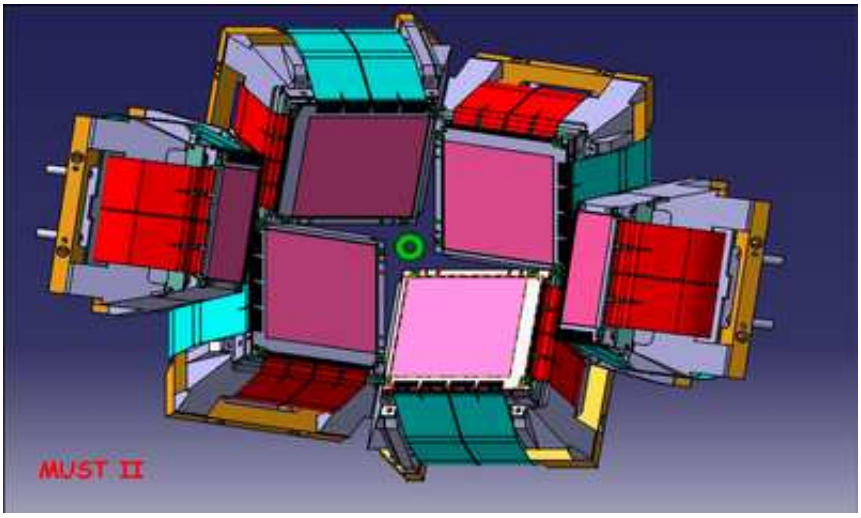


**Figure 1.8:** *The MUST2 array. Image taken from [25].*

horizontal strips and an active area of $60 \times 60$ mm$^2$ (90 $\mu$m inter-strip gap), giving an X-Y position resolution of 1 mm. Each strip detector is backed by a $58 \times 58$ mm$^2$ lithium drifted silicon diode (Si(Li)) of 3 mm thickness and a 15 mm CsI crystal. The evolution of MUST is MUST2 [27], [28], it consists of 6 telescopes (see Figure 1.8) that multiply the solid angle coverage of the MUST ensemble by a factor of three. Compared to its predecessor, the innovation comes from the electronics based on ASIC chips and the new Si strip detectors featuring an active area of $10 \times 10$ cm$^2$ with a number of strips equal to $128 \times 128$ and an inter-strip gap of 56 $\mu$m.

Side by side to the detection of the reaction products, the identification techniques play obviously a fundamental role. Classical particles identification techniques include:

- $\Delta$E-E analysis, that exploits the mutual dependence of the energy released by the impinging particle in consecutive stages of the telescope. Considering a two stage telescope and a particle that stops in the second stage, $\Delta$E is the energy released in the first stage and E is the remaining energy released in the second stage. In silicon detectors the amplitude of the output signal is proportional to the energy released by the ionizing particle, regardless of the type of particle. The energy released depends on the silicon detector thickness and on the Bragg curve of the particular fragment. In case of scintillators the signal amplitude is a function of the charge and mass of the particle and is no more linear to the energy released. In principle $\Delta$E-E scatter plots

allow for both charge (Z) and mass (A) identification, however, depending to some degree on the resolution of the telescope, this is true for light particles while, for heavy fragments, generally the mass resolution is low and only Z identification is feasible. Obviously, for very low energetic particles that stop in the first stage, the identification by means of this technique is not possible;

- time of flight (ToF) is the measurement of the velocity of the fragments produced, that is related to the mass of the particle through the kinetic energy. ToF consists basically in a time difference measurement between two timing signals, the start signal comes usually from the radioactive ion beam accelerator, the stop signal is provided by the detector. The velocity is calculated as the ratio between the known target-detector distance and the time of flight. In case of low energetic particles stopping in the first stage this technique allows for mass identification (no charge identification is possible), if particles punch through the first detection stage, ToF can be combined with other identification plots in order to provide charge identification;

- pulse shape analysis exploits the dependence of the detector signals on the charge, mass and energy of the impinging particles to identify the reaction products. Processing techniques based on the pulse shape analysis are powerful tools for the identification of particles stopping in the first stage. The Z-discrimination can be obtained by means of the measurement of the rise time of the signals collected from the silicon detector. When this technique is combined with a ToF measurement, complete identification in charge and mass of the projectiles stopped in the first stage is possible. The resolution in mass and charge separation are strictly related to the physical properties and to the topology of the detector as well as to the front-end electronics performance. Moreover the requirements for the ToF and pulse shape analysis are partly conflicting, Tof requires fast timing signals while pulse shape benefits from slower detector pulses [29].

A combination of $\Delta$E-E and pulse shape analysis techniques has been applied [30] to the discrimination of the reaction products with CHIMERA [31] [32] (Charged Heavy Ion Mass and Energy Resolving Array), a large $4\pi$ ($\sim$95% of the solid angle) multidetector array made of 1192 telescopes. Each telescope of CHIMERA is composed of two detection stages, the first is a large area ($5 \times 5$ cm$^2$) planar thin (300 $\mu$m) silicon detector, backed by a CsI(Tl) scintillator. An example of particle identification, with a 21 MeV/u $^{20}$Ne beam bombarding a $^{12}$C target, is showed in Figure 1.9. The scatter

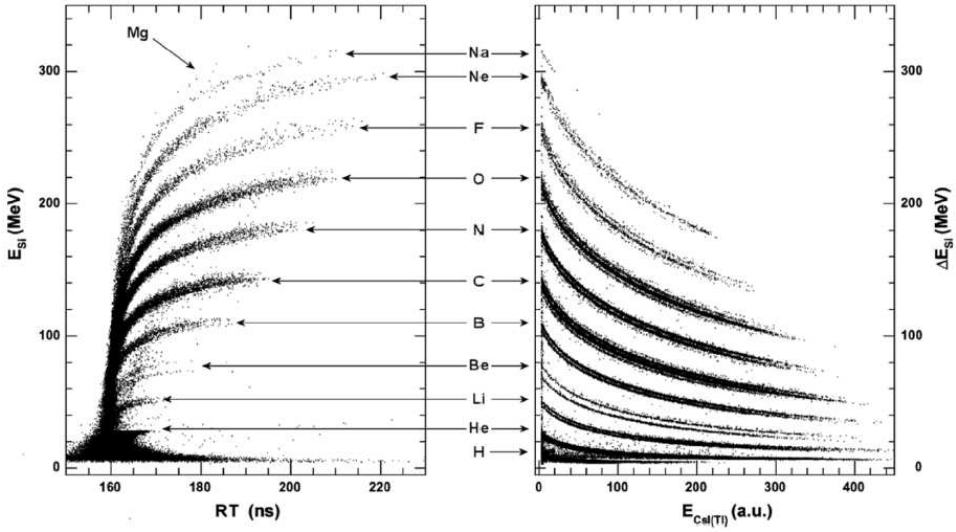


**Figure 1.9:** *Particle identification of the reaction products obtained with a 21 MeV/u $^{20}Ne$ beam bombarding a $^{12}C$ target, by means of $\Delta$E-E and pulse shape analysis techniques. The $\Delta E_{SI}$-$E_{CsI(Tl)}$ scatter plot on the right displays the reaction products producing a signal in the scintillator. The $E_{SI}$-rise time scatter plot on the left displays the reaction products stopping in the silicon detector (300 $\mu$m thickness). Charge identification up to Z=11 is obtained in both cases. Image taken from [30].*

plot on the right is a $\Delta$E-E plot, $\Delta E_{SI}$ is the energy released in the first stage and $E_{Cs(Tl)}$ is the remaining energy released in the scintillator where the particle is stopped. In this plot are displayed all the reaction products producing a signal in the scintillator. As clearly visible, charge identification up to Z=11 is achieved. Also isotopic identification is reached for all the identified charges [30]. For low energetic particles stopping in the silicon detector first stage the inapplicability of the $\Delta$E-E technique has been aforementioned, so the pulse shape analysis technique has been exploited in order to identify even the least energetic fragments. The result is showed in the scatter plot on the left, $E_{SI}$ is the energy of the particle stopped by the first silicon stage and RS is the rise time of the silicon detector output signal (preamplified and digitized). The particle identification capability obtained with this technique is fully evident from the scatter plot. Again charge identification up to Z=11 is obtained, in other words pulse shape analysis allowed the identification, even at low energies, of the large variety of particles identified at high energies with the $\Delta$E-E technique. Furthermore isotopic identification is reached for the identified particles up to Z=5 [30].

Multi-fragmentation experiments evolve toward the production of an in-

creasingly large variety of particles and fragments, the complex scenario, consequence of the complex structure of LCP and IMF, calls for the development of detection systems with higher angular and energy resolution and wide dynamic range, able to identify the broadest ensemble of reaction products, from the heaviest to the lightest ones, in a wide energy range. The identification of the most energetic and penetrating light charged particles require a high stopping power of the telescope, on the other hand a low identification threshold is required for both low energetic LCPs and IMFs. These requirements drives towards detector stages based on silicon strip technology and the telescopes evolve towards higher segmentation degree topologies, like the HiRA and MUST2 arrays beforehand discussed, enhancing the angular resolution. Moreover the higher segmentation means lower detector capacitance, that allows increasing the signal-noise ratio and obtaining high energy resolution [29]. The identification power can be greatly enhanced by means of pulse shape analysis techniques, that allow to identify the least energetic reaction products stopping in the first detection stage. However the pulse shape analysis capability could be compromised by the combination of a high granularity detector with the high levels of charge injection achieved in such experiments, as discussed in 1.3.

## 1.3 The issue of detector characterization at high charge injection levels

The two different fields of science discussed so far, experiments with high intensity X-ray photon beams at the $4^{th}$ generation synchrotron light sources and particle identification in multi-fragmentation nuclear physics experiments, have a common, very demanding, requirement consisting in an exceptionally high dynamic range with an excellent energy resolution. Coping with these requirement is very hard, a meaningful example is provided by one of the implementation for the European XFEL, that has been depicted in 1.1.3, while pulse shape analysis has been described as a powerful technique for the identification of low-energy particles stopping in the first detection stage of a telescope, enhancing the identification power, as discussed in 1.2. Moreover the light intensity or the particle energy are so high that a huge amount of charge carrier is generated, influencing the spatial and time response of the detector as well as the shape of the output signal, as exposed in the following.

### 1.3.1 High charge intensity effects

With the expected high intensity of photon per pixel ($10^4$ ph/pixel/bunch) at the new $4^{th}$ generation synchrotron light sources, the detectors must cope with very high levels of charge injection. For example, referring to Table 1.4, an irradiation with $10^4$ hard X-ray photons (10 keV) means a great amount of generated electron-hole pairs in silicon, approximately equal to $10^4 \text{ph} \cdot 10^4 \text{eV}/3.6 \simeq 3 \cdot 10^7$ e-h pairs. Similar, if not higher, level of charge injection are reached in intermediate energy particle physics experiments. Even in case of light charged particles interaction $10^7$ e-h pairs can be generated in a 1 mm thick first stage silicon detector (Figure 1.13), while interaction with intermediate mass fragments releases energies up to hundreds of MeV in silicon (Figure 1.9). At this high level of generated charge Coulomb repulsion have a strong effect in the transport dynamics of the detector. Moreover at the highest energies the charge density can be so much high that plasma effects become relevant , having a great impact on the detector collection time and signal shape.

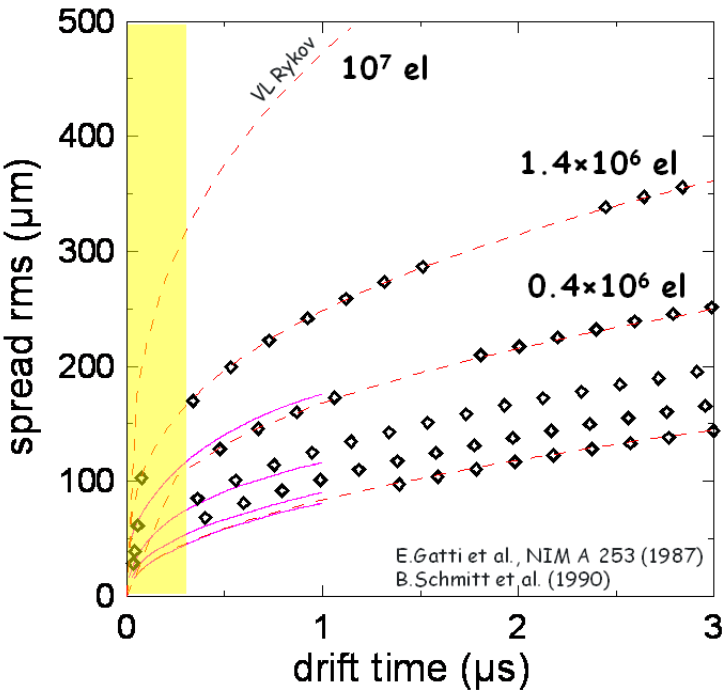


**Figure 1.10:** *Charge broadening effect for different levels of charge injection. The spread of the charge cloud is showed as a function of the drift time. The yellow area corresponds to the typical charge collection times for silicon detectors [33].*

In Figure 1.10 the Coulomb repulsion is showed, in terms of the broadening effect of the charge cloud as a function of the drift time. The yellow area highlights the typical charge collection times for silicon detectors. The broadening effect is more evident at higher levels of charge generation. The Coulomb repulsion dominate over the diffusion process, especially at shorter timescale ($\sim$100 ns). This means a remarkable charge broadening, even with short charge collection times, that cause a degradation of both the spatial and time resolution of the detector.

Plasma effect is, briefly, the shielding of the inner region of the charge cloud from the depletion field created by the external bias, because a high charge carrier density. As a consequence the charge moves slowly toward the anode and the collection time increases by a so-called plasma erosion time. Figure 1.11 shows the consequence of plasma formation in terms of the plasma erosion time as a function of the electric field in the detector for different charge density levels. Obviously at higher electric field the plasma effect become less noticeable, moreover it can be observed that, given the charge density, the erosion time dramatically decrease when the electric field reach a particular value. In other terms the depletion field becomes dominant respect to the electric field inside the high-density charge cloud.

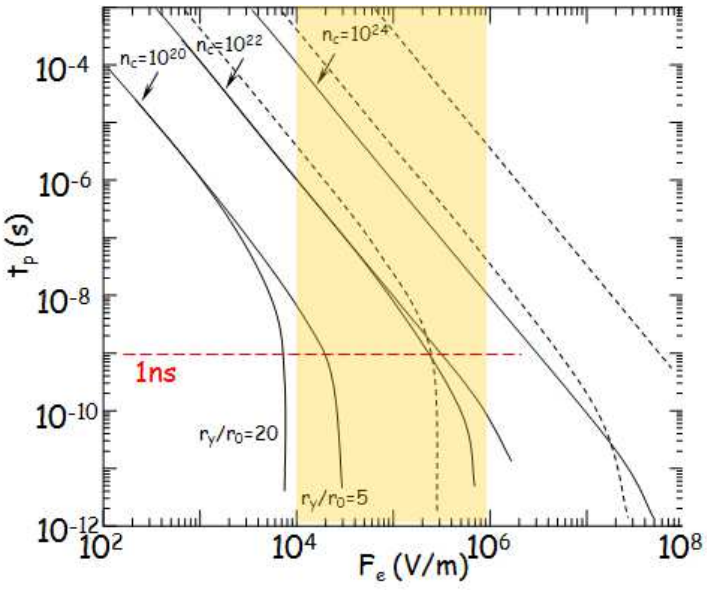


**Figure 1.11:** *Plasma effect for different levels of charge density. The plasma erosion time is represented as a function of the electric field in the detector. The highlighted area corresponds to the typical electric field for silicon detectors [34].*

Within the Figure 1.11 are highlighted in the yellow area the typical depletion field values reached inside the detectors and 1 ns as the plasma erosion time limit (below this value plasma effects may be assumed negligible considering the typical charge collection time). At high charge density levels the erosion time increases, this produce a great effect on the collection time, having a negative impact on the detector speed and affecting the signal shape.

Finally it must be remarked that these are 3-D effects, complex simulation can model these phenomena [35], but need also confirmation by direct experimental qualification. Devices in general require at least two-dimensional - in some cases even three-dimensional - transient analysis to arrive at quantitatively correct results. At present three-dimensional analysis is only done in very exceptional circumstances due to the large demand on computer memory and power. In general, one relies on two-dimensional simulations and tries to guess the changes expected for three dimensions from several two-dimensional simulations [36]. So it is necessary a direct qualification of the detector response, that depends on the position of interaction, ionization profile, charge injection level and so on, even at the highest ionization densities.

### 1.3.2 High dynamic range and high energy resolution

When the detector must cope with the requirement of a high dynamic range and, at the same time, an excellent energy resolution is needed, the realization is very demanding and rely both on the properties of the detector and on the performance of the readout electronics.

Firstly the case of the free electron laser source is discussed. The request of a very high dynamic range (up to $10^4$ photons) in combination with a very high resolution, down to the single photon, is a very critical issue, especially at low energy. In fact there is the need to count up to $10^4$ in the most irradiated area and at the same time to discriminate the single count in the adjacent pixel with a low error probability.

With the very short length of the X-ray pulse (100 fs) photon counting is impossible, so integrating detectors are needed, but the discrimination of single photons requires a very low electronic noise, especially in the soft X-rays range. Moreover, in order to achieve at the same time the high dynamic range and the single photon precision, a great accuracy in the calibration of the amplitude response is needed.

Figure 1.12 shows the calculated curves of the energy standard deviation ($\sigma_E$) as a function of the incoming X-ray photon energy. The curves are cal-

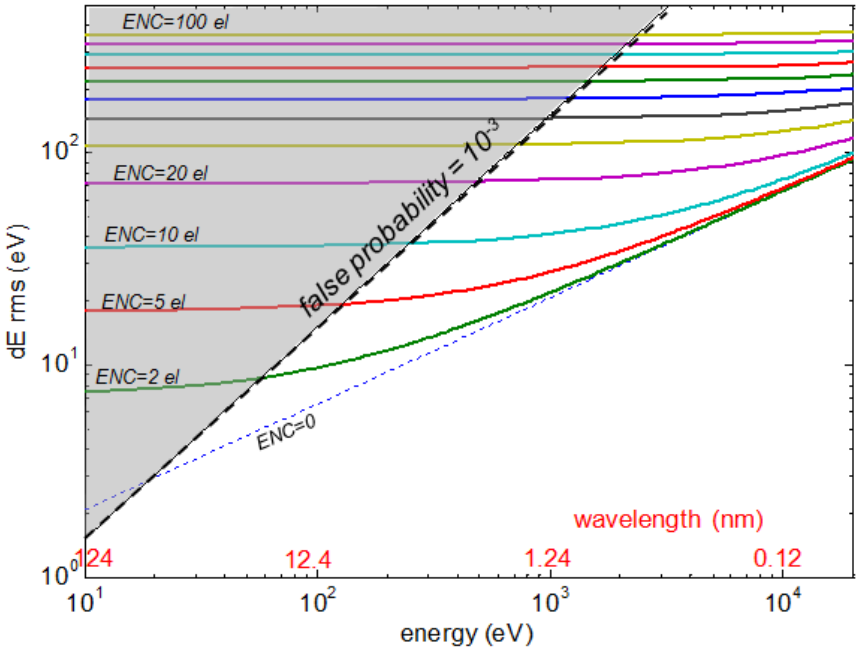


**Figure 1.12:** *Energy standard deviation as a function of the incoming X-ray photon energy, showed for different electronic noise contribution.*

culated adding two noise contributions, the one related to the Fano factor, energy dependent ($\sigma_{Fano} = \epsilon_{Si} \cdot \sqrt{E_{ph}/\epsilon_{Si} \cdot F_{Si}}$, with $\epsilon_{Si} = 3.6$ eV and $F_{Si} = 0.12$), and the constant one related to the electronic noise ($\sigma_{ENC} = \epsilon_{Si} \cdot ENC$). Each curve is calculated at a different ENC contribution, with the formula $\sigma_E = \sqrt{\sigma^2_{Fano} + \sigma^2_{ENC}}$.

The electronic noise contribution imposes a lower limit to the minimum energy of the single detectable photon with low false-positives, so it is clear from Figure 1.12 that the discrimination at lower energy require high performing low noise electronic. Furthermore low noise electronic means long filtering times, this is in contrast with the requirement of a high readout speed.

In case of detection system for particle identification the discussion is quite similar. The identification in a wide energy range of light charged particles and more massive fragments require a low identification threshold. Such threshold depends from both the detector and the front end electronics, however, cause the particle range, a value of the order of few hundreds of keV is a standard for the most penetrating light charged particles

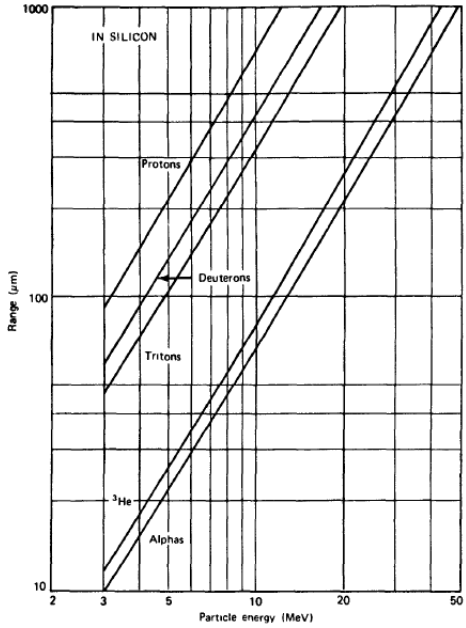


**Figure 1.13:** *Particle range as a function of energy for different light charged particles in silicon. Image taken from [37].*

(Figure 1.13) while for heavy fragments this value increase cause the less penetrating power. The most energetic fragments can release in silicon energies up to several hundreds of MeV, as visible from Figure 1.9 (silicon thickness 300 $\mu$m), leading to a high dynamic range of three order of magnitude. At the same time the requested energy resolution is $\leq 1\%$, so the readout electronics plays a key role. The increasingly granularity of the silicon detectors can copes with the request of high angular resolution and, thanks to the lower capacitance that allow increasing the signal-noise ratio, with the request of high energy resolution.

Pulse shape analysis has been introduced as a powerful tool able to identify even low-energy particles stopping in the first silicon stage, however the increasing granularity combined with the high charge injection level in the silicon strip detector stage require an accurate qualification of the detector response in terms of amplitude, time and also of the full shape in order to qualify the charge sharing phenomena effects on the pulse shape analysis capability of the whole system. Last but not least an accurate calibration of the detection system is required in the foreseen charge generation range with an absolute reference.

## 1.4 Detector qualification over a wide dynamic range

Summarizing, the new $4^{th}$ generation X-ray sources will open up areas of research that were inaccessible so far, but pose also a great challenge in the development and the accurate characterization of suitable radiation detectors. On the other hand a different field of science, Nuclear Physics experiments, has been discussed. In both cases the ionization levels reached in semiconductor detectors are very high and a wide dynamic range with high energy resolution is required. In particular the following issues have been discussed:

- time structure of the light signal, in the most demanding case, like the European XFEL, the detector must perform a very high readout speed, thus a qualification of the transport dynamics with nanosecond precision is required;
- energy range and quantum efficiency, in this case the entrance window must be carefully designed and at very low energy the electronic noise is a critical issue, therefore the development and characterization of a high performing front-end electronics is needed;
- high charge intensity effects, critical in terms of position and time resolution of the detector and of the output signal shape, 3-D effects hard to model and simulate that require a direct characterization of the detector;
- high dynamic range and high energy resolution are very demanding and conflicting requirements, the amplitude response must be carefully calibrated, also the electronic noise is an issue for the achievement of high energy resolution and the front-end electronics must be qualified as well.

It is necessary therefore to develop characterization techniques in a wide range of charge injection level, suitable for the detector diagnostics and calibration and for the qualification of the front-end electronics in the expected operative energy range as well as for the validation of the simulations with experimental data.

In Figure 1.14 the basic concept of a characterization suite is presented. The main actors are:

- radiation sources able to inject a precise quantity of electric charge in a well defined position (X, Y lateral coordinates) of the detector with high time accuracy as well as with tunable ionization profile (tunable

Z, penetration depth in the detector); this allow to perform a characterization as a function of energy, position and time;

- a fast data acquisition system (DAQ) able to digitize the front-end electronics output for off-line analysis;
- a dedicated deconvolution algorithm [38] able to recovery the induced anode current pulse shape, which is directly correlated to the charge cloud (Ramo's theorem [39]) and is a powerful tool to gain deeper insight on detector behavior and for detector diagnostics.

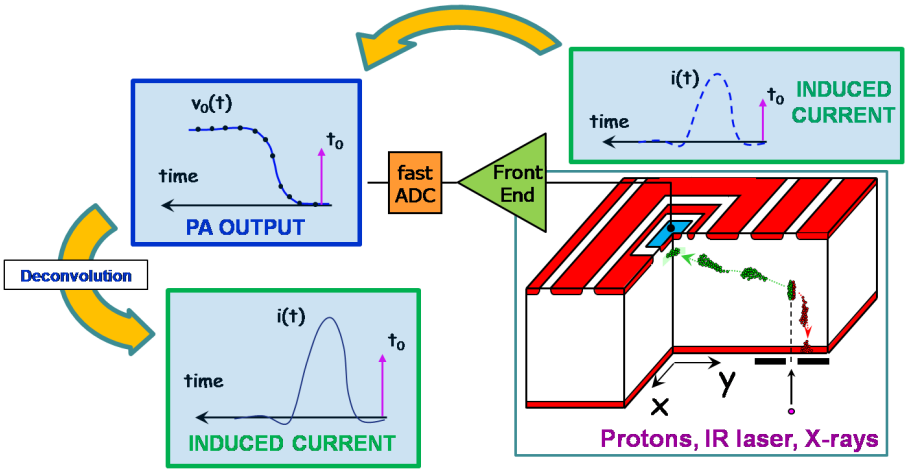


**Figure 1.14:** *Basic concept of a characterization suite.*

The development of these experimental techniques and their application to qualify relevant detector systems has been assessed in the framework of the ASPIDE experiment supported by INFN (*Istituto Nazionale di Fisica Nucleare*), a collaboration between the INFN sections of Milano and Firenze. ASPIDE means **A**pplication of **S**ingle **P**roton bunches **I**nteractions to **D**etector & **E**lectronics response characterization at high charge levels; the main goal of the experiment is the upgrade of the DEFEL beam line at LABEC (LAboratorio di tecniche nucleari per i BEni Culturali), Sesto Fiorentino, Firenze, Italy, especially tailored for detector characterization, at high charge levels, for different application fields (X-ray FELs, Nuclear physics experiments etc.). The proton facility has been complemented by a pulsed laser system in order to cover lower charge levels

Aim of this work is to present the development of a radiation detector characterization technique in a wide range of charge injection as well as to show some relevant case studies. The discussion is organized as follows:

- Chapter 2: in this chapter the high - spatial and timing - resolution facility, based on a pulsed laser system for the lower charge levels and on mono-energetic proton bunches for the higher levels of charge injection, is introduced. The improvements carried out during the present work as well as the performance assessment of the two radiation sources are described in detail.
- Chapter 3: this chapter is dedicated to the development of a general purpose multichannel data acquisition system capable of full shape digitization of the waveforms collected at the output of the detectors under test. The implementation of the system is described, in terms of the exploited hardware and of the developed management software. Finally the first functionality tests of the implemented system are discussed;
- Chapter 4: in this chapter the application of the developed characterization suite to the following relevant case studies is presented:
  - the Double Sided Silicon Strip Detectors (DSSSDs) used as first and second detection stages of the FARCOS array telescopes. The energy calibration of DSSSDs in a wide range of injected charge, performed with mono-energetic protons, is presented. The sharing phenomena, that occur in case of inter-strip irradiation, must be investigated in order to evaluate their effect on the pulse shape analysis capability of the system. Scans of the strips performed at high charge injection levels, with the collection of the pulse shape, digitized and recorded in order to gain a deep insight of the effect of the sharing phenomena are discussed;
  - a first prototype of a DSSC-type pixel with DePFET readout. A preliminary test with mono-energetic protons and a deep characterization of the single pixels, carried out with the pulsed laser system and including bi-dimensional and one-dimensional mapping as well as the amplitude response characterization as a function of several parameters such as the back voltage, the injected charge, the clear frequency and the injection modality are presented.
- Chapter 5: finally the conclusions and future activities of the work will be stated.

CHAPTER 2

# The characterization suite

With the aim to cover a wide range of injected charge this work is based on two different techniques: the use of monochromatic protons for high levels of charge generation and of pulsed IR laser systems suitable for low and medium injection levels. In the following the characterization suite is introduced, first of all advantages and disadvantages of both the investigated techniques are discussed, then the facilities are described, highlighting the work carried out, in particular the optimization of the laser test suite and the improvement and qualification of the performance of the proton beam source.

## 2.1 A wide range of charge injection level source based on laser IR and mono-energetic protons beam

Laser sources are an efficient tool for the characterization of detector response and in particular for the possibility of mapping the relevant properties of radiation detectors with micrometer resolution. The main advantages of this kind of sources are:

- intrinsic capabilities of accuracy in beam positioning and in time synchronization;

- finely tunable intensity;
- ionization profile inside the bulk quite similar to the ionization profile generated by X-rays and dependent on the wavelength, as shown in Figure 2.1.

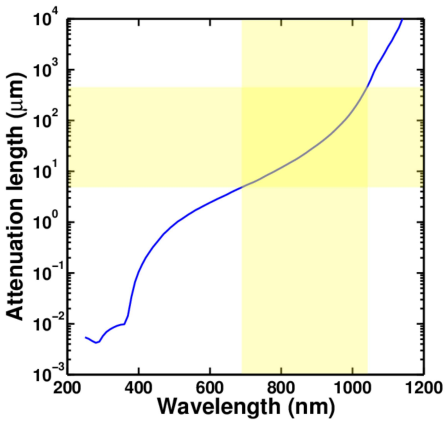


(a) Silicon absorption length in the infrared and visible range as a function of wavelength. Data taken from [40].

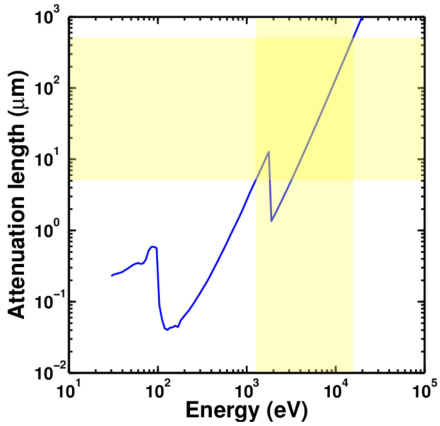


(b) Silicon absorption length in the X-ray range as a function of energy. Data taken from [11] X-ray database.

**Figure 2.1:** *Silicon absorption length in the infrared and visible range (a) and in the X-ray range (b). A region between few μm to few hundreds of μm of the absorption coefficient is highlighted, which corresponds to a wavelength range 700-1050 nm in the near infrared region and to an energy range 1-10 keV in case of X-rays.*

The laser source has also some disadvantages, it can be difficult to calibrate the laser intensity for all the available intensity range. In fact, optical reflection losses and refraction at the considered wavelength can affect the spatial distribution of the generated charge within the detector volume. However at low levels of charge injection absolute calibration of the intensity can be gained with direct comparison with the response to calibration radioactive sources. The typical charge injected per pulse is less than $10^6$ electrons. Therefore the IR pulsed laser is a flexible and accurate probe up to intermediate levels of charge generation.

As an attractive tool to probe the response of the detector-front end system at higher levels of charge injection with high precision in space, time and for different ionization profiles across the detector depth, the possibility of using a pulsed mono-energetic proton beam has been exploited. Figure 2.2 shows the protons projected range in silicon as a function of the proton energy, the range is perfectly matched with the typical thickness of

silicon detectors in the energy range 1 - 6 MeV. Moreover the ionization profile of protons can be tuned from shallow ionization to an extended ionization along the wafer thickness. Figure 2.3 (a) reports the ionization profiles of protons in silicon at different proton energies, as visible in the range 1 - 6 MeV the profile ranges from a depth of 16 $\mu$m (1 MeV) up to 295 $\mu$m (6 MeV). The simulations of the ionization profile of proton in silicon (Figure 2.3 (b)) show both the longitudinal and the lateral range of protons. In the lateral direction the radial range is about 1 $\mu$m at 1 MeV, 4.5 $\mu$m at 3 MeV and 9.5 $\mu$m at 5 MeV, respectively, which sets the ultimate achievable position resolution in the mapping of the detector-electronics response with protons. Moreover by increasing the number of protons in a bunch,

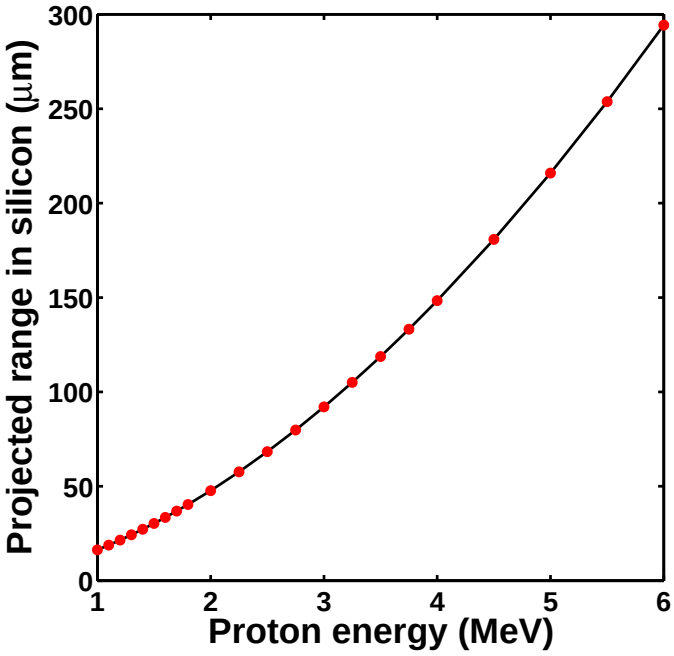


**Figure 2.2:** *Proton projected range in silicon as a function energy.*

it is possible to probe the detector at increasing levels of charge injection. These levels correspond exactly to multiples of the generated charge by a single proton and therefore the total generated charge in the detector is intrinsically calibrated. Being the time duration of a proton bunch (i.e. the spread of the times of incidence of individual protons in the same bunch on the detector surface) much smaller than the detector charge collection time, the detector output amplitude is proportional to the bunch multiplicity. Pro-

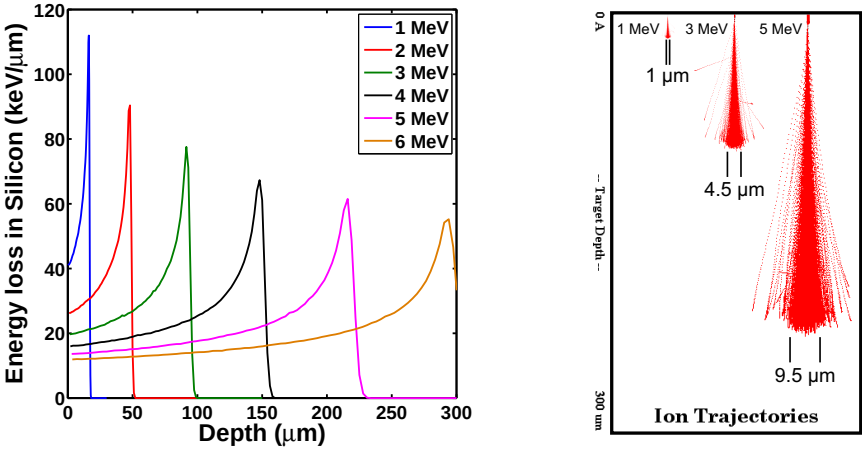


(a) proton energy loss in silicon

(b) proton straggling

**Figure 2.3:** *Proton energy loss in silicon (a); ionization trajectories for different proton energy in silicon (300 μm thick) and corresponding radial range (b). Simulations carried out with SRIM 2013 [41]*

tons are hence suitable for probing the detector and front-end electronics at high, and precisely calibrated, levels of charge generation with high spatial resolution and tunable ionization profile.

## 2.2 The proton-beam facility

In our case the proton beam comes from the 3 MV Tandetron ion accelerator (Figure 2.4) located at the LABEC [42] (LAboratorio di tecniche nucleari per i BEni Culturali), the laboratory of nuclear techniques for cultural heritage located in Sesto Fiorentino, Firenze, Italy and created by the Italian National Institute of Nuclear Physics (INFN). Several facilities are available at LABEC, in particular:

- one AMS (Accelerator Mass Spectrometry) beam line;
- six IBA (Ion Beam Analysis) beam lines. The IBA beam lines can be divided as follows:
  - one external beam line dedicated to Archaeometry (mainly PIXE and PIGE measurements);
  - one external beam line dedicated to atmospheric aerosol measurements;

**Figure 2.4:** *The 3 MeV Tandetron ion accelerator system (of the tandem type) at LABEC, produced by High Voltage Engineering Europa B.V.*

- one external micro-beam line;
- one fast pulsed beam line (DEFEL);
- one beam line dedicated to measurements of particle scattering cross sections;
- one beam line with a multipurpose chamber for in vacuum IBA.

Among all the IBA beam lines, our attention will be focused on the fast pulsed beam line DEFEL (highlighted in Figure 2.5, which shows a scheme of the accelerator hall), which is equipped with a fast electrostatic chopper that allows the creation of a pulsed proton beam [43].

The working principle of the beam line consists in deflecting the continuous beam of the accelerator transversally across a slit, allowing a bunch of ions ($H^+$ or other available ions such $He^{2+}$, $Li^{3+}$ and $C^{4+}$) to proceed downstream through an aperture for a short time interval (of the order of 1 ns). The adjustment of the size of the aperture, with a motorized slit, and of the intensity of the continuous beam, allows the creation of a pulsed beam with a variable and finely controllable number of particles in each pulse (down to an average value much below 1 particle per single bunch). The beam is normally deflected toward a beam stopper and a bunch is created every time a trigger is applied.

The beam, coming from the accelerator, is deflected into the beam line by means of a switching magnet. The central part of the beam is selected by the motorized slit n°1 (typical aperture is below $1 \times 1$ mm$^2$), that is the first element of the beam line, visible from the beam line scheme depicted in

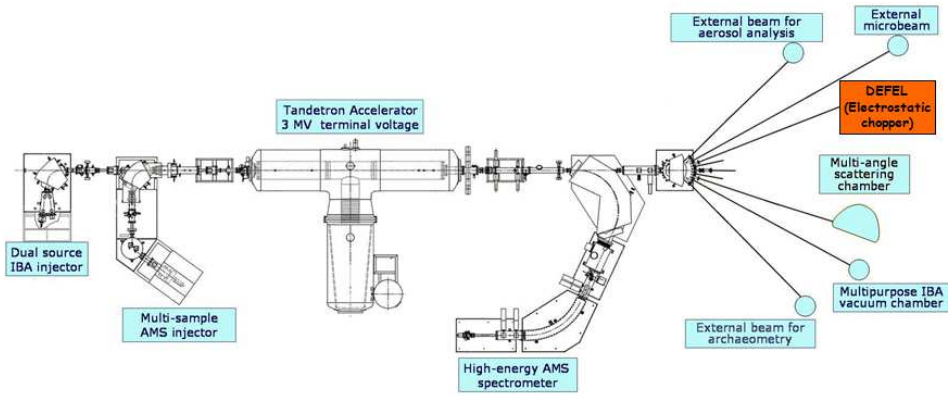


**Figure 2.5:** *Scheme of the beam lines at the 3 MeV Tandetron accelerator at LABEC. The DEFEL beam line is highlighted*

Figure 2.6. Tantalum apertures n°1 and n° 3 (both 4.5 mm $\times$ 19 mm) have been introduced for entering only the zones of uniform field of the deflectors, and at the same time for protecting the isolating support of the plates against accidental hitting of the beam (especially during beam focusing and alignment operations). The tantalum aperture n° 2 (4 mm $\times$ 10 mm) acts as a beam stopper during the phase ON of the predeflector. The monitors are motorized rotating platforms used for diagnostic purposes during the setup phase. Each of them is equipped with a Faraday cup for the beam current measurement and with a quartz crystal for the beam position check. The image on the quartz is remotely observed using a network connected video camera.

The deflector consists of a couple of metal plates (60 cm long, 20 mm wide, 2 mm thick), parallel to the beam line, 5 mm apart from each other; it is placed inside the magnetic quadrupole doublet, used to focus the beam on the final slit. By means of a suitable driving electronics [43] the beam, that is normally deflected to position A (refer to in Figure 2.6) can move to position B by means of a trigger pulse. In particular, the upper plate of the deflector is normally kept at 200 V while the lower one is kept at 100 V (now position A). When a trigger pulse is applied, the electronics driving system set the voltage of the upper plate of the deflector close to ground (now position B). Positions A and B are far from the slit aperture so the beam can enter the chamber only during the voltage transition. The predeflector is mechanically similar to the deflector and also the driving electronics is very similar apart from the value of both the upper plate voltage, 800

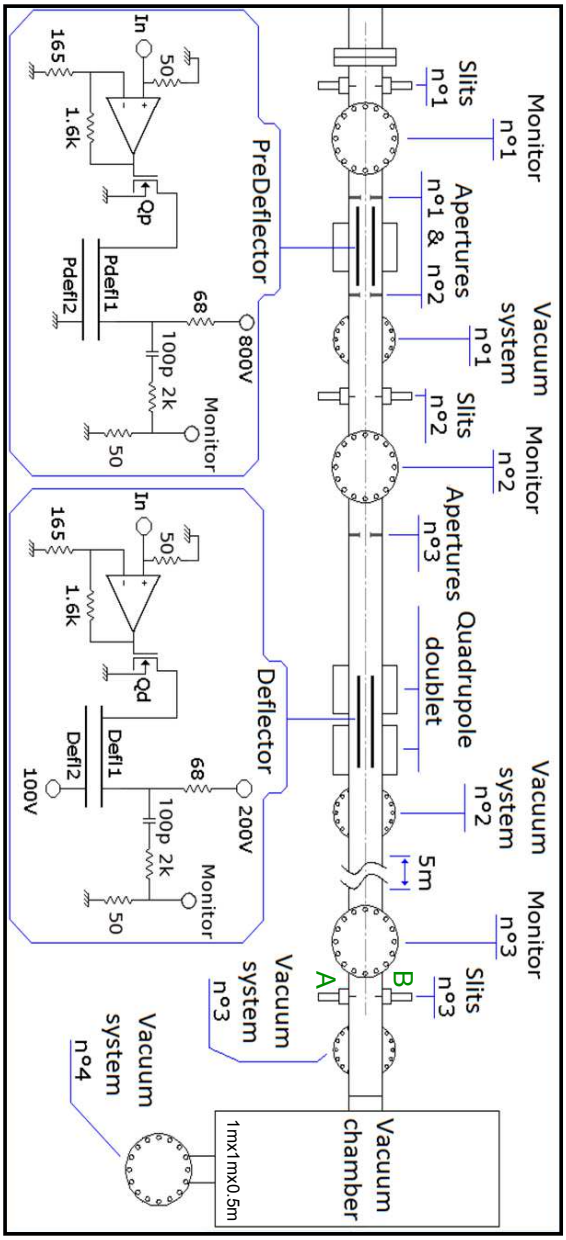


**Figure 2.6:** *Scheme of the DEFEL beam line (not to scale). The picture highlights the motorized slits acting as collimator, rotating platforms (monitor) used for diagnostic purposes, tantalum apertures and high vacuum pumping stations as well as the deflectors with the dedicated driver electronics. At the end of the beam line a big experimental vacuum chamber is available.*

V in this case, and the bottom plate, ground. The beam, that is normally deflected, is allowed to pass undisturbed by means of a short pulse applied to the driving electronics of the deflector and predeflector.

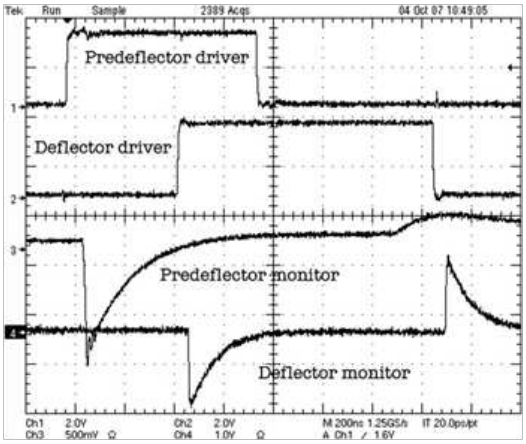


**Figure 2.7:** *Predeflector and deflector signals [43].*

The synchronization scheme of the deflection voltages is shown in Figure 2.7. The deflector pulse starts during the one of the predeflector and ends a fraction of microsecond after it. At the beginning of the cycle, when in the absence of predeflector the beam would hit position A, the upper predeflector plate is kept at a voltage of 800 V and the beam is deflected enough so that it actually hits the tantalum aperture n° 2. The two plates are shortened a fraction of a microsecond before the transition of the deflector: now the beam hits A. The deflector pulse will sweep the beam from A to B, producing the particle bunch when passing over the aperture n° 3. After $\sim$1 $\mu$s the predeflector upper plate voltage is restored and the beam hits again aperture n° 2. As a consequence, the beam is always stopped on aperture n° 2 except for 1 $\mu$s.

By stopping the beam at aperture n° 2 instead of A or B, the predeflector reduces the possible radiation background near the measurements chamber; secondly, it inhibits the beam from passing through the final slit during the reverse transition of the deflector pulse. This automatically selects the leading front of the deflector pulse, which is intrinsically faster due to the driving electronics. Slit n° 2 are anti-scattering slits and are nominally adjusted at the same aperture as slit n° 1: they are a constraint for the beam path, stopping a large part of the particles accidentally scattered by the predeflector plates that would have a chance to reach the measurement chamber along uncontrolled paths.

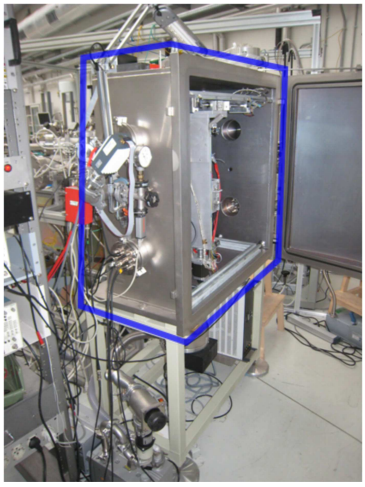

**Figure 2.8:** *The experimental vacuum chamber at the end of the DEFEL beam line.*

The end-station of the beam-line is equipped with a big experimental vacuum chamber (1m×1m×0.5m, Figure 2.8) that houses X-Y movement stages remotely controlled, holding the detector mechanical frame and allowing two-dimensional scans. The mounting frame houses also a silicon p-i-n photodiode detector (Hamamatsu, S3590) for beam intensity adjustment, a quartz glass for precise positioning and alignment of the proton beam and a CMOS imager as beam profile bi-dimensional monitor, recently installed (this latter will be discussed in the following section). An optical camera allows alignment of the proton beam to reference markers on the quartz glass and on the detector chip.

All the following requirements are fulfilled by the DEFEL beam line:

- self calibrated source (no need of a radioactive source for calibration);
- high energy to probe the detector-electronic system at high level of charge injection (proton energy range 1 - 6 MeV, bunches from the single proton to an arbitrary number);
- finely controlled number of particles per bunch.

## 2.3 Upgrade and assessment of the proton beam line performances

In this section the work carried out to improve the DEFEL beam line, in terms of the upgrade of the proton beam spatial properties, is described. Moreover the assessment of the beam line performances, in terms of energy

calibration, spatial and timing resolutions, is presented. These results have been presented in a publication of which I am coauthor [44].

### 2.3.1 Energy calibration

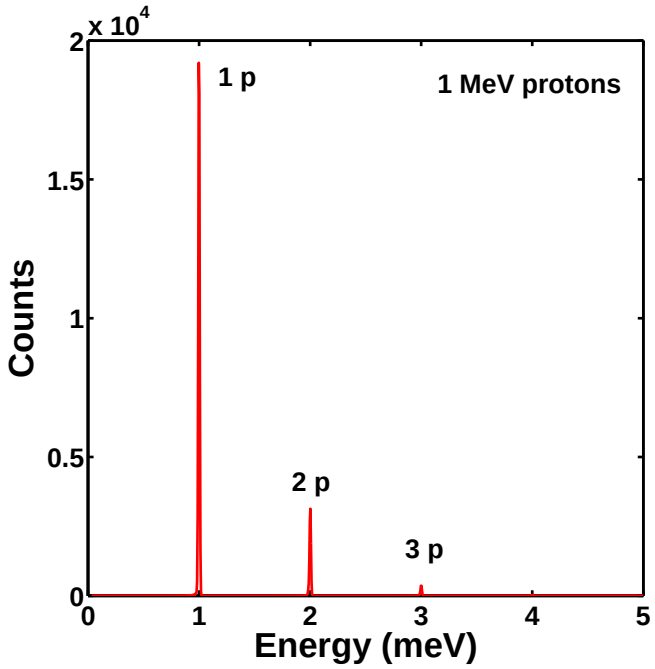


**Figure 2.9:** *Energy spectrum of 1 MeV proton bunches collected with a p-i-n silicon photodiode (Hamamatsu S3590) at the DEFEL beam line.*

Figure 2.9 shows an energy spectrum collected by the silicon photodiode, placed inside the experimental chamber, irradiated with 1 MeV proton bunches. The output signal coming from the p-i-n photodiode is preamplified by a charge preamplifier (Tennelec TC170) and a fast voltage amplifier (ORTEC 572) and digitized with a 500 MSample/s, 12 bit data acquisition system (based on SIS3350 digitizing boards, from Struck Innovative Systeme GmbH). The data are analyzed off-line, baseline subtraction (average of the first 1500 samples) is performed for first, then the amplitude is computed as the maximum of the waveform, filtered with a triangular filter (201 taps). Adjacent peaks are equally spaced (1 MeV) and each peak corresponds to a different bunch multiplicity, up to 3 in this case where the probability of single proton in a bunch has been maximized. By increasing the average beam intensity, distribution of the proton multiplicity can be

easily extended to higher values in order to inject a wider range of charge in the detector. Each peak has been least square fitted with a Gaussian function and the centroid, that is the peak energy $E_{peak}$, is derived. The relative error, calculated with the formula ($E_{peak}$ - $E_{nom}$)/$E_{nom}$, is equal to 0.05%, 0.05% and 0.02% for the nominal energy $E_{nom}$ of 1 MeV, 2 MeV and 3 MeV respectively; hence this spectrum provides an indisputable demonstration of the absolute self calibration of the source.

### 2.3.2 Proton beam spatial properties

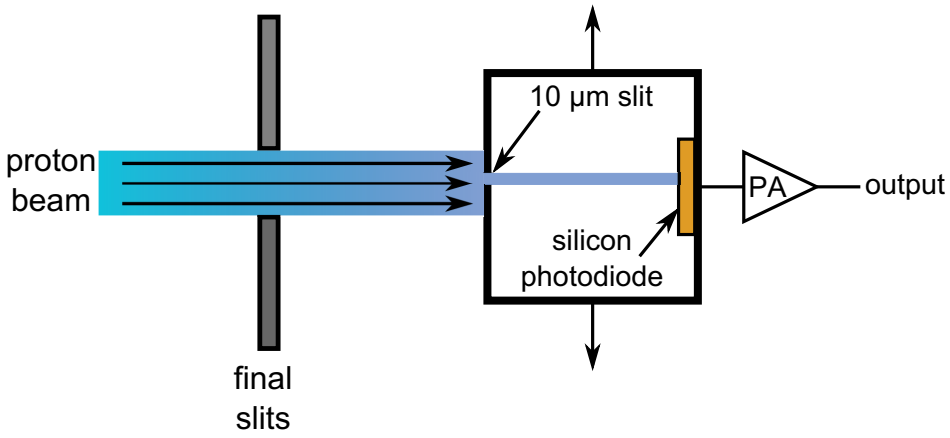


**Figure 2.10:** *Sketch of the experimental setup for the characterization of the proton beam profile with the old beam profiling slits. The final slit n°3 aperture is 100 µm × 100 µm. The beam was scanned by means of a narrow opening (10 µm), at each coordinate a spectrum is collected with a p-i-n silicon photodiode, that is integral with the narrow slit.*

The final slit n°3 define the pulse duration, affect the mean number of particles in the bunch and define the minimum size of the beam, that up to the 2012 was limited to the order of 100 $\mu$m × 100 $\mu$m. Figure 2.10 shows the experimental setup for the characterization of the proton beam profile with the old profiling slits. The final slit aperture was 100 $\mu$m × 100 $\mu$m. The beam is scanned by means of a narrow opening (10 $\mu$m), which can be rotated by 90 degrees and moved with two-dimensional motorized stages, in order to perform a beam scanning in both the horizontal (X) and vertical (Y) directions. At each position of the narrow slit a spectrum was collected by means of the p-i-n silicon photodiode, that is integral with the slit. The spectrum counts were proportional to the intensity of the proton beam.

Figure 2.11 shows the scans of the beam profile along the X and Y directions. The data are least square fitted assuming a Gaussian shape, the

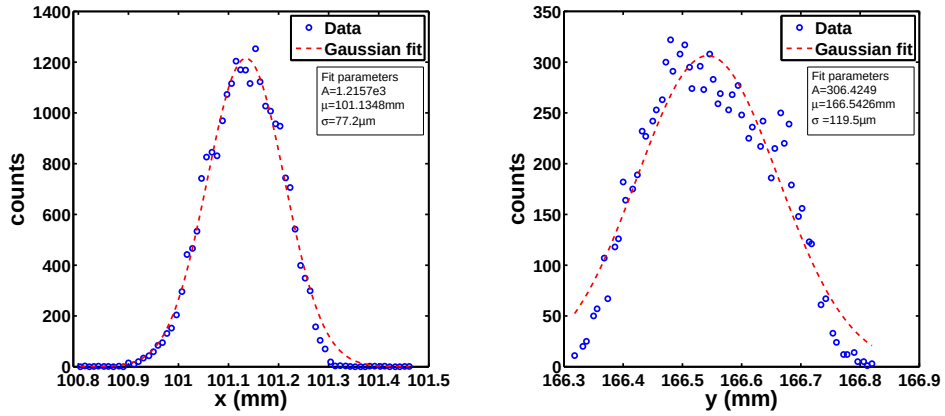


(a) x direction

(b) y direction

**Figure 2.11:** *Beam profile scans along X and Y directions. Dashed lines show the corresponding least square fit according to a Gaussian shape model.*

extracted full width half maximum ($2.35 \cdot \sigma$) is of the order of 100 $\mu$m in both directions.

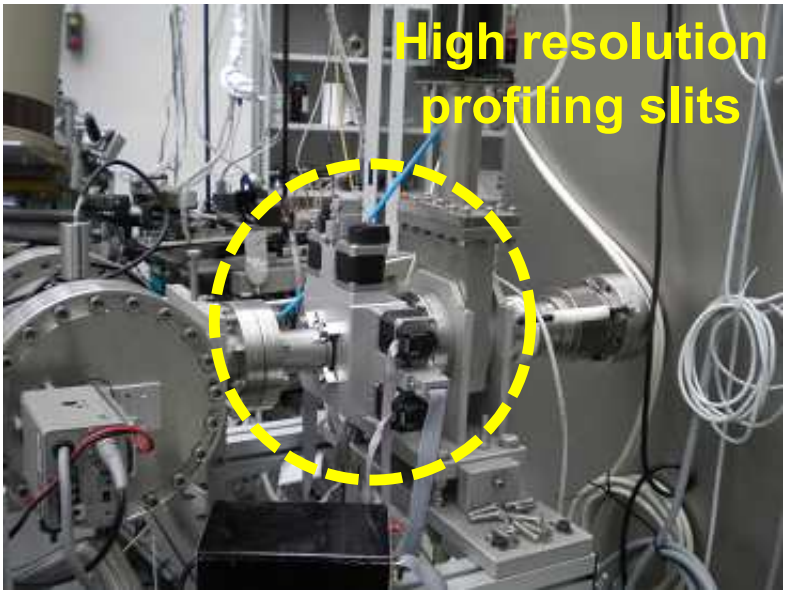


**Figure 2.12:** *The new in-vacuum high-resolution beam profiling slits installed at the DE-FEL beam line (here showed the final slit n°3).*

To overcome this spatial resolution limitation, in the early 2012, the DE-

FEL beam line has been upgraded in terms of spatial resolution and on-line monitoring of the proton beam profile. Standard slits n°2 and n°3 have been replaced with novel remotely controlled in-vacuum hi-resolution profiling slits produced by (JJ X-ray model IB-C30-HV, Figure 2.12). The slits are remotely controlled by a custom made controller, which is described at the end of this section. In order to provide improved on-line beam quality and position assessment, the beam line has been equipped with a CMOS imager (Aptina MT9v034, 752 $\times$ 480 pixels, 6 $\times$ 6 $\mu$m$^2$ pixel size), able to take pictures of the incoming proton bunches. The CMOS sensor is a monochrome one, 1/3-inch optical format, the active imager size is 4.51 mm (H) $\times$ 2.88 mm (V), 5.35 mm diagonal. The protecting glass has been removed in order to allow the protons to reach the sensor surface. The Aptina sensor board is interfaced with a BeagleBoard xM board by means of two different interfaces: a parallel interface for the image data transfer and an I$^2$C interface for the sensor programming. The BeagleBoard, which operates inside the DEFEL experimental chamber in vacuum, is cooled with metal pillars that act as heat sink, they thermally connect the integrated circuits of the board (by gluing them to the package with a thermal conductive glue) to the metal body of the experimental vacuum chamber.

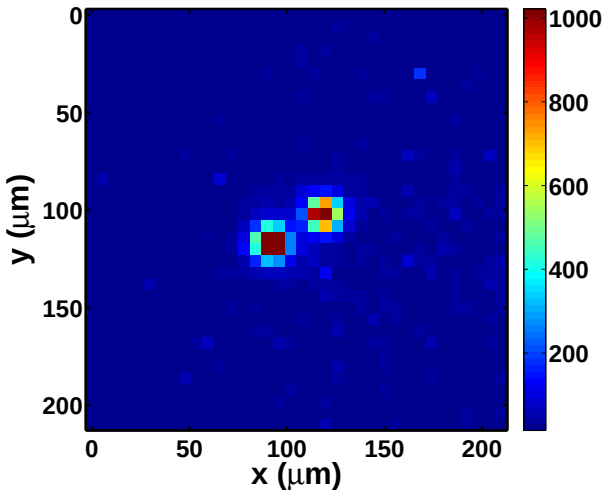


**Figure 2.13:** *Single shot picture of proton bunches (CMOS exposure time 62.5 ms, DEFEL trigger @ 500 Hz).*

By means of the CMOS image sensor the spatial properties of the proton beam (1 MeV proton energy), after the upgrade of the beam line, have

been qualified. Figure 2.13 report a single shot image of a bunch with two protons, the color map is the pixel intensity in dimensionless units.

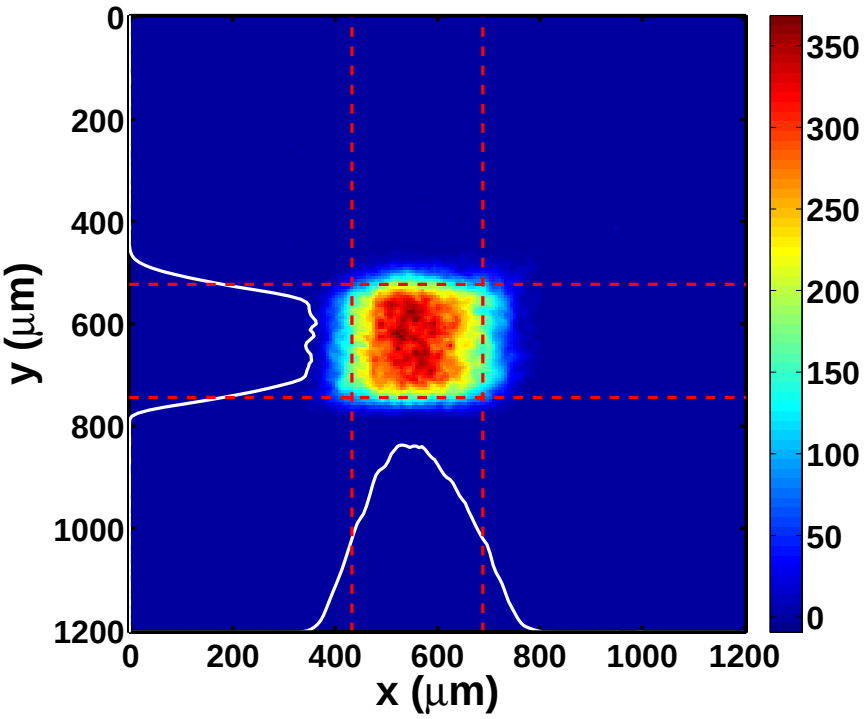


**Figure 2.14:** *Two-dimensional profile with a 200 $\mu$m $\times$ 200 $\mu$m opening of the final slit n°3 (CMOS exposure time 62.5 ms, DEFEL trigger @ 500 Hz). The white lines are the projections of the 2-D picture onto the x and y axes, the red dashed lines define the FWHM of the profile, that is 254 $\mu$m $\times$ 220 $\mu$m.*

Summing of several snapshots allows the observation of the full two-dimensional beam profile. The profile picture is obtained adding single frames and normalizing to the number of frames. Dark-frame subtraction technique has been applied to minimize image noise (noise from the sensor, dead or hot pixels).

Figure 2.14 shows the two-dimensional profile corresponding to an opening of 200 $\mu$m $\times$ 200 $\mu$m of the final slit n° 3.

The single picture can be projected onto the x and y axes and the uni-dimensional profiles analyzed to evaluate the full width half maximum (FWHM) of the beam in both directions. The computation of the FWHM has been performed by considering a threshold at half between the maximum and minimum values of the uni-dimensional profile. The threshold

crossing spatial coordinate is achieved with a linear interpolation of the uni-dimensional profile values immediately under and above the threshold. Performing this analysis the resulting beam size is 254 $\mu$m $\times$ 220 $\mu$m, greater than the 200 $\mu$m $\times$ 200 $\mu$m opening of the final slit. In addition there is a slight asymmetry, being the beam larger in the x direction. The uni-dimensional profiles and the FWHM are superimposed to the beam image in Figure 2.14.

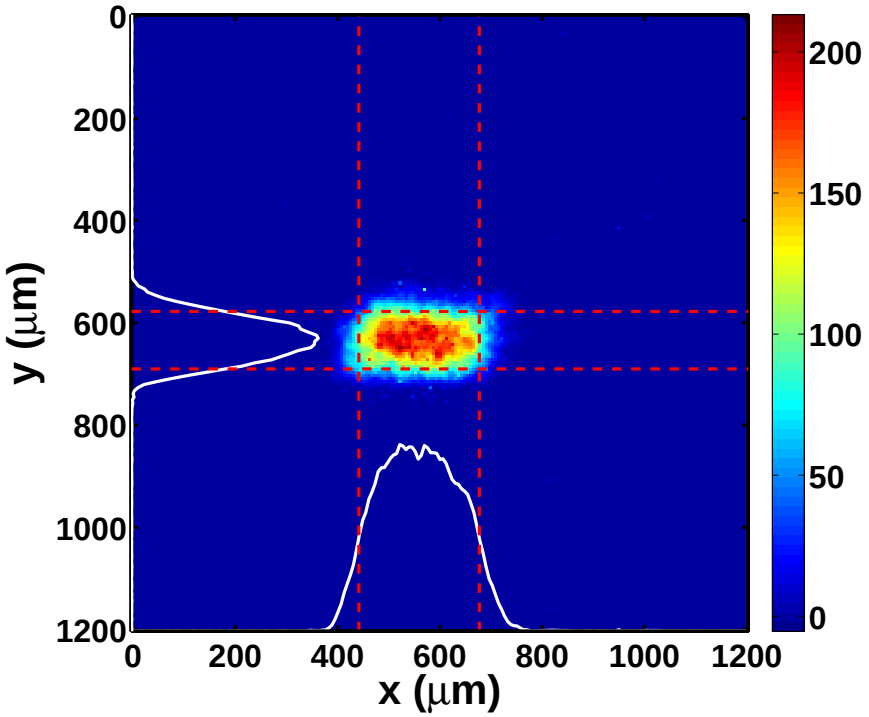


**Figure 2.15:** *Two-dimensional profile with a 100 $\mu$m $\times$ 100 $\mu$m opening of the final slit n°3 (CMOS exposure time 62.5 ms, DEFEL trigger @ 500 Hz). The white lines are the projections of the 2-D picture onto the x and y axes, the red dashed lines define the FWHM of the profile, that is 234 $\mu$m $\times$ 112 $\mu$m.*

A second two-dimensional beam profile is showed in Figure 2.15, obtained with a 100 $\mu$m $\times$ 100 $\mu$m opening of the final slit, halved with the aim to shrink the beam. Observing the picture a great asymmetry of the profile becomes immediately evident; along the y direction a great narrowing is obtained, on the other hand along the x direction the profile is quite the same of the above discussed case. Quantitative confirmation is given by data analysis, with a profile size of 234 $\mu$m $\times$ 112 $\mu$m, the x size is quite

unchanged while the y size is pretty much halved.

The following considerations can be drawn:

- the relation between the beam profile and the final slit opening is different for the x and y directions;
- narrowing the final slit opening does not necessarily lead to a corresponding shrinking of the proton beam;
- the proton beam spatial properties depend on all the components of the beam line (profiling slits n°1 and n°2, quadrupole doublet and so on, refer to Figure 2.6), hence the beam narrowing, operating just with the final slit, is not straightforward.

Aim of the present work is not so much the investigation of the beam profile spatial properties in relation to the parameters of the DEFEL beam line as to highlight the usefulness of the CMOS imager as a beam profile optimization tool. As previously stated in 2.2 the quadrupole doublet is used to focus the proton beam, the driving currents can be set independently to separately have effect on the x and y directions of the beam orthogonal plane. The focus of the beam can obviously make the final slit more or less effective, depending on the focus coordinate, that can be different for the x and y directions, along the beam propagation direction.

Attempting to optimize the beam profile in the x direction the quadrupole current has been spanned from 1.8 A to 1.4 A, keeping a fixed final slit opening equal to 50 $\mu$m $\times$ 10000 $\mu$m. The effect of the current on the spatial properties of the beam can be immediately evaluated with the CMOS imager. Setting the current to 1.8 A (Figure 2.16), to 1.6 A (Figure 2.17)and to 1.4 A (Figure 2.18), a beam shrinking along the x direction, respectively to 133 $\mu$m, 82 $\mu$m and finally 62 $\mu$m, has been achieved.

A Further optimization has allowed to obtain, for this first qualification after the beam line improvement, a beam spot down to 65 $\mu$m $\times$ 42 $\mu$m (Figure 2.19) with a 30 $\mu$m $\times$ 30 $\mu$m final slit opening. This is an acceptable result compared to the old spatial properties, however the spot size can be further improved by means of the systematic study of the beam line parameters and of the beam line optics.

#### 2.3.2.1 The remote controller of the beam profiling slit

A custom made controller, designed and implemented at LABEC, Firenze, provide remote control of the beam profiling slits. Each slit has four blades, named TOP, BOTTOM, LEFT, RIGHT, hence four stepper motors. The controller provide 4 motor drivers and is capable to control a single slit.

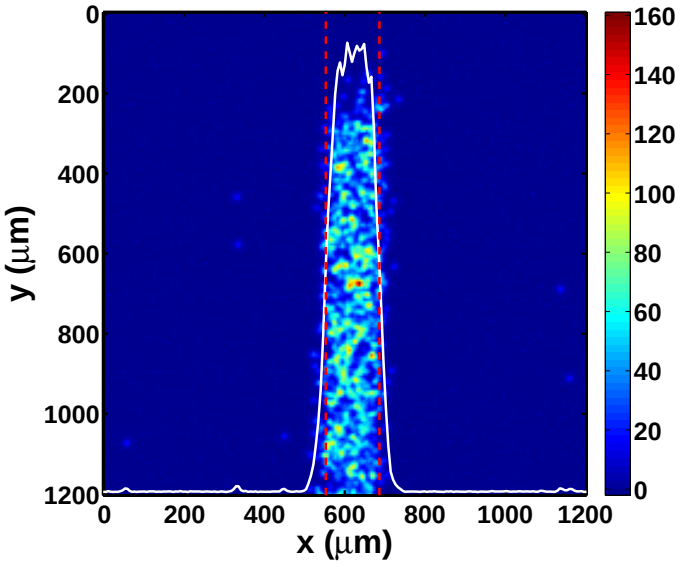


**Figure 2.16:** *Two-dimensional profile with a 50 μm × 10000 μm opening of the final slit n°3, quadrupole current set to 1.8 A. The FWHM along the x direction is 133 μm (CMOS exposure time 62.5 ms, DEFEL trigger @ 100 Hz).*

Three novel remotely controlled hi-resolution profiling slits, produced by JJ X-ray, have been provided: two are in-vacuum slits with motors equipped with incremental encoders and have been installed at the DEFEL beam line (as previously described in 2.3.2, p. 37), one is an in-air slit (JJ X-ray model IB-C30-AIR) without the encoders and has been installed in our laboratory in Politecnico di Milano in order to enhance our X-ray imaging system based on a X-ray table-top Mo-anode source tube. The original version of the custom made controller, suitable just for encoders-equipped slits, has been optimized in order to extend its use to slits with motors unprovided of the encoder.

Figure 2.20 shows the scheme of principle of the controller. The whole system is based on a RCM3200 RabbitCore® microprocessor core, that provides a 10/100Base-T Ethernet communication interface, and is composed of two boards, one called MOTHERBOARD and a second acting as frontal DISPLAY. The MOTHERBOARD houses the 4 motor drivers, generates the signals suitable for controlling the motor drivers as well as the clock signal for the proper operation of the counters and the programmable waveform generators (the integrated circuits LS7366R and AD9833BRM respectively) and the bias voltages for the motor drivers, the microproces-

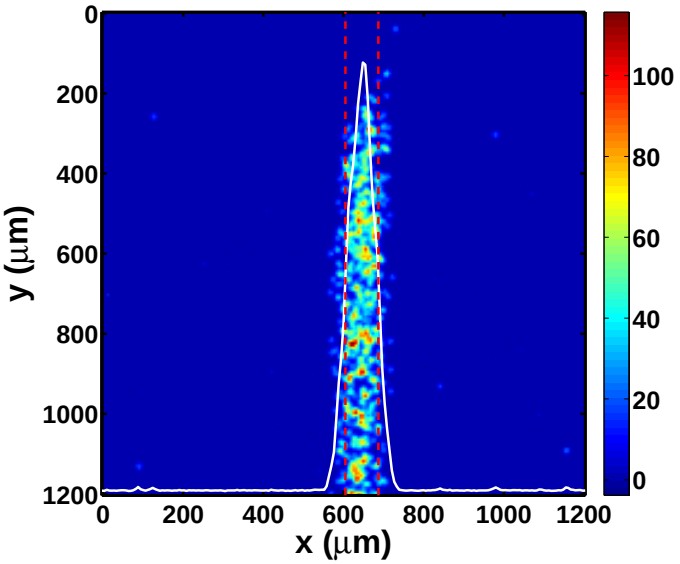


**Figure 2.17:** *Two-dimensional profile with a 50 μm × 10000 μm opening of the final slit n°3, quadrupole current set to 1.6 A. The FWHM along the x direction is 82 μm (CMOS exposure time 62.5 ms, DEFEL trigger @ 100 Hz).*

sor core, the integrated circuits and the encoders, and receives the end of travel (EoT) and encoder (if available) signals from the motors. The DISPLAY board provides numerical information about the position of the four blades as well as push buttons for manual motion. Each position is displayed by five 7-segments led displays, driven by a led display driver integrated circuit (MAX6955), the most significant digit corresponds to tens of millimeters and the least significant to micrometers. When the position of one of the four blades must be changed, the microprocessor instructs the programmable waveform generator to generate a square waveform, with a number of periods depending on the desired travel, that is the input of the motor driver. This latter, receiving also the enable and the DIR (direction of the motor motion) signals from the microprocessor, moves the stepper motor according to the travel range and direction imposed by the user. The motor provide EoT signals, managed by the microprocessor, and, if available, the quadrature outputs from the incremental encoders. In the old version of the controller the encoder outputs were fed directly to the counter, a chip providing both quadrature and non-quadrature up/down counting features. In the new version of the controller, in case the stepper motors are not provided with encoders, the output signal (square waveform ) from the

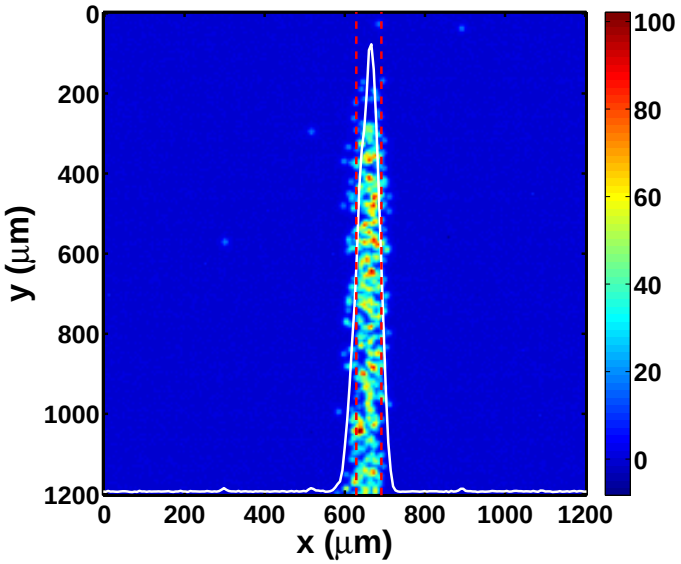


**Figure 2.18:** *Two-dimensional profile with a 50 μm × 10000 μm opening of the final slit n°3, quadrupole current set to 1.4 A. The FWHM along the x direction is 62 μm (CMOS exposure time 62.5 ms, DEFEL trigger @ 100 Hz).*

programmable waveform generator is used to keep track of the slit position. Obviously, without the encoders, no feedback is provided by the motors in this case. Thanks to the digital buffers 1 and 2 the counter can be alternatively fed with the encoder output, in this case acting as quadrature counter, or with the waveform generator output and the DIR signal, acting as up/down counter. Buffer 1 and 2 are enabled by a logic signal provided by the microprocessor, the arrangement of the two logic inverters makes the simultaneous enabling of the two buffers impossible, i.e. two different signals can not be simultaneously connected to the counter inputs. The microprocessor communicates with the counter by a serial interface, obtains the relative movement of the blade and calculates the current position, that is sent to the DISPLAY board. This latter provides also an interrupt to the microprocessor in case one of the buttons for the manual motion is pressed.

This controller has been assembled and tested, resulting fully functional, at LABEC, Firenze, Italy, with the invaluable help of Dr. Luca Carraresi, Università degli studi di Firenze, Dip. di Fisica e Astronomia and INFN Firenze. Figure 2.21 shows a photo of the controller connected to the in-air model profiling slit. The front panel, with position displays and push buttons for manual motion provided for each blade, is visible.

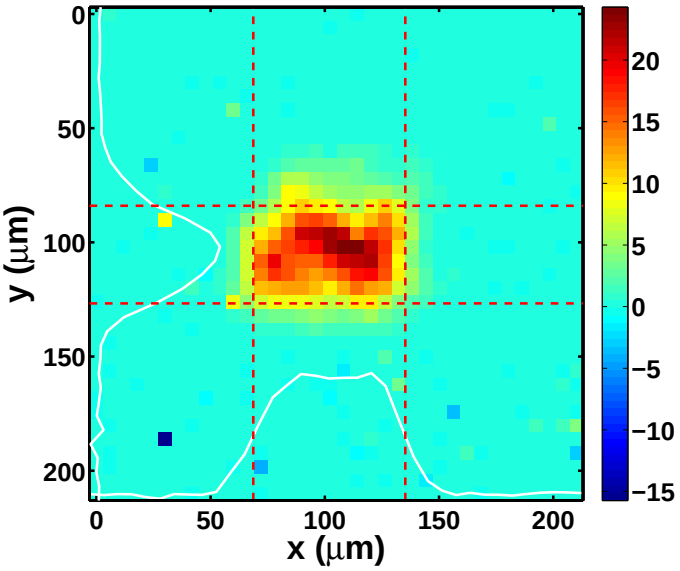


**Figure 2.19:** *Two-dimensional profile with a 30 μm × 30 μm opening of the final slit n°3. The beam spot is 65 μm × 42 μm (CMOS exposure time 62.5 ms, DEFEL trigger @ 500 Hz).*

The firmware of the controller has been implemented with a set of commands, that can be sent to the microprocessor via Ethernet, providing all the necessary functions (absolute or relative movement of each individual blade, get current position and so on) needed for the remote control of the instrument. A graphical interface, that is suitable for the management, via Ethernet interface, of the slit controller with a remote PC, has been developed in LabView® language. Figure 2.22 shows a screenshot of the developed software, whose functions are described in the following:

- communication: the user sets the slit controller IP address and receives a feedback from the software, that indicates the successful connection with the controller, and the PC communication port and IP address used;

- slit position: this is the main section of the software, it provides, for each axis, the current position and motion status, absolute and relative movement functions, the end of travel status and the possibility to set the current position as 0. The software logic acts in such a way that it is not possible, for the user, to input a movement command when an axis is already traveling. In this section are provided also the following

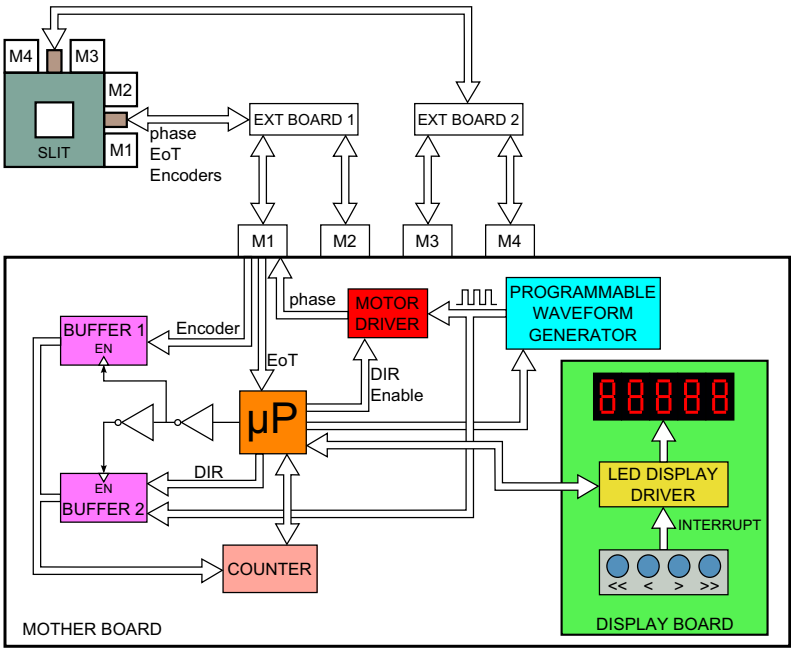


**Figure 2.20:** *Scheme of principle of the new version of the custom made controller for the profiling slits, optimized for the use with both slits equipped with/unprovided of the encoders. For sake of clarity the scheme, that is the same for the 4 stepper motors of the slit (except the microprocessor obviously, that is one , refers just to a single motor.*

functions:

  - positions storing: store and recall a slit position of interest (10 slots available);
  - motor on/off;

- global relative movement: this is a particular section that provides the possibility to perform a relative movement of more than one axis at the same time. This is a useful feature, for example, if one wants to perform a scan moving the slit with fixed aperture.

### 2.3.3 Time jitter qualification

The jitter of the time of arrival of the proton bunch is another key figure of merit for the DEFEL beam line, in order to open the way to probing the transport dynamics of the charge carriers in radiation detectors with accurate time resolution. A fast trigger signal, well synchronized with the proton bunch, is provided by the beam line itself and is the *predeflector monitor* (Figure 2.7, p. 34).


**Figure 2.21:** *Photo of the controller and the profiling slit (in-air version, JJ X-ray IB-C30-AIR model).*

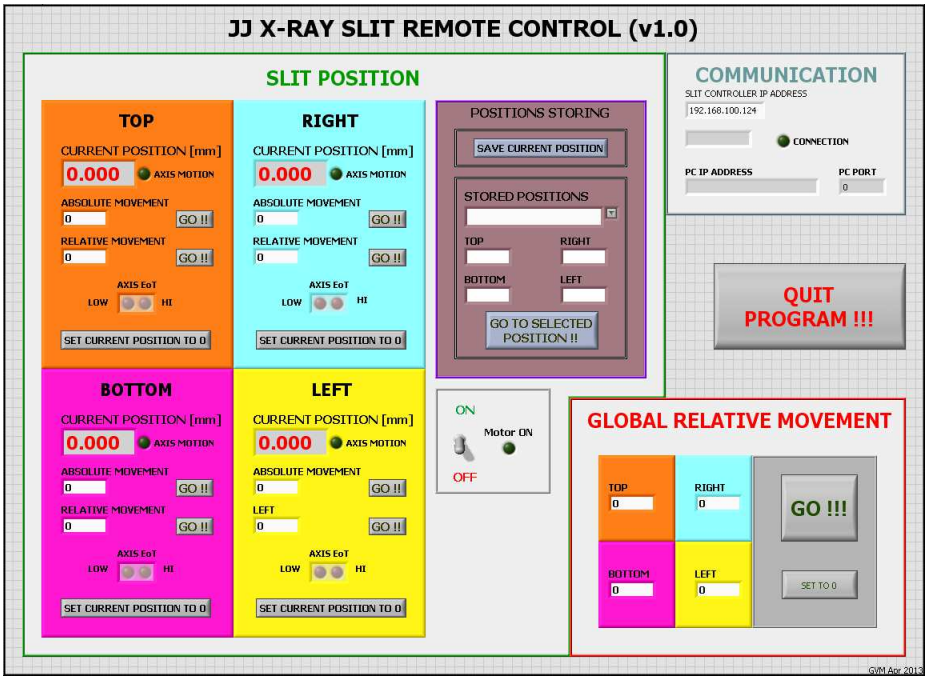


**Figure 2.22:** *Screenshot of the LabView® interface developed for the remote control, via Ethernet, of the slit controller.*

The qualification of the time jitter has been carried out by measuring the time difference between the time of arrival of the trigger signal and the occurrence of a signal from a silicon p-i-n photodiode detector (Hamamatsu, S3590) in the case of 1 MeV protons interaction. The time jitter is caused by the slightly different paths traversed by the incoming protons. The most critical condition arises from the 1 MeV protons because they are the slowest (the velocity is proportional to the square root of the proton energy), hence the difference between the travel time of different paths is greater. Moreover two different experimental setups have been arranged, one based on a Constant Fraction Discriminator (CFD) technique, the other based on a threshold discriminator and a Time Digital Converter (TDC).

Figure 2.23 shows a sketch of the CFD based measurement setup. A p-i-n silicon diode interacts with the proton bunch, the signal is amplified by a charge preamplifier and a fast voltage amplifier and fed to one input of the digital data acquisition system (DAQ), which consists of a SIS3350 digitization board (4 channels, 0.5 GSample/s max, 12 bit). The acquisition

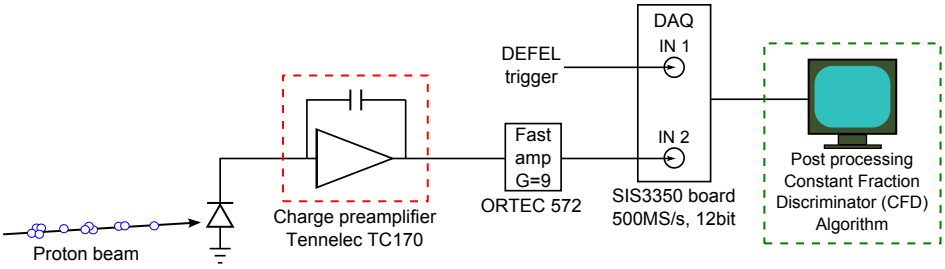


**Figure 2.23:** *Constant Fraction Discriminator (CFD) experimental setup for the DEFEL time jitter qualification.*

is triggered by the DEFEL trigger signal, connected to the other input; both the amplified diode signal and the trigger signal are digitized at 500 MSamples/s sampling rate (see Chapter 3, p. 59, for a full description of the DAQ system) and the data are streamed to the remote PC for post processing analysis by means of a constant fraction discriminator algorithm. The DAQ code on PC acts differently on the two waveforms. Regarding the trigger signal, after baseline subtraction (average of the first 1500 samples), the threshold is calculated as the 50 % of the maximum. For the calculation of the threshold crossing time the data are upsampled with an upsampling factor of 2, then a third degree polynomial fit is performed on seven samples centered on the named "crossing sample", defined as the first sample above the threshold. The threshold crossing time is calculated as the intersection between the polynomial and the threshold. Regarding the diode output

waveform the baseline is first subtracted (average of the first 1500 samples). The maximum is calculated on the baseline-subtracted-waveform after processing with a digital triangular filter (201 taps). The baseline-subtracted-waveform is then processed with a digital triangular filter (7 taps) and the threshold crossing time is calculated like in the previous case, but defining the threshold as the 40 % of the maximum.

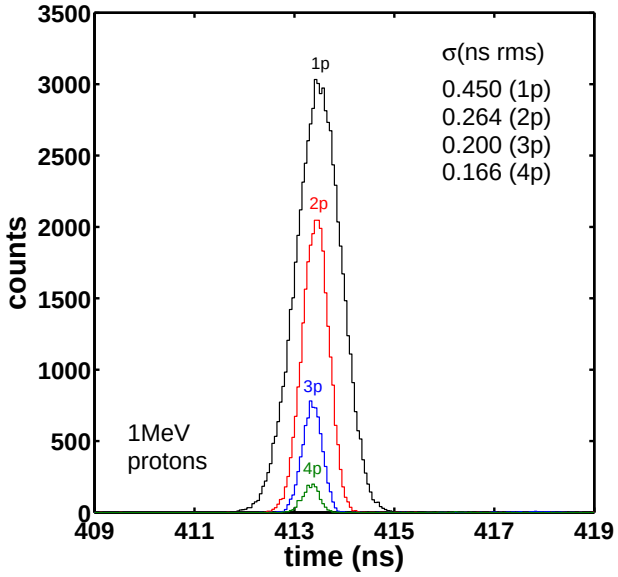


**Figure 2.24:** *Time difference histograms between the photodiode output signal and the DEFEL trigger signal for 1 MeV protons obtained with the data digitization and the subsequent application of the CFD algorithm. The rms standard deviations of a Gaussian fit are indicated.*

Figure 2.24 shows the time difference histogram in case of 1 MeV proton bunches; the different distributions correspond to bunches with different multiplicity (from 1 to 4 protons, the amplitudes are separated via software), with the relative rms standard deviation (derived from a least square Gaussian fit) taken as time jitter. The jitter is always below 0.5 ns, and the better results are achieved with the 4 proton bunches, when the electronic noise is less relevant because the higher slope of the detector signal. The histogram does not show any evidence of amplitude walk, confirming the goodness of the CFD algorithm.

The TDC based system, presented in Figure 2.25, is slightly more complex. Regarding the interaction with the proton beam the arrangement is the same as in the previous case, except for the negative fast amplifier gain.

The time difference measurement is performed at a hardware level by a time digital converter. This latter converts in a digital code the time elapsed between a start and a stop signal. The start signal is given by the DEFEL

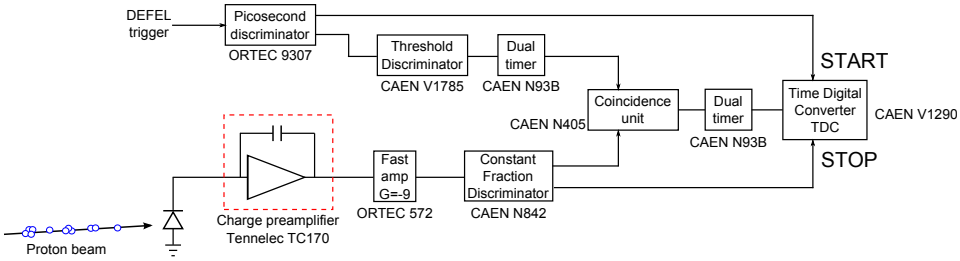


**Figure 2.25:** *Threshold discriminator and Time Digital Converter (TDC) experimental setup for the DEFEL time jitter qualification.*

trigger by means of a constant threshold fast Picosecond discriminator. The stop signal is provided by the silicon detector (amplifier output). The DEFEL trigger and the detector signal drive also a coincidence unit, which enables the TDC only in case of the simultaneous occurrence of the two signals, in order to avoid the case of a trigger occurrence (TDC start signal) with no proton hitting the detector (TDC stop signal).

Figure 2.26 shows the time difference histogram obtained with the TDC based qualification, still in case of 1 MeV protons. The very good performance achieved with the previous test are confirmed, again the time jitter is below 0.5 ns. In this case the amplitude walk is clearly visible, introducing a beneficial separation effect that allows the TDC to distinguish between bunches with different multiplicity.

Some final considerations about these two tests can be discussed observing Figure 2.27, that summarizes the standard deviations (i.e. the time jitter) as a function of the number of protons per single bunch for the two qualification modalities. The TDC based test shows better results with a small number of protons per bunch, but increasing the number of protons the CFD results are the more performing. A possible explanation relies in the different instrumental noise of the two equipments.

Considering the time jitter inversely proportional to the signal amplitude (given by the number of protons $N_P$) the standard deviation can be expressed as $\sigma = A/N_p$. However, there is also a contribution from the noise added by the measurement equipment, this latter can be considered, as a first approximation, independent from the signal amplitude and can be taken into account by means of the addition of a constant term: $\sigma = A/N_p + INSTR_{NOISE}$.

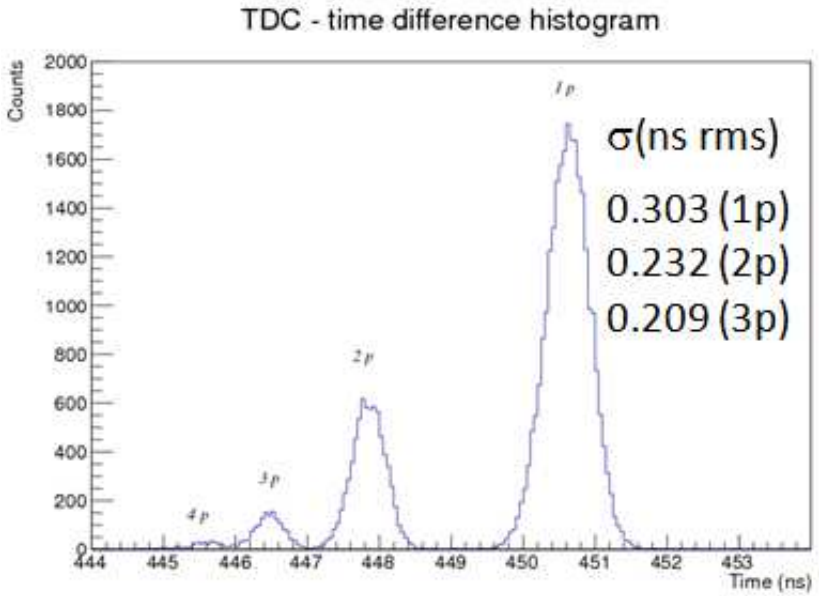


**Figure 2.26:** *Time difference histograms between the photodiode output signal and the DEFEL trigger signal for 1 MeV protons, obtained with the TDC based experimental setup.*

Least square fitting the data according to this expression allows to determine the A coefficient and the instrumental noise contribution, that is, referring to Figure 2.27, the horizontal asymptote of the data fit. The CFD based system shows a lower instrumental noise. The A coefficient instead represents the sensitivity of the measurement equipment to the number of protons per bunch, in this case the TDC based system shows the better performance.

## 2.4 The laser test system

For testing low levels of charge injection (less than $10^6$ electrons) a facility based on an infrared laser system is available in our laboratory in Politecnico di Milano. The laser driving unit is a Pico Quant PDL800-D model that allows for repetition rates up to 80 MHz. The IR laser test system features two interchangeable laser heads with wavelengths of 905 nm ($\pm$ 10 nm) which assures an absorption length in silicon of about 54 $\mu$m at room temperature, and of 705 nm ($\pm$ 10 nm) that features an absorption length in silicon of about 7 $\mu$m at room temperature, though a large variety of wavelengths exist to probe the detector with different ionization profiles.

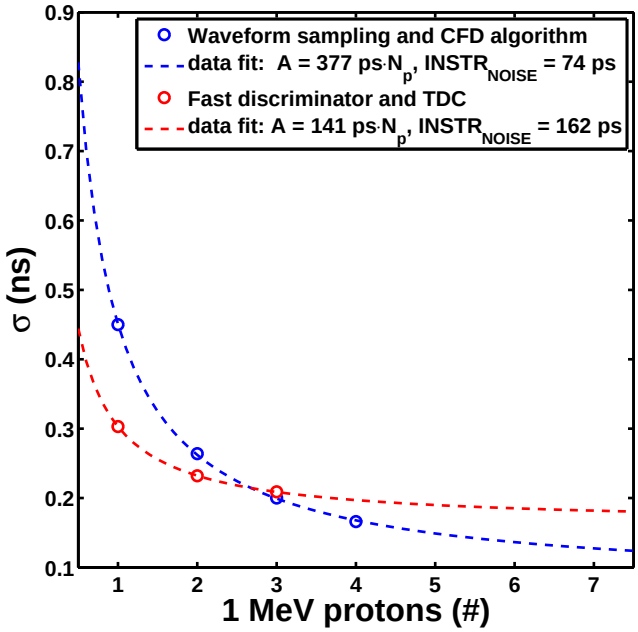


**Figure 2.27:** *Time jitter standard deviation as a function of the number of protons per single bunch for the two qualification modalities.*

In Figure 2.28 there is a photo of the setup housed in a $1m^3$ shielded chamber, this latter placed on an optical table. The setup is equipped with motorized X-Y stages (two Newport linear stages, controlled by a Newport controller remotely connected via GPIB to a pc) with micrometer precision that allow a fine beam positioning. A microscope with two eyepieces slots is then mounted in front of the detector. In one eye-piece slot there is the optical fiber (single mode optical fiber with core/cladding diameter 6/125 $\mu$m) that guides the laser pulse. In the other one an IR sensible camera helps in beam positioning. A 20x objective focuses the laser pulse on the surface of the detector under test, and an optical illuminator is available, for objective-detector focus distance optimization.

The shielded box is provided with electrical feedthroughs for the detector signals and DC voltages, the slides and camera cables. The laser fiber optic is brought inside by means of a separate shielded hole.

In order to determine the laser spot size a direct measurement has been carried out using the known fine aluminum strip pattern present on the anode side of a prototype of Multi-Linear Silicon Drift Detector (MLSDD) [23]. In particular the intensity profile has been measured by means of a

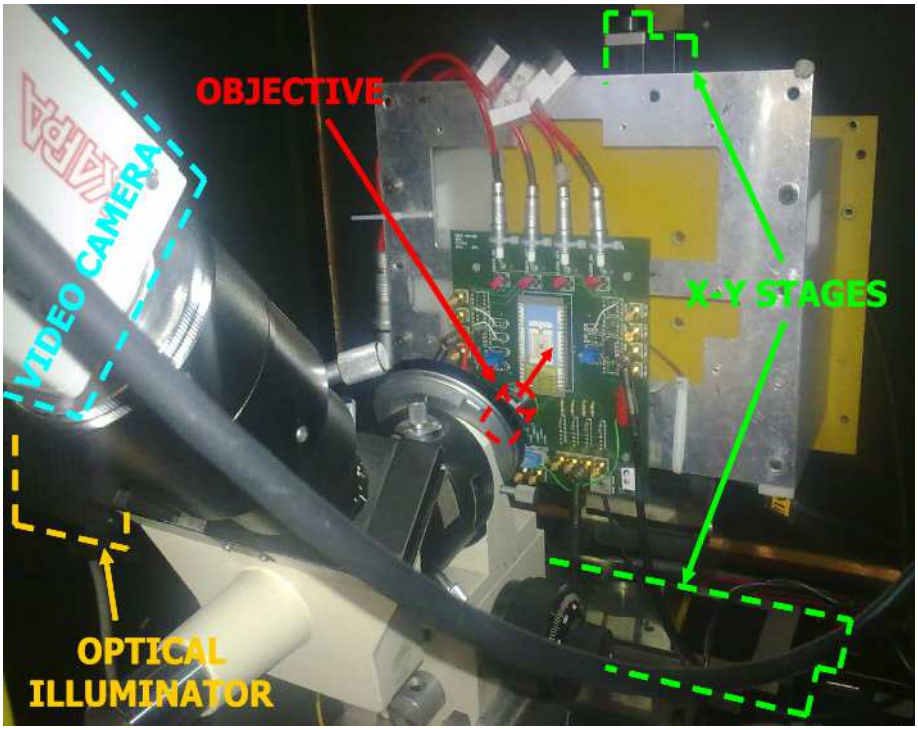


**Figure 2.28:** *Photo of the IR laser test suite setup inside the shielded experimental chamber.*

fine scanning (1 $\mu$m step), and profiting of the different reflective properties of the aluminum strips on the detector surface with respect to the strips implanted in naked silicon the transmittance curve of the detector surface has been modeled as negligible for the metal covered detector surface and as unitary for the naked silicon area. Figure 2.29 shows the intensity profile, that is the result of the convolution between the laser spot intensity profile and the transmission curve. The resulting FWHM of the laser, assuming a trapezoidal profile of the spot, is of the order of 10 $\mu$m, well suited as a fine probe for in-pixel scans.

The facility provides also high timing accuracy, with sub-nanosecond pulse duration, as qualified from a test (Figure 2.30) carried out with a Si-SPAD - Single Photon Avalanche Photodiode [22].

A dedicated LabView® code allows launching scans (both in the lateral and longitudinal directions) of the detector surface. The charge generated in the bulk of the detector by the laser radiation gives an output signal that is pre-amplified by readout electronics. The pre-amplified signal is fed into into a 5-poles pseudo Gaussian shaper and its unipolar and bipolar outputs

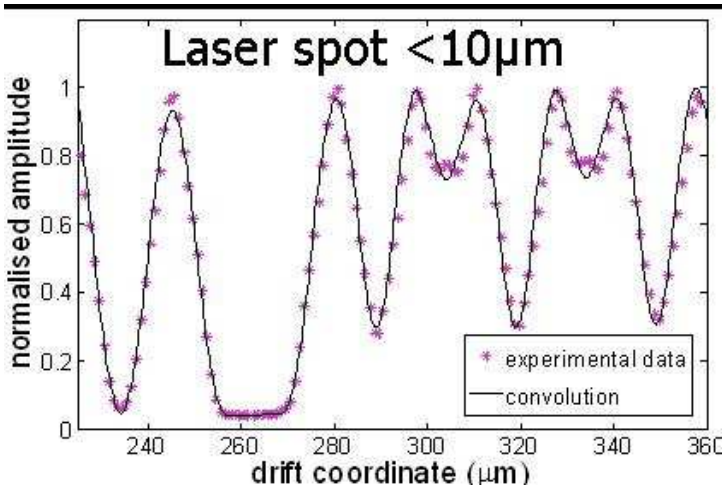


**Figure 2.29:** *Qualification of the laser spot size.*

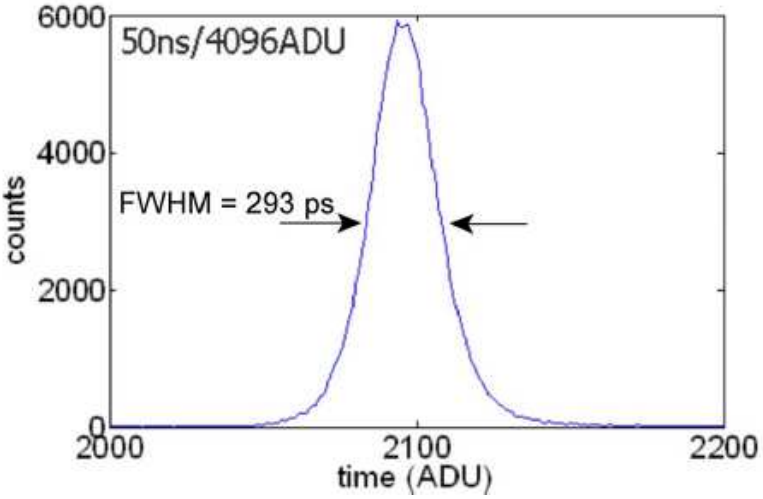


**Figure 2.30:** *IR laser output pulse time-dependence measured with a fast SPAD. The FWHM is 293 ps*

are digitized by an oscilloscope (Tektronix TDS 540D, 8 bit, 500 MHz analog bandwidth, sampling rate up to 2 GSample/s), connected remotely via GPIB to the acquisition pc. From the digitized data the Labview® software extracts the amplitude, from the unipolar shaper output, and the collection time, from the bipolar shaper output; these parameters, with the corresponding spatial coordinates, are stored in a file, while the acquired waveforms are discarded.

Recently, new motion stages, with different travel ranges, have been purchased in order to expand the system and make it more flexible and adaptable to the test of different radiation detectors, each one mounted in a different setup (the size of the electronic boards as well as the mechanical frame housing the detector vary case by case) with different requirements. These new motion stages are not compatible with the controller that is already part of the facility, so a new one has been purchased. In addition the facility has been improved with the introduction of a better performing oscilloscope (Tektronix DPO 4104, 8 bit, 1 GHz analog bandwidth, sampling rate up to 5 GSample/s).

The installation of both the new controller and the new oscilloscope has required further development of the LabView® software in order to make it compatible with the new instruments. In addition the software has been improved, and now the digitized waveforms can be stored to disk for off-line analysis. In Figure 2.30 there is a screenshot of the developed software.

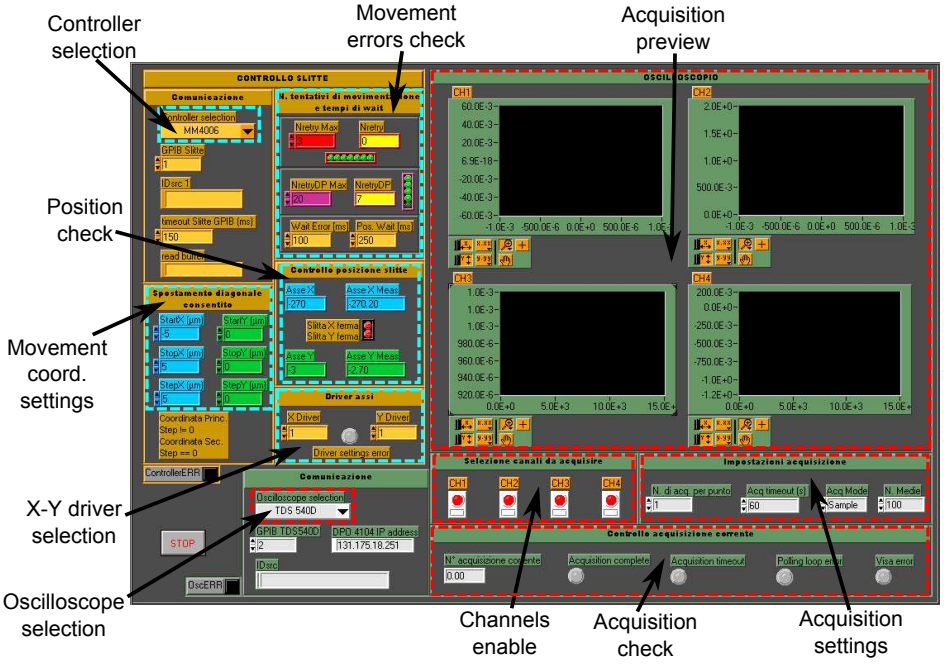


**Figure 2.31:** *A screenshot of the developed software for the remote control of the laser test suite instruments dedicated to the motion and acquisition. The motion section is in yellow-earth, the oscilloscope section is the green one. The main features are highlighted (cyan for the motion section, red for the acquisition section).*

Two colors distinguish the motion section (yellow-earth) from the acquisition section (green). The main features of the software, highlighted in

Figure 2.30, are described in the following:

- movement stages and controller
  - controller selection: it is possible the selection of both the two controllers, depending on the motion stages housed in the shielded chamber. This feature adds more flexibility, the user can freely install any couple of X-Y motion stages inside the shielded box, depending on the needs of the detector under test;
  - X-Y driver selection: a controller provides different types of driver outputs, and each motion stage must be connected with a compatible output. Because the variety of available stages, they are not compatible with all the different driver outputs. With this feature the user can choose the output driver connected to the corresponding X axis and Y axis motion stages;
  - movement errors check: the software checks the occurrence of an error (for example a communication error with the controller) during the axis motion and, after a number of attempts to complete the motion without errors stops the execution;
  - movement coordinate settings: here the user can set the start coordinate, stop coordinate and the step for both the X and Y axes;
  - position check: this feature reports the current position of the stages, in addition the software checks if the current position is equal to the desired position, if not stops the execution;
- oscilloscope:
  - oscilloscope selection: it is possible the selection of the new oscilloscope (DPO 4104) as well as the old one (TDS 540D);
  - channels enable: the user can chose the oscilloscope channels that will be digitized and stored to disk;
  - acquisition check: the software stops the execution in case of the occurrence of an error (a communication error with the oscilloscope, a timeout during the acquisition...);
  - acquisition settings: different options can be set, the number of acquisitions performed at each position coordinate, the acquisition mode (sample, average), and the acquisition timeout;
  - acquisition preview: the acquired waveforms are plotted in a live preview during the acquisition.

CHAPTER 3

# Development of a general purpose multichannel digital data acquisition system

A general purpose multichannel system is versatile and suitable for the different foreseen experimental situations, especially the case of charge sharing among adjacent detector channels, which may be more noticeable at high levels of charge generation. As example, in a two-dimensional pixelated matrix detector, at least 9 channels are needed in order to probe one pixel and the eight first neighbors.

Moreover the acquisition of the full shape of the output signals allows to gain deeper knowledge of the detector behavior. An example is the knowledge of the real pulse at the anode of the detector (directly correlated with the charge cloud) achievable by means of a dedicated deconvolution algorithm.

The development of a general purpose, multichannel, Data Acquisition (DAQ) system has been carried out during this PhD research activity. In this chapter the developed system will be described in detail (both from hardware and software point of views) and, finally, the first functionality tests will be presented.

## 3.1 Hardware description

The DAQ system is a fundamental element that acts as interface, with high temporal precision, from one side with the trigger signal, from the other side with the readout electronics of the detector.

Such a system should, in fact, be able to digitize a number of channels of the detector, according to a preselected trigger pattern, and to transfer the gathered data to the remote PC.

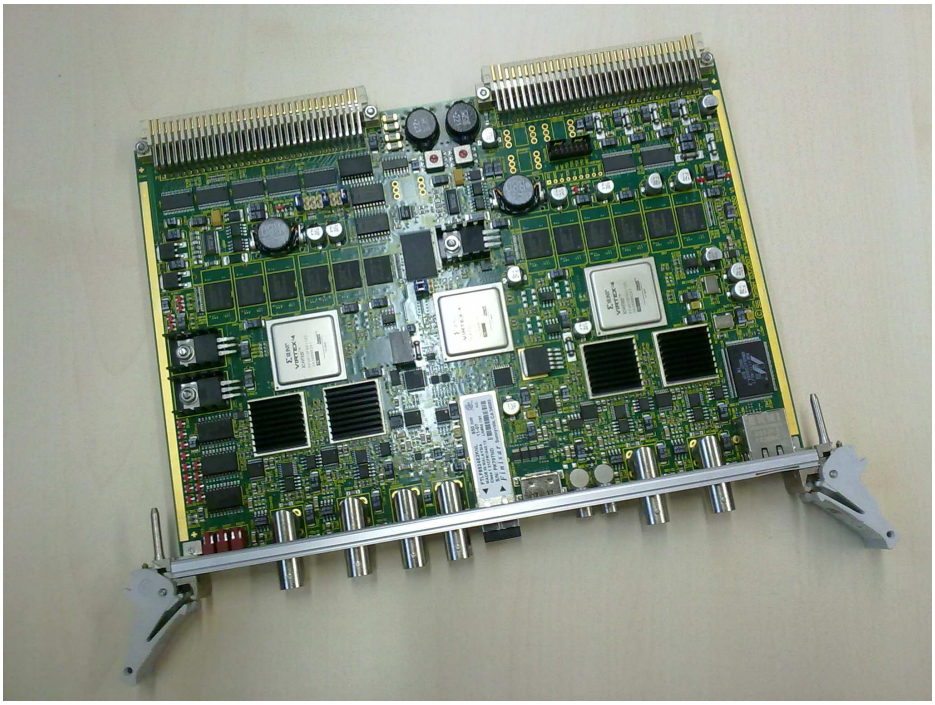

**Figure 3.1:** *A photo of the SIS3350 digitization board.*

The SIS3350 digitization boards (Figure 3.1), produced by the SIS GmbH (Struck Innovative Systeme), are the main components of the DAQ system. They have been chosen, for the implementation of the system, given their usage flexibility. The main features of these modules are a maximum sampling rate of 0.5 GSamples/s (2 ns of sampling period) and 12 bit resolution.

The reason for this choice relies mainly in the right compromise between the requirement of an adequate sampling frequency, suitable to acquire sufficient signal information (typical signal rise times are of the order of 10 ns, compared to 2 ns of sampling period) and still maintain a good resolution.

Each SIS3350 board provides:

- 4 acquisition channels;
- BNC Clock IN connection: each board can be externally clocked;
- BNC Clock OUT connection: each board provides an external clock signal that can be fed to other boards for synchronization purpose;
- LEMO TRIG IN connection: an external trigger signal (both NIM or TTL levels are accepted) can be provided via lemo connector;
- LEMO TRIG OUT connection: each board can provide an external trigger signal, that can trigger other boards in the data acquisition system;
- HDMI connector: this connector is suitable for both providing and feeding standard LVDS (Low Voltage Differential Signaling) clock and trigger signals;
- Ethernet and optical link connections for communication purpose.

All these features make the boards very versatile and suitable for different hardware configurations. The external BNC clock and LEMO trigger inputs accept analog input signals for maximum flexibility.

The clock can be generated internally, from an on board 100 MHz quartz (fixed clock) or by means of a frequency synthesizer with programmable frequency up to 0.5 GSamples/s, or provided externally. In the latter case the internal logic signal is generated on the board from the comparison of an external periodic signal with a programmable threshold (BNC external clock). An external clock signal, according to the standard LVDS, is a further alternative. The trigger modalities are various; firstly an auto trigger,

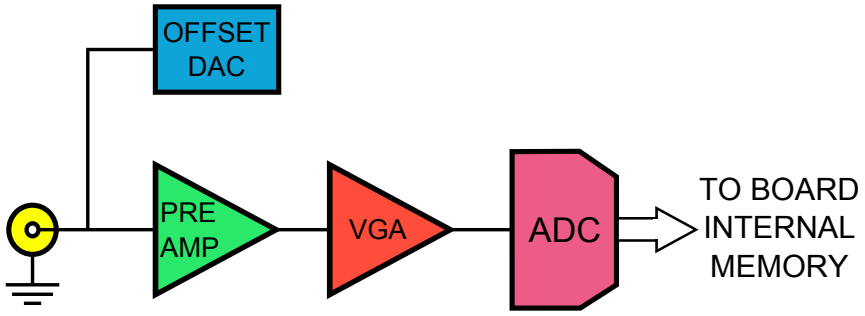


**Figure 3.2:** *A sketch of the electronics of a SIS3350 individual channel.*

adjustable separately on each of the 4 acquisition channels, is available in threshold (both greater than or lower than conditions are available) or FIR

modes. The first mode is sensitive to the level of the signal, the latter is sensitive to the slope. Secondly, an external trigger (provided by the LEMO TRIG IN connector) with digitally programmable threshold and finally an external LVDS trigger are also available.

On each channel, as depicted in Figure 3.2, there are a 12 bit ADC, a 16 bit offset DAC, a preamplifier and a Variable Gain Amplifier (VGA). The offset DAC and the VGA, programmable by the user, adjust the signal level to the dynamic range of the ADC. The stream of digitized data from the ADC chips, when a trigger condition occurs, is recorded to the board internal memory, which is 128 MSamples per channel. This large amount of memory allows recording very long duration waveforms with very short sampling period, for example with 0.5 GSamples/s sampling rate a time interval of $\sim 0.25$ seconds, with a resolution of 2 ns, can be recorded.

The overall hardware consists of the well described acquisition boards, communication boards, remote PC and connection cables (Figure 3.3). The SIS3350 boards are connected via VME Bus A32 D32 MBLT64read (40 MByte/s), with a SIS3100 bridge, produced by SIS (Struck Innovative Systeme) GmbH, which acts as VME-PCI interface, via optical fiber (optical link 10 GB/s), for the communication with remote PC. This latter is equipped with a SIS1100 PCI bridge, produced by SIS (Struck Innovative Systeme) GmbH.

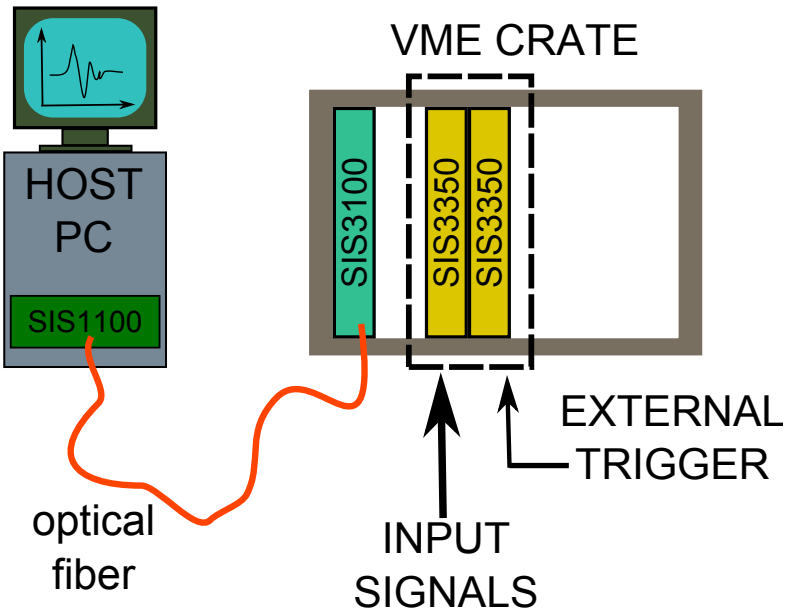


**Figure 3.3:** *Sketch of the DAQ hardware.*

In Figure 3.4 there is a picture of the system, that up to now is composed of 8 channels, i.e. two SIS3350 digitization boards (limited by the available hardware). The boards can be connected and triggered in different configurations thanks to the flexibility provided by the management software developed for the DAQ, that will be described in the following.

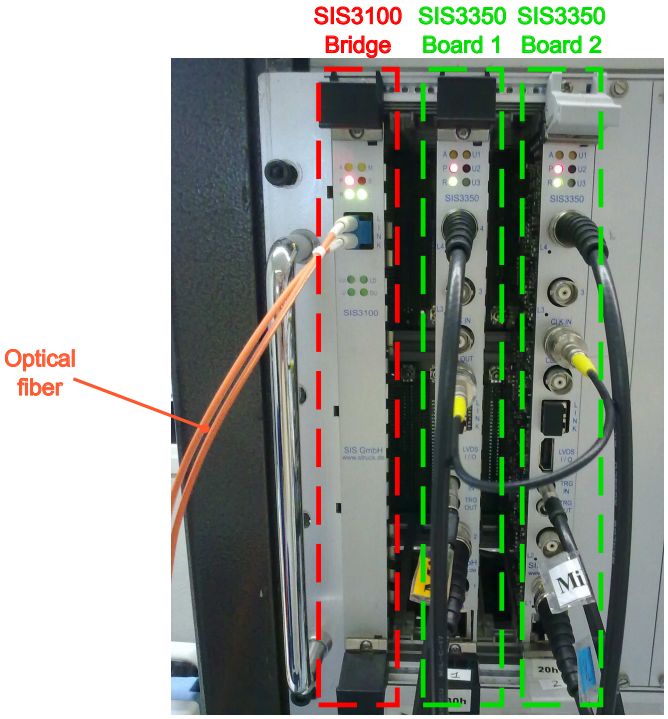


**Figure 3.4:** *A photo of the DAQ system. The SIS3100 bridge and the two SIS3350 digitization boards are highlighted.*

## 3.2 The DAQ management software

Several points have been considered in the development of the management software for the DAQ system. First of all the input modality offered to the user, developed in such a way to guarantee the maximum user friendliness and, at the same time, the possibility to take advantage of the different configurations and options offered by the digitization boards. Another point is the management of the acquisition, which consists of different procedures like arming the on-board acquisition logic, waiting for the end of the acquisition or, possibly, for an external interrupt provided by the user, performing an error check and giving an appropriate feedback in case of an error oc-

curs. Also the management of the digitized data that are streamed from the boards internal memory to the remote PC has been taken into account obviously, considering also the file format used to record the data to the PC disk and other stuffs like the implementation of a graphical live preview of the acquisition and the writing of a log file.

The dedicated configuration-control software, aimed at the management of the whole DAQ system, is written in C language and is designed to accomplish the aforementioned features. Essentially, the software can be described as consisting of the following three sections:

- the configuration of the system;
- the acquisition management;
- the data transfer-storing;

which are exposed in the following.

### 3.2.1 User input settings

The development of this section has been very tricky because the six modes of operation implemented by the firmware of the SIS3350 boards. Each of these operating modes provides different options and has different features, including:

- synchronous or asynchronous acquisition. In the first case the 4 individual channels start the acquisition simultaneously when a trigger occurs, which can be the external (global) trigger or the auto trigger (on a single channel), while in the second case the acquisition is triggered just on the channel when the auto trigger occurs and the individual channels acquire data asynchronously;
- the available memory for the acquisition of a single waveform, that ranges from 16 kSamples up to the entire memory size (128 Msamples) depending on the modality of operation;
- the available trigger modalities, for example the asynchronous modes do not allow the external trigger but just the auto trigger on single channels.

In case of a general purpose system the key word is flexibility, which means a wide number of options offered to the user, in order to have the possibility to adapt the system to different experimental conditions. This complicates the matters in the case of an input text file (the choice made for this project),

since the options available to the user are conditioned by the choice of a particular mode of operation.

More than that, in order to create a multi-board system, the use of asynchronous modes is not possible obviously, because to synchronize the acquisition of all the boards together an external trigger is needed, this latter not available in asynchronous mode as previously discussed.

Consequently some board arrangement configurations have been *a priori* selected, each one with a dedicated input text file. This is a compromise between software complexity, that grows by increasing the number of the implemented hardware configurations and the related input files, and to guarantee user friendliness (dedicated input files are easier to understand and fill) and the availability of different hardware configuration chances. The following configurations are supported:

- usage of a single SIS3350 board among the ones inserted in the system;
- multi-board system, in one of the following configurations (see Figure 3.5):
  - multi-board 1: synchronous acquisition, triggered by a common external master trigger;
  - multi-board 2: synchronous acquisition, with the trigger source located on a single board (external or auto trigger) and then distributed to the other boards of the system.

The software generates a menu with the configuration options outlined above, depending on the actual number of boards in the system. This latter is known through a text file that lists all the boards installed in the system, providing in particular the following information for each module:

- the VME address, that must be different for each board obviously, is determined by the user by means of a rotary switch on the board;
- an ordinal number, determined by the user but different for each board (checked by the software), that is suitable to unequivocally and clearly identify the module.

In this way the software is very adaptable to the hardware modifications (number of SIS3350 boards and their address) and it can support the inclusion of a reasonable number of additional modules in the DAQ system (limited for example by the slots of the VME crate).

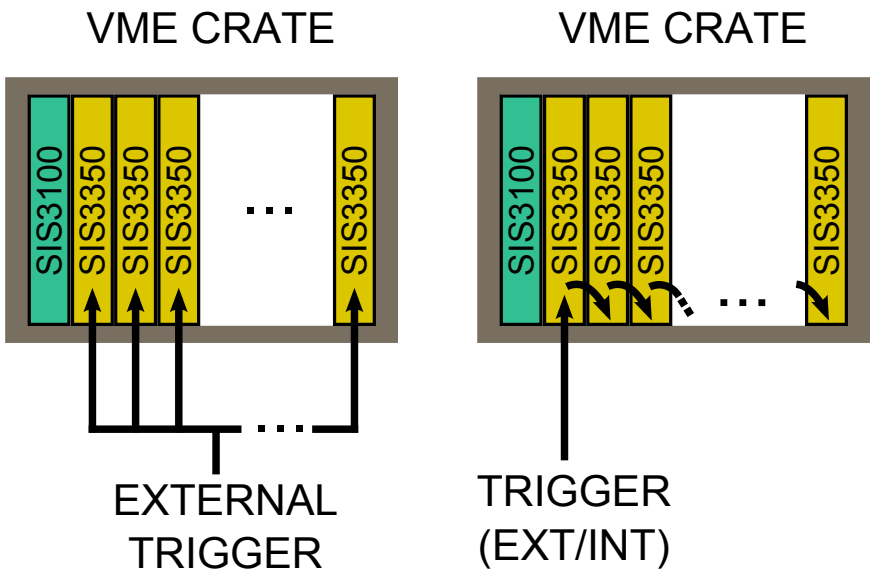


(a) multi-board 1 configuration (b) multi-board 2 configuration

**Figure 3.5:** *The two multi-board configurations managed by the software.*

Depending on the hardware configuration selected in this first step the software generates the input files suitable for the particular configuration. The software has been implemented in such a way to make available all the six modes of operation in the case of usage of a single board and to restrict the choice to just two modes in the case of a multi-board arrangement. It has been also considered to streamline the notation by generating two different input files: the first one allows parameters related to the acquisition to be set (i.e. the mode of operation of the board, the digitized waveform sample length, the gain and offset of each individual channel and so on); the second one is generated according to the choices made in the first one and allows setting the trigger input modality and the distribution of the trigger and clock signals in the case of multi-board system.

In particular the first input file, sketched in Figure 3.6, provides the following options:

- acquisition mode settings: the user can select one of the available modalities (that are six in case of single board system and two in the multi-board case) and operating modality related options;

- clock settings (available just in case of single board system): the user selects the clock source among the available four, if the frequency

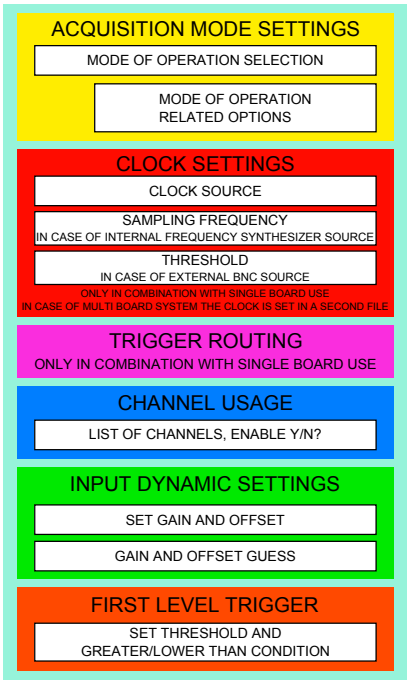


**Figure 3.6:** *Sketch of the first input file available to the user to set the DAQ system.*

synthesizer is selected the user must specify the frequency, while, in case of external clock provided via BNC connector, the threshold must be set. In case of multi-board system the clock settings are demanded to the second input file;

- trigger routing (available just in case of single board usage): the routing from any trigger input (external, LEMO or LVDS, or auto) toward any of the trigger outputs (LEMO or LVDS) is possible. In case of multi-board system this option is disabled, the trigger routing is managed by the software in case of the multi-board 2 hardware configuration, which foresees the distribution of the trigger from board to board;

- channels usage: the user can neglect one or more unused channels, in order to prevent the transfer and the storage of useless data and to save transfer time and disk space;

- input dynamic settings: in this section the offset and the gain of each individual channel are set in order to adjust the input signal to the dynamic range of the ADC. The offset and the gain are expressed as

dimensionless numbers (a value from 0 to $2^{16} - 1$ for the 16-bit offset DAC and a value from 0 to 255 for the variable gain amplifier). In addition the software is able to provide a guess for the offset and the gain values by the insertion of the expected high and low levels (expressed in Volt) of the sampled signal, with the aim to make the dynamic setting as simple and fast as possible for the user. A characterization of the input offset and gain has been carried out in order to implement this feature (see 3.2.1.1, p. 70);

- first level trigger: during the experiment the occurrence of empty events is possible. In order to avoid these events to be recorded and to save data transfer time and disk memory, the user can set a first level trigger condition (typically a discrimination threshold). In particular a single threshold discrimination has been implemented, with greater than or lower than condition.

In case of multi-board configuration this first input file is generated for each board installed in the system. A second input text file, that allows to set the trigger as well as the clock in case of multi-board system, is then generated. The content of this file is dependent on the choices made in the first file and on the selected hardware configuration.

Regardless of the number of modules, this second input file is generated only once and it contains options that are valid for all the modules in the system. Figure 3.7 shows a sketch of the structure of the second input file. The availability of the options depends on the hardware configuration, as stated in the follows:

- in case of single board system:
  - auto trigger settings on each individual channel: the auto trigger can be independently enabled for one or more channels of the board, with different trigger conditions for each individual channel. The available trigger modalities depend on the previously selected mode of operation;
  - external trigger settings (available just in case of previous selection of a synchronous mode of operation): the user can enable both the external LVDS trigger source and the external trigger provided via LEMO connector, this latter foresees also the setting of the threshold;
  - output trigger pulse length: when the trigger (auto or external) is routed toward one of the board trigger outputs, the length of the output pulse is customizable;

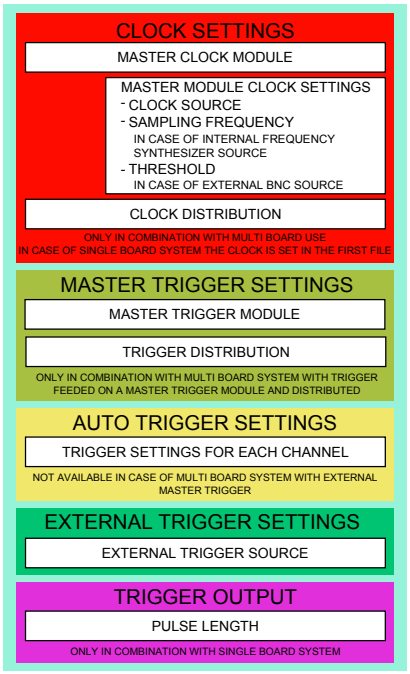


**Figure 3.7:** *Sketch of the second input file available to the user to set the DAQ system.*

- in case of the multi-board 1 system (external common master trigger) only the external trigger is available, furthermore the user can set the options regarding the clock distribution. In more detail:
  - clock settings: the user can define one of the boards as the *clock source module* and the clock distribution mode (BNC cable or LVDS standard), regarding the *clock source module* the clock source is selected among the 4 available options;
  - external trigger settings: the same options described before for the single board case, they are set up just once and are valid for all the modules installed in the system;
- in case of the multi-board 2 system (trigger source located on a *master trigger board* and then distributed to the other modules) the input file is slightly more complex:
  - clock settings: these options work like in the multi-board 1 configuration;
  - master trigger board settings: one of the SIS3350 modules is set as the *master trigger board*, the acquisition is triggered by a trig-

ger source (auto or external trigger) on this board. The trigger is then distributed to the other boards via LEMO or LVDS, defined by user;

– auto/external trigger settings: these settings work like described above for the single board case and they refer just to the previously defined *master trigger board*.

All the input files provide suggestions to the user, default values when possible as well as guidance on the acceptable minimum and maximum values, for the options that require a numerical value. More than that, once it is filled by the user, the software analyzes the file showing a summary of the settings, alerting the user if one or more errors are found (bad compilation of the file) and asking to fix them. The software, after analyzing the input file and finding it with no errors, converts the user settings into the appropriate digital words and uploads the SIS3350 board logic.

Once the boards have been initialized with the options set by the user an acquisition graphic preview is showed, acting as a feedback for the user settings, which may be adjusted as necessary.

#### 3.2.1.1 Offset and gain characterization

As outlined above a feature that allows to automatically adjust the offset and the gain of each individual digitizing channel, according to the voltage levels of the digitized signal, has been implemented. To this aim it was necessary a characterization of the boards that are currently available in the system. Each board allows gain and offset to be set by the insertion of digital codes; the relationship between the gain code and the input dynamic range as well as between the offset code and the resulting input offset voltage has been inferred.

Firstly the characterization of the input dynamic range has been addressed. Each individual channel of each module has been fed with a sinusoidal waveform of known amplitude ($V_{IN,pp}$) that has been acquired with different values of the gain code. The recorded waveforms have been post-processed, obtaining the ADC output amplitude, expressed in LSB ($\Delta LSB_{out}$), and the gain of the channel as a function of the gain code, according to the simple formula:

$$Gain_{CH} = \frac{\Delta LSB_{out}}{V_{in,pp}} \tag{3.1}$$

The gain is outlined in Figure 3.8 as a function of the gain code and for the 8 individual channels of the DAQ system (the two modules have been

stated as *module 1* and *module 2*). The trend is clearly linear (i.e. the gain of the channel is proportional to the gain code of the variable gain amplifier), from the graph two straight lines of different slope are visible, related to a double gain feature of the VGAs, a low gain mode (gain codes from 0 to 127) and a high gain mode (gain codes from 128 to 255). In addition, within

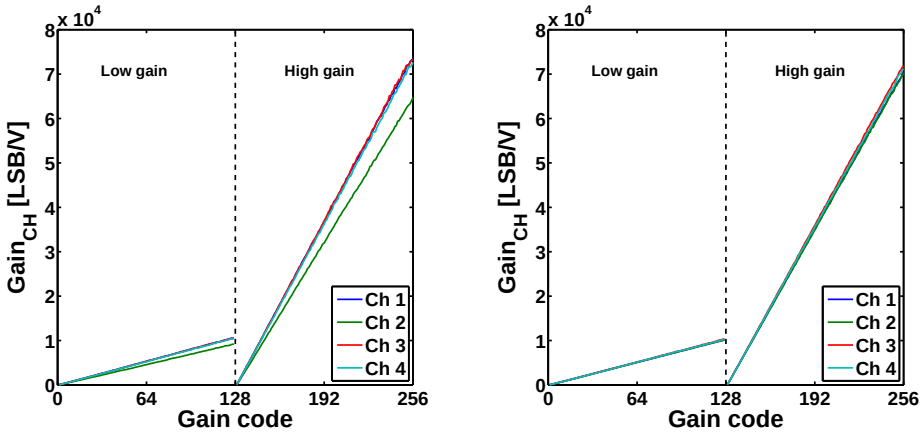


(a) module 1 (b) module 2

**Figure 3.8:** *Channel gain, expressed in LSB/V, as a function of the gain code.*

the same module, the individual channels show a uniform gain, except for the channel 2 of the *module 1* that shows a slightly different gain from the other.

Then the relation between the input dynamic range and the gain code has been deduced. The input dynamic range (DR) corresponds to an ADC output amplitude equal to $\Delta LSB_{out} = 4096$ (12 bit ADC) and, being known the gain of the channel, it can be inferred according to the following formula:

$$DR = \frac{4096}{Gain_{CH}} \tag{3.2}$$

Figure 3.9 shows the resulting dynamic range as a function of the gain code. It must be stated that, regardless of the gain code, the dynamic range is anyway limited by the SIS3350 boards circuitry to $\sim$ 6 V.

Fitting the hyperbolic trend (Figure 3.10) according to a $k_G$/(gain code) law, the $k_G$ coefficient, that is expressed in [V·(gain code)] and relates the input dynamic range to a specific gain code is obtained. The results are summarized in Figure 3.11, which shows the $k_G$ coefficient obtained for the 8 individual channels and for both the low and high gain modes. This

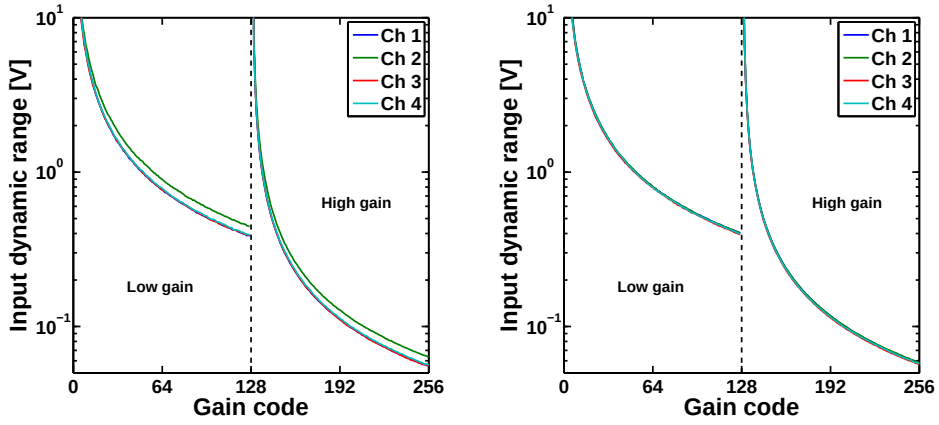


(a) module 1 (b) module 2

**Figure 3.9:** *Input dynamic range as a function of the gain code.*

parameter is suitable for the conversion from the signal voltage levels to the gain code value, therefore has been incorporated in the software code.

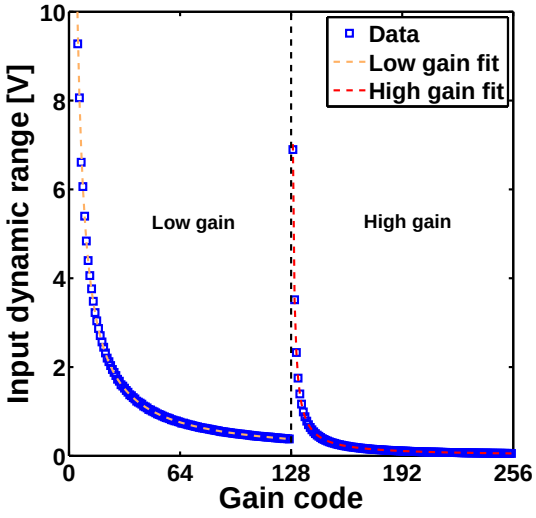


**Figure 3.10:** *Least square fit, according to the $k_G$/(gain code) law.*

The next step has been the assessment of the input offset voltage as a function of the offset code. In this case each individual channel has been digitized without feeding any input signal, varying the offset code (values from 0 to 65000, step 1000) and for different values of the gain code (values

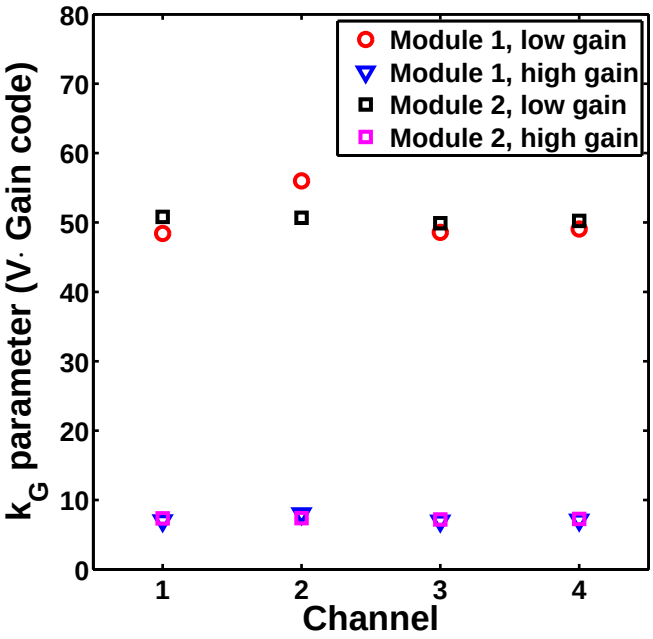


**Figure 3.11:** *The extracted parameter $k_G$, that relates the gain code to the input dynamic range of the individual channels.*

from 0 to 255, step 5). For each channel has been obtained a plot like the one showed in Figure 3.12. The average ADC output is the input baseline mean value amplified by the preamplifier and the VGA (refer to Figure 3.2, p. 61, for the scheme of the individual channel electronics), it is showed as a function of the gain code and each curve corresponds to a single offset code value. The baseline shows a saturation effect (to 0 or 4095) by increasing the gain code. The offset DAC provides bipolar offset; ideally, in a 16-bit bipolar DAC, the 0 V output code is $2^{16}/2$ (32768), for lower offset codes an ever negative input offset (and consequently a negative saturation) is achieved, otherwise for greater offset codes. The saturation is as fast as the offset absolute value is high, this corresponds to offset code values close to 0 or to $2^{16}-1$. Figure 3.12 shows also a slight asymmetry, a nearly constant baseline (a constant baseline corresponds to 0 V input offset voltage) is observable for the offset code 30000 (instead of an expected value between 32000-33000).

The average output baseline value, expressed in LSB units, has been converted into the input offset voltage by means of the information, gathered with the previous characterization, about the gain of the individual

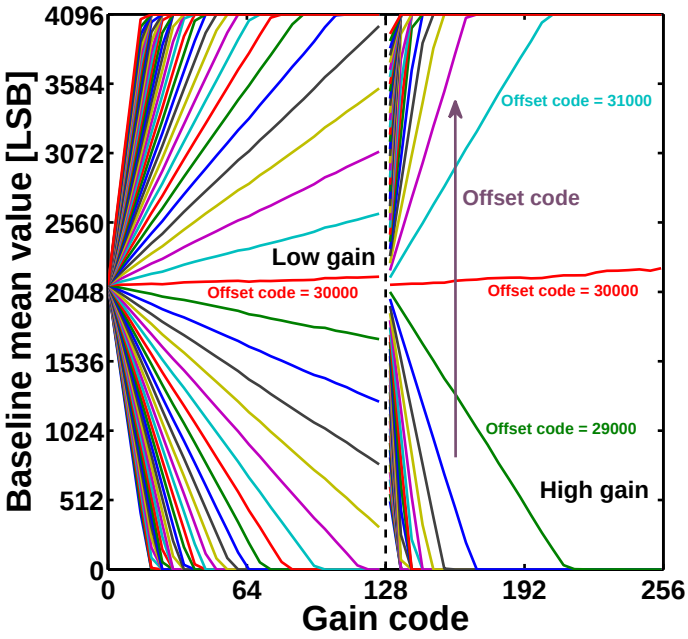


**Figure 3.12:** *Average ADC output sampled baseline, expressed in LSB, as a function of the gain code, plotted for different offset codes.*

channel as a function of the gain code. Figure 3.13 shows the same data of Figure 3.12 but converted into voltage and plotted as a function of the offset code, each curve corresponds to a gain code value. Different curves can be observed, that saturate at different voltage values, according to the gain code used (obviously the grater the gain, the lower can be the input offset in order to avoid saturation). However all the curves are superimposed in the central linear zone where they are not saturated. This linear zone is the most interesting, because it shows the variation of the offset input voltage as a function of the offset code. The relation, in terms of the slope $m$ and the coefficient $q$, between the input offset voltage and the offset code is found by performing a linear fit with the data of all the curves but taking into account, for each curve, just the data in the linear region. The results are shown, for the 8 individual channel of the DAQ system, in Figure 3.14, which summarizes the slope and the constant term.

These parameters allow a direct conversion from offset code and input offset voltage and, like the $k_G$ described before, have been incorporated in the software code in order to implement the gain/offset guess feature.

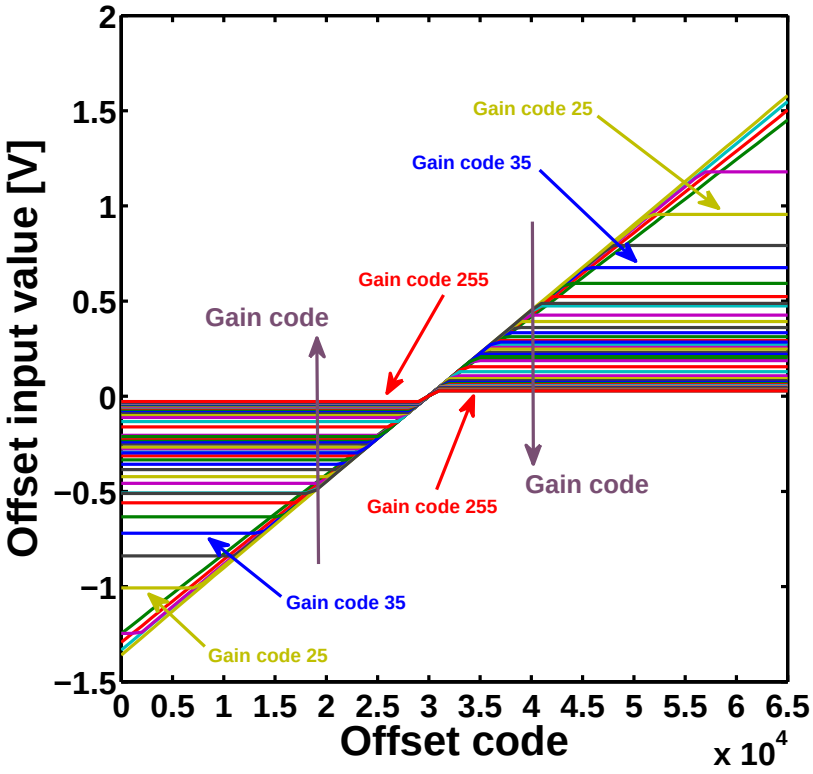


**Figure 3.13:** *Offset input voltage, as a function of the offset code, plotted for different gain codes.*

### 3.2.2 Management of the acquisition

The main issue to deal with, regarding the acquisition stage, has been the maintaining of the synchronism of the modules, in other words it is necessary to enable the on-board sampling logic (for all the boards of the DAQ system), to wait for an event (a trigger) that starts the acquisition, to understand when the acquisition is accomplished and to disable the sampling logic in order to prevent the acquisition of extra events. This has been easily achieved by exploiting some of the features that are offered by the SIS3350 boards.

It has been decided to transfer the data, from the internal memory of the boards to the remote PC, after the acquisition of each event. This has been preferred to a data transfer performed once the internal memory was full. In fact, the boards do not have any check about the used memory space,

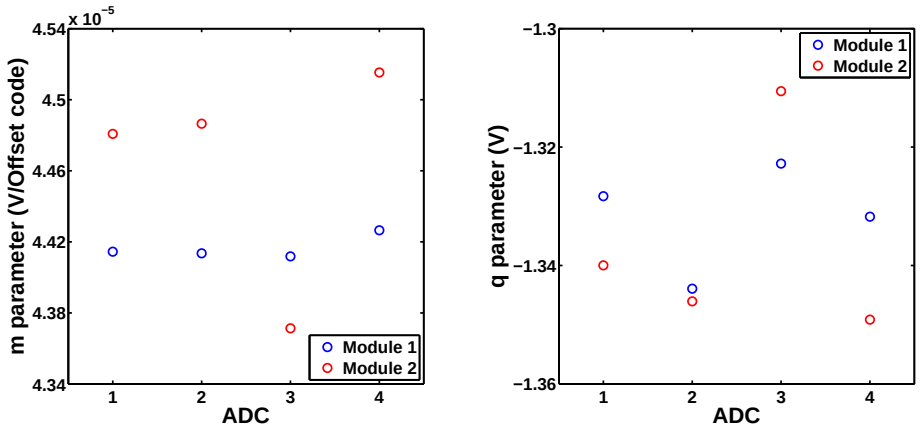


(a) m parameter

(b) q parameter

**Figure 3.14:** *The parameters m and q, extracted with a linear fit of the input offset voltage as a function of the DAC offset code, plotted for the different channels of the DAQ.*

when the memory is full the existing data are overwritten. Thus this choice has simplified the development of the software, by avoiding the continuous check of the memory usage status.

The boards provide an interrupt register that has been extremely helpful in order to effectively manage the acquisition. This register provides flags that highlight the occurrence of certain events, including the end of the acquisition. In addition the board internal logic provides a very useful feature for the synchronous modes of operation, that consists of the automatic disarming of the sampling logic at the end of the acquisition. This feature is extremely convenient, especially in the case of multi-board systems. In this way the acquisition of extra spurious events is automatically prevented, there is no need to implement any check via software.

So, before starting the acquisition, the software takes care to correctly set the interrupt register. Then it enables the on-board sampling logic of the modules, making the boards ready to acquire an event at the occurrence of a trigger condition. At the happening of the trigger condition the stream of digitized data from the ADC output is recorded to the boards internal memory. In the meanwhile the software continuously checks the modules until the completion of the acquisition is signaled by the interrupt registers of all the modules in the system.

When this condition occurs, in the case of synchronous modes of operation the on-board sampling logic is automatically disarmed, while in the case of asynchronous modes this does not happen and there is the possi-

bility that a further trigger event starts a subsequent extra acquisition. Is therefore the program that disarms the sampling logic in this latter case, but this is a simple operation because the asynchronous modes are available just with the single board hardware configuration.

An error check is performed by the software during the process just described, if an error occurs during the communication with the modules (while enabling the on-board sampling logic or during the polling of the interrupt register during the acquisition) the execution stops and an error message is printed. In addition a log file is written, which keeps track of the user-entered settings and of all the operations performed by the program (acquisition and storing of each event, an error that causes the software to be halted and so on).

After the successful completion of the acquisition the data are transferred to the host pc and written to disk, as described in the next section. The procedure acquisition-data transfer-data recording is repeated until a stop condition is verified, which may be the maximum number of events to be acquired, that is set by the user, or an external interrupt provided by the user.

The management of the acquisition is equipped with a graphic live preview, discussed in the following.

#### 3.2.2.1 Acquisition live preview

A feedback for the user is very useful, especially in order to identify and promptly correct any error, caused, for example, by a wrong set up of the system, that could spoil the data taking. So a second dedicated software has been associated with the main program. This second software is developed in C language and is suitable for the management of a graphical live preview of the acquisition. This software reads the data, that are recorded event by event on the remote disk, and periodically (with a rate of $\sim$ two per second) it shows the last sampled event. Figure 3.15 shows a screenshot of the preview.

A separate windows visualization for each waveform coming from the different channels that are enabled for the acquisition has been preferred. The reason resides in a better clarity, because the channels are divided by color, according to the specific SIS3350 module they derive from, making very easy the recognition of a particular channel.

This implementation, however, is more complicated than the implementation of its counterpart with a single window that shows all the waveforms acquired in a single event. In fact, the management of multiple windows is needed, the number of which depends on the number of channels used in

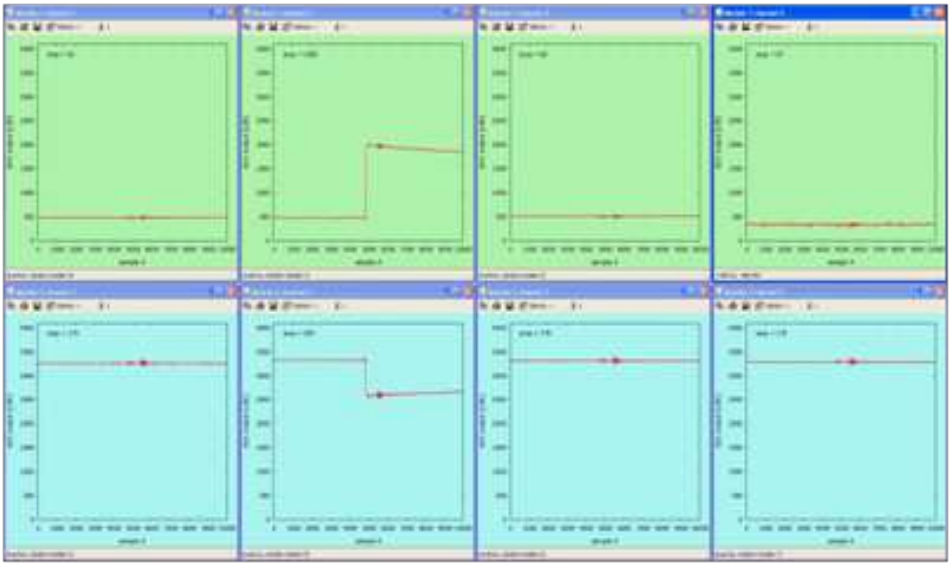

**Figure 3.15:** *A screenshot of the graphic live preview. 8 channels are visible, with 2 different colors, in order to distinguish the two SIS3350 modules of the DAQ system.*

the acquisition, and also on the number of modules installed in the system.

Therefore an algorithm that automatically fills the screen with an arbitrary number of windows has been developed, in order to follow the main software philosophy of adaptability to the hardware modifications.

### 3.2.3 Data recording

The data storing is another important issue for the development of the DAQ system. It has been settled to record the entire acquisition in a single file, in binary format. This choice was dictated by the need to maximize the disk writing speed, in order to increase the maximum acquisition rate, expressed in events acquired per second, of the acquisition system.

The binary format is undoubtedly more performing compared to the ASCII one, in addition a single file allows avoiding the continual open/close file operations that would occur in the case multiple files (acquisition of thousands of events is typical).

Being written in binary format, the file has been designed in order to be recognized and then reopened by a subsequent program, regardless of the number of events saved, the amount of sampled channels for each event, the number of samples of the single waveform and so on. The implementation of this feature has been simplified by the capabilities offered by the

SIS3350 boards internal logic, in particular the availability of a header, that is attached to each waveform and contains all the useful information.

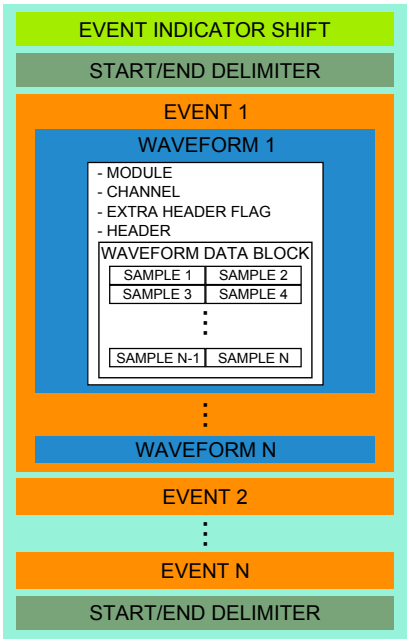


**Figure 3.16:** *Sketch of the record file format. The data are streamed divided into events, each event is composed of different waveforms.*

The SIS3350 board logic is based on 32-bit digital words, so also in the binary file the data have been organized with words of this size. In particular, the format of the file (Figure 3.16) is described below:

- event indicator shift: this is a fixed number added to the ordinal number of each event. This number is then necessary to distinguish the ordinal number of the event from other data, that could have otherwise the same value, such as the number of the module or the individual channel (see below);
- start/end delimiter: this number indicates the start and the end of the acquisition;
- the remaining file contains the acquisition, divided into events. Each event is organized as follows:
  - ordinal number of the event (added to the event indicator shift);
  - the acquired waveforms, each composed of:

    - module number: the SIS3350 boards are numbered in order to be univocally identified (3.2.1);
    - channel number: the number of the individual channel, from 1 to 4;
    - extra header flag: a flag that indicates the addition of an extra header, that is added to the normal header from the logic board under certain conditions;
    - header: a block composed of 4 or 8 32-bit words, depending on the extra header insertion. The header contains information on the size, expressed in samples, of the digitized waveform;
    - waveform: a block of 32-bit words containing the actual digitized data, each word contains two samples. The block size, variable according to the user settings, is always deducible from the information included in the header;

- start/end delimiter: to indicate the end of the data.

This file is created at the beginning of the acquisition; as each event is digitized is then streamed to the host PC and recorded to the file, that is closed once the acquisition is complete.

## 3.3 The DAQ under test

In the following will be presented some preliminary tests, that have been carried out up to now in the framework of the development of the DAQ system.

### 3.3.1 Preliminary on-beam test of the 8-channel system

A preliminary test of a the DAQ system has been carried out during a beam time at the DEFEL beam line at LABEC, Florence, Italy, in September 2012 with a two-fold goal. The first (and primary) goal of the beam time was the characterization of the response matrix and the calibration of Double-Sided Silicon Strip Detectors (DSSSDs) with mono-chromatic protons. A detailed description of the DSSSDs as well as the experimental results are presented in Chapter 4.

The second goal of the beam time was the test of the developed DAQ system. The new acquisition system worked in parallel with the primary 64-channel data acquisition system (100 MSample/s, 14 bit) of the DSSSD readout acting as a reference (see Figure 3.17 for the connection scheme).

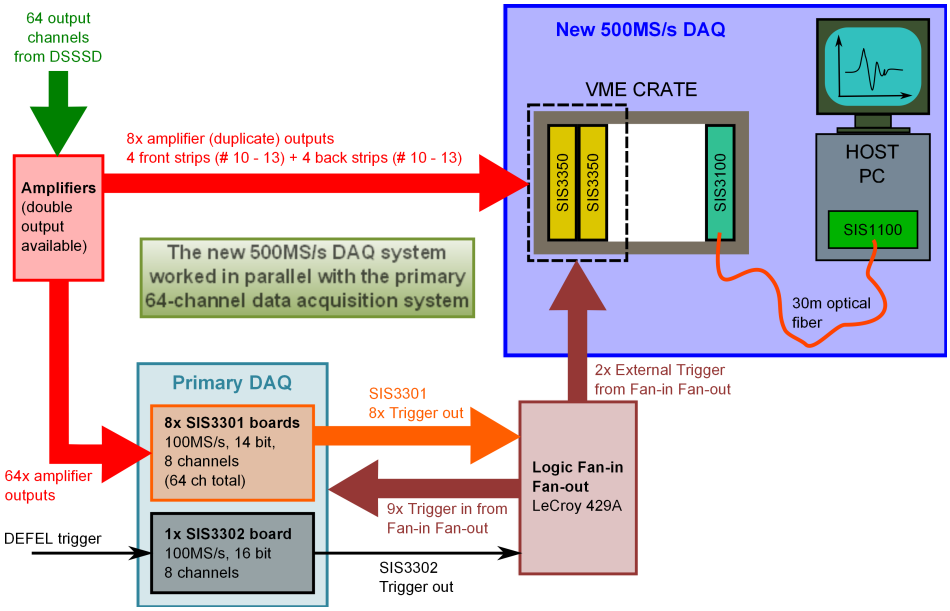


**Figure 3.17:** *Scheme of the connection of the new DAQ system under test in parallel to the primary system.*

The DSSSDs are divided into 32 horizontal and 32 vertical strips, each strip readout amplifier is provided with a double output, therefore 8 duplicates of the 64 strip readout channels have been fed to the 8 input channels of the DAQ system. The acquisition was triggered by the DEFEL line trigger signal, by means of a Fan in - Fan out unit, that is able to produce up to 16 output signals, used to trigger the modules of the primary data acquisition system and also the two modules of the DAQ under test. Each module has been triggered by feeding the trigger signal to the LEMO external trigger input, the data acquisition system has been configured following the multi-board 1 hardware configuration. The sampling frequency was set to the maximum value (500 MSamples/s) and the digitized waveform length to 1000 samples (i.e. duration of the acquisition 2 $\mu$s) while the DEFEL trigger frequency was 100 Hz.

Aim of this preliminary test was to verify the proper functioning of the system, developed so far, in a real environment, in order to qualify the effectiveness of the acquisition software and to evaluate possible improvements and the implementation of additional necessary features. When this test has been carried out the DAQ system was not fully developed yet, the graphical live preview feature has been implemented later and the data downloading was not optimized, being less efficient, in terms of speed, than in the latest

version.

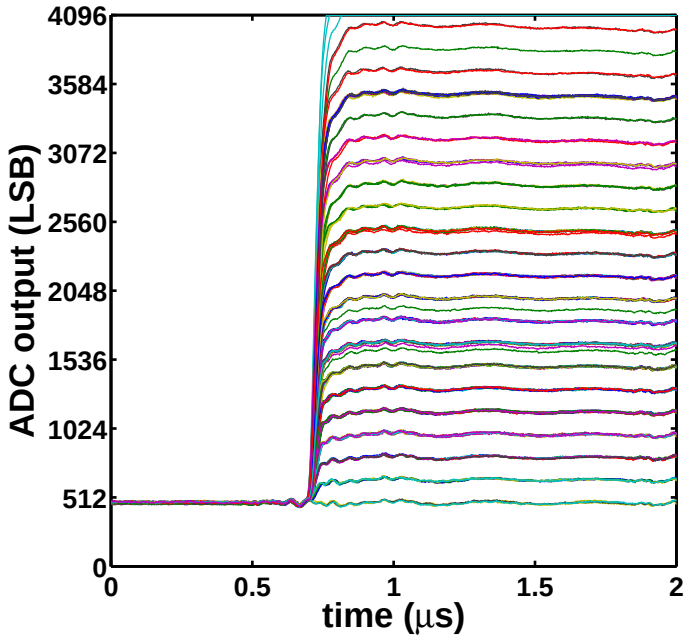


**Figure 3.18:** *Acquired waveforms, from an output channel of the DSSSD preamplifier, with the new DAQ system.*

This preliminary test produced very promising results, the user input settings implemented modality has showed a great practicality and the software management of the two SIS3350 modules during the acquisition was fully functional, allowing for the first time the digitization, by the new DAQ system, of data coming from a real device. Figure 3.18 shows a set of waveforms collected from a front strip in case of 3 MeV proton bunches. The different amplitudes correspond to the multiplicity of the proton bunch.

In spite of the general well-functioning of the system, the data transfer with the primary 64-channel reference system was much faster (this system can reach $\sim$30MByte/s data transfer speed) than with the new DAQ, because a not fully efficient data storing routine. This first negative result has pushed the efforts toward the implementation of a faster system; the achieved performance, in terms of the acquisition rate, is discussed in the following paragraph.

### 3.3.2 Acquisition rate

The acquisition rate of the DAQ system is defined as the events acquired per unit time. This parameter depends on many factors, some are related to the experiment, such as the event probability, the external trigger rate; other are related to the DAQ system, like the sampling frequency, the data stream transfer/storage rate. Aim of the characterization is to qualify under what conditions the acquisition rate is limited by external factors and when is limited instead by the DAQ system.

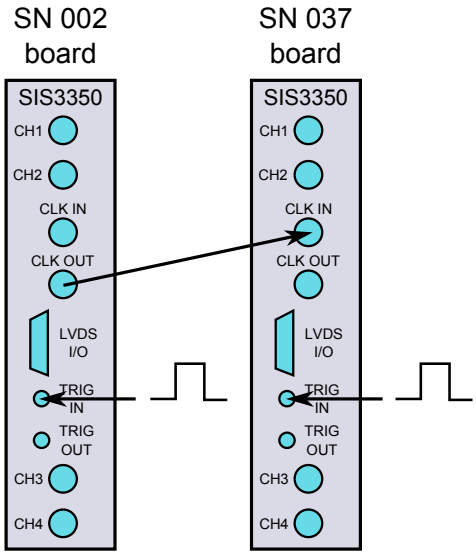


**Figure 3.19:** *Hardware configuration of the DAQ for the acquisition rate qualification.*

In order to carry out this test the system has been configured following the multi-board 1 hardware configuration (common external master trigger). Figure 3.19 shows in more detail the experimental setup, the 2 modules are distinguished by means of the serial number (SN002 board and SN037 board). The master trigger is externally fed via LEMO connector. The trigger signal is provided by a four channel digital delay/pulse generator (Model DG535, Stanford Research Systems, inc.). The SN002 board has been set as the *master clock board* and the clock has been distributed via BNC connector to the SN037 board with a 20 cm short cable.

The acquisition rate has been qualified at the maximum sampling frequency (500 MSamples/s), as a function of the external trigger frequency and of the number of samples of the digitized waveforms. All the 8 individual channels have been digitized, so a single event is composed by 8 waveforms. Different acquisitions have been performed varying the trigger

rate and the single event size, the results are presented in Figure 3.20 which shows the acquisition rate as a function of the number of samples of a single digitized waveform. The best condition is achieved when the acquisition

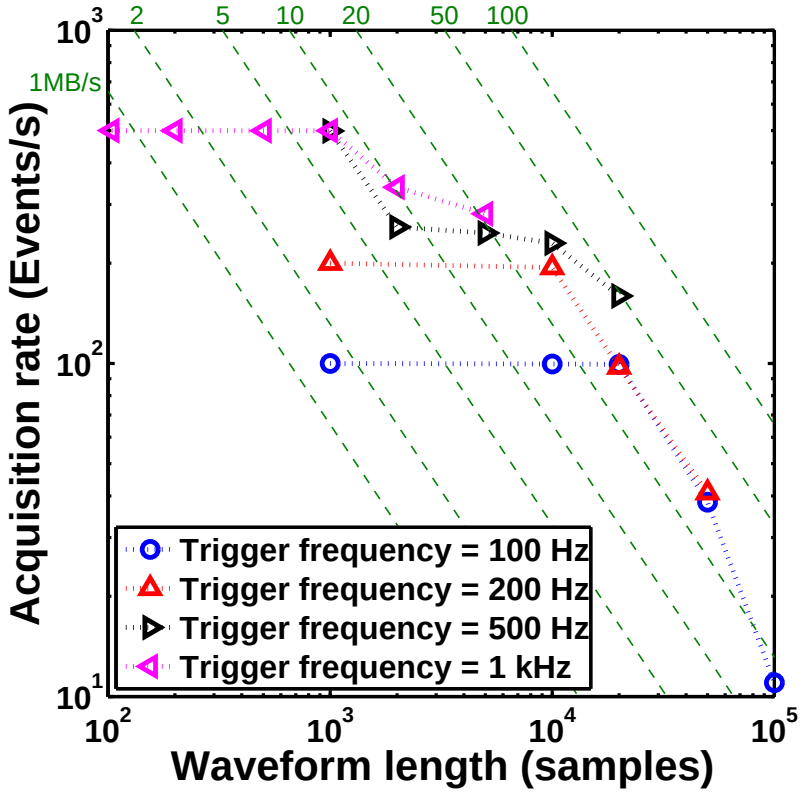


**Figure 3.20:** *Acquisition rate as a function of the sample length of the acquired waveforms. The green lines indicate the acquisition rate corresponding to a constant data transfer speed that ranges from 1 MB/s to 100 MB/s .*

rate is equal to the trigger frequency, in other words in this case the limiting factor is the external rate and not the DAQ system. From Figure 3.20 it can be stated that this condition occurs, for example, in case of external trigger frequency up to 500 Hz and a waveform length of 1000 samples, while is never obtained in case of 1 kHz external trigger frequency. By increasing the amount of digitized data in a single event the task becomes more demanding and the acquisition rate decreases as a consequence. In this case the limiting factor is the DAQ system, this lead to missed events because the DAQ system can not follow the event rate. Just a fraction of events will be collected, given by the ratio between the acquisition rate

and the event/trigger rate. The achieved performance is comparable with the 64-channel reference system used in the previous test, the data transfer speed is ∼30MByte/s, except one experimental point that shows 50MB/s, as visible from Figure 3.20.

The results are summarized in Table 3.1.

**Table 3.1:** *Maximum acquisition rates and corresponding maximum event size (expressed as the number of samples of each digitized waveform) achieved with a given external rate. The data refer to events collected with 8 channels at 500 MSamples/s sampling frequency.*

| Trigger frequency (Hz) | Acquisition rate (events/s) | waveform length (samples) |
|---|---|---|
| 100 | 100 | 20000 |
| 200 | 200 | 10000 |
| 500 | 500 | 1000 |
| 1000 | 500 | 1000 |

### 3.3.3 Qualification of the timestamp

Timestamp is the encoded information, recorded by the SIS3350 boards internal logic, used to identify the exact moment when a trigger event on an individual channel occurs. During the experiments the digitized waveforms of each event are marked with a timestamp, that provides time correlation between subsequent events and, within the same event, between different channels of the DAQ.

The SIS3350 boards are equipped with a 48-bit timestamp counter that counts at half of the sampling frequency. In other words, working at the maximum sampling frequency (500 MSample/s), the counter will reach the digital full scale in $\sim 10^6$ seconds, i.e. 13 days of data acquisition. The timestamp is provided to the user with the header of the digitized waveforms and is attached to the data, individually for each channel, when the logic starts to write the samples to the board internal memory.

Different tests have been performed with the aim to assess the timestamp stability within the individual channels. The basic idea of these tests was quite simple: feeding an external trigger and performing a synchronous acquisition the difference between the timestamp of different channels ought to be stable, in this case the time correlation resolution is limited just by the working frequency of the timestamp counter; in case the difference changes as the time run on, this is traduced in a worsening of the channels time correlation resolution. The full 8-channel system has been probed, the two modules are distinguished by means of the serial numbers as SN002 board

and SN037 board.

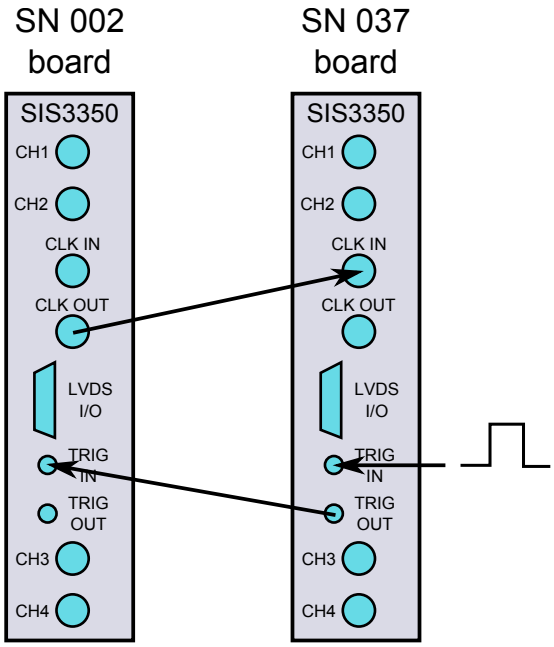


**Figure 3.21:** *Hardware configuration of the DAQ for the timestamp test n° 1*

Figure 3.21 shows the hardware configuration for the first test. The system has been configured following the multi-board 2 hardware configuration. The master trigger is externally fed via LEMO connector to the SN037 board, acting as *master trigger board*, and distributed via LEMO connector to the SN002 board. The trigger signal is provided by a four channel digital delay/pulse generator (Model DG535, Stanford Research Systems, inc.). The SN037 board is clocked, via BNC connector with a 20 cm short cable, by the SN002 board that acts as the *master clock board*.

The timestamp value has been obtained from the acquisition of 30000 events performed with a trigger frequency of 100 Hz (i.e. acquisition total time of 5 minutes). The difference between the timestamp of the individual channels has been analyzed. Regarding the SN002 board a perfect synchronization within the four channels has been obtained. Figure 3.22 shows, as example, the difference between the channels 1 and 2 of the SN002 board, expressed in counts as a function of the event number.

The channel 4 of the same board was however affected by a failure. Performing the timestamp difference between this channel and any of the other channels a result like the one showed in Figure 3.23 is obtained. Different spikes are visible, due to wrong bits written in the timestamp digital code.

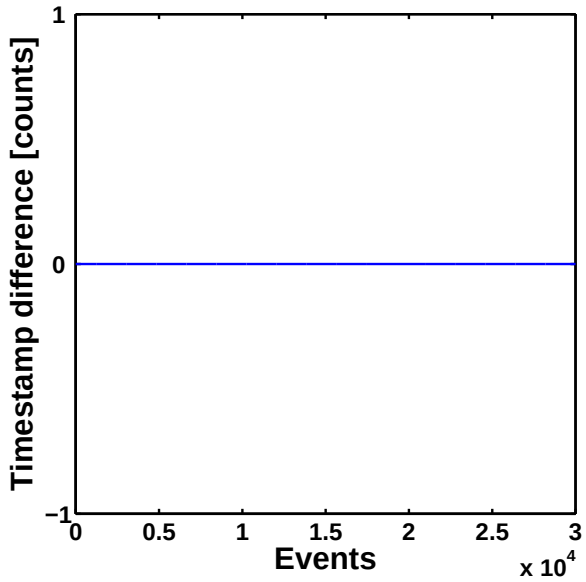


**Figure 3.22:** *Timestamp difference between the channels 1 and 2 of the SN002 board.*

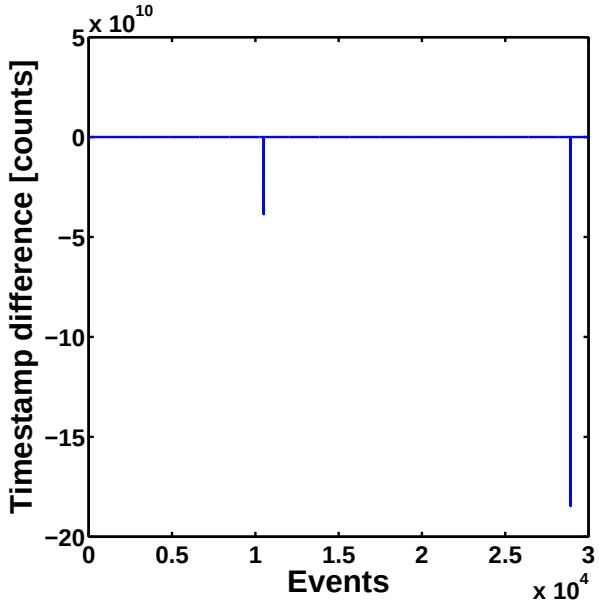


**Figure 3.23:** *Timestamp difference between the channels 1 and 4 of the SN002 board.*

Regarding the SN037 board the results are summarized in Figure 3.24,

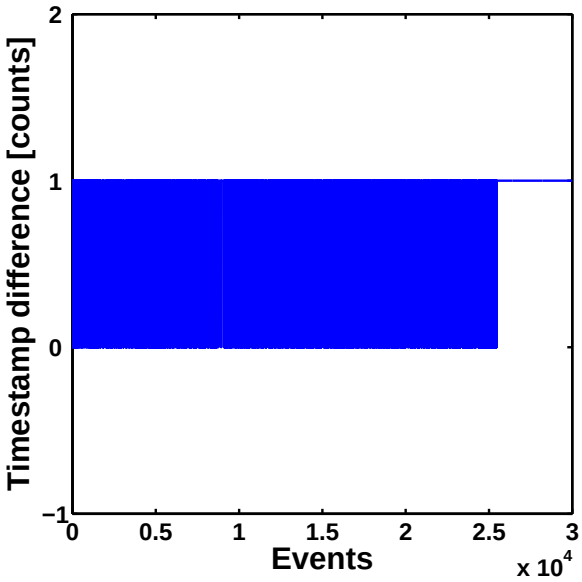


**Figure 3.24:** *Timestamp difference between the channels 1 and 4 of the SN037 board.*

in any case the timestamp difference is constant or at most oscillate with amplitude of 1 count, that is however in agreement with the technical specifications of the SIS3350 boards.

A second test has been carried just exchanging the clock distribution. Figure 3.25 shows the hardware configuration for this second test, that is the same of the previous test except that now is the SN002 board that is clocked, via BNC connector, by the SN037 board that acts as *master clock board*.

Again the timestamp value has been obtained from the acquisition of 30000 events performed with a trigger frequency of 100 Hz.

For the SN037 board the results are quite similar to the previous test, while the SN002 shows a clear drift of the timestamp within the four channels, visible in Figure 3.26. The drift is superimposed to an oscillation with amplitude of 1 count.

Channel 4 still shows the same malfunctioning of the timestamp discussed in the previous test. Figure 3.27 shows the timestamp difference between the channels 1 and 4 of the SN002 board in logarithmic scale, highlighting both the drift effect and the failure due to the wrong bits written.

The final result can be summarized as follows:

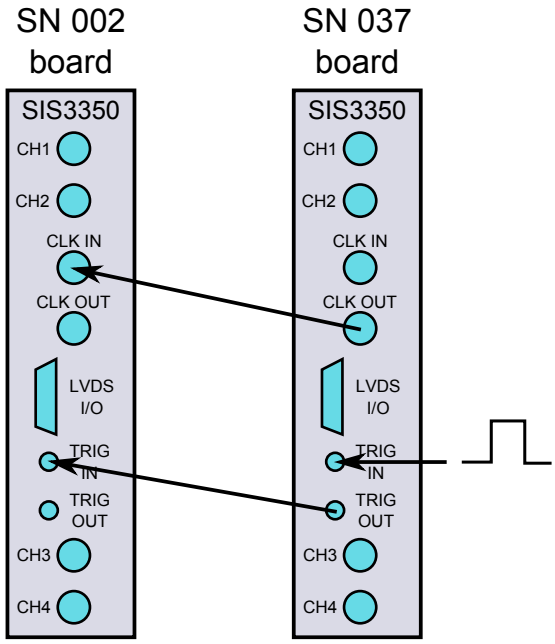


**Figure 3.25:** *Hardware configuration of the DAQ for the timestamp test n°2.*

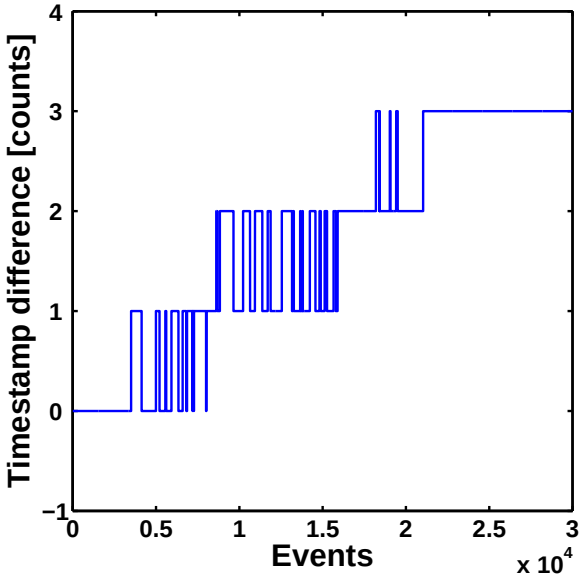


**Figure 3.26:** *Timestamp difference between the channels 1 and 3 of the SN002 board.*

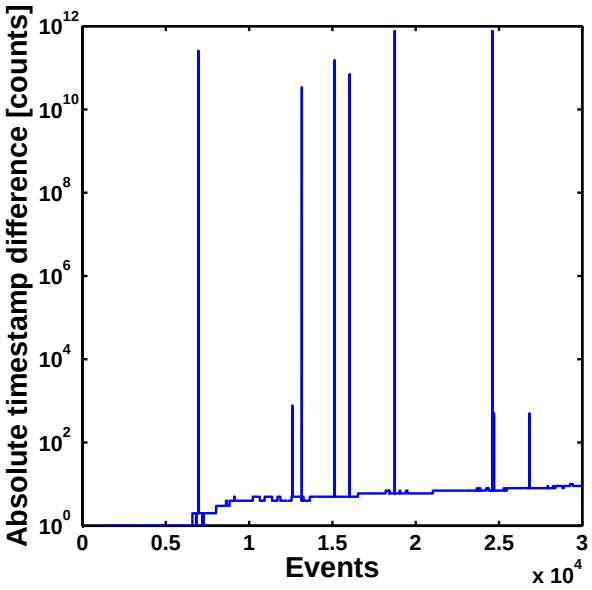


**Figure 3.27:** *Timestamp difference between the channels 1 and 4 of the SN002 board.*

- the SN037 board shows a good stability of the timestamp within the single channels in all conditions, at most the timestamp difference oscillate with amplitude of 1 count, however in agreement with the technical specifications;
- the SN002 board channel 4 timestamp is affected by a failure;
- if SN002 board is externally clocked the timestamp difference shows a clear drift within the four channels, otherwise the timestamp is stable (channel 4 failure still affect the board).

After these tests the SN002 has been sent to the manufacturer for inspection, and the channel 4 failure has been fixed. However the timestamp drift effect, showed in case of external clock, still affects the board. This can be solved using the SN002 board with the internal clock acting as *master clock board*.

CHAPTER 4

# Case studies

The radiation detectors characterization suite has been probed through qualification campaigns on two relevant case studies, discussed in the following. The first is the characterization, carried out with monochromatic protons, of the amplitude response over a wide range of the Double Sided Silicon Strip Detectors (DSSSDs) used as first and second detection stages of the telescopes that constitute the FARCOS array [45], [46] (Femtoscope ARray for COrrelations and Spectroscopy). The second is a detailed qualification, performed at low levels of charge generation with the laser test suite, of a first prototype of a DSSC-type pixel matrix with DePFET readout.

## 4.1 Qualification of a silicon strip detector with monochromatic protons at the DEFEL beam line

The characterization presented in this section is framed within the development of FARCOS, that is a novel detection system featuring high angular and energy resolution, able to reconstruct the particles momentum at high precision for different cases in multi-fragmentation nuclear physics experiments.

The telescopes that constitute the FARCOS array are composed of CsI(Tl)

crystals and Double-Sided Silicon Strip Detectors (DSSSD), the high spatial and energy resolution is provided by DSSSD of 300 $\mu$m and 1500 $\mu$m thickness, used as first and second detection stages respectively.

The mapping of the response matrix of the DSSSDs composing the FARCOS telescopes, with high spatial and time resolution, and the amplitude calibration have been performed by means of the mono-energetic proton beam at the DEFEL beam line of LABEC, Florence, Italy during a one-week beam time in September 2012. The results exposed in the following have been presented in a publication of which I am coauthor [47], and provide a meaningful example of the potentiality of the DEFEL proton beam line as a powerful characterization tool for radiation detectors.

### 4.1.1 Experimental setup

The double side silicon strip detector, provided by MICRON Semiconductor, on a standard design (BB7) with a minimum area PCB frame (4 mm of length), features an active area of 64 $\times$ 64 mm$^2$ [48]. Each DSSSD is divided into 32 horizontal and 32 vertical strips, with which it is possible to generate individual pixels of 2 mm $\times$ 2 mm. The inter-strip gap is 25 $\mu$m on the junction side (p+ implant strips, referred also as front side) and 40 $\mu$m on the ohmic side (n+ implant strips, referred also as back side), where p-stop implants are provided for strip insulation. A multi-guard ring structure is provided on the detector periphery on the junction side but it is left floating. Kapton cables (nearly 20 cm-long) are directly wire-bonded to each side of the detector.

The experimental setup is composed as follows:

- components in vacuum (DEFEL experimental chamber):
  - the detector under test and the charge preamplifiers are located inside the experimental chamber, housed on a mechanical frame;
  - a printed circuit board, responsible of distributing the needed filtered bias voltages to the preamplifiers and the detector together with the test signal coming from an external pulser, is held also on the mechanical frame;
- components out of vacuum:
  - anti-aliasing amplifiers (AAA), fed with the charge preamplifiers output;
  - the trigger system and the digitizer (64 channels ,100 MSample/s, 14 bit and 8 channels, 100 MSample/s, 16 bit);

– the host PC that supervises the acquisition process, located outside the radiation controlled area and connected to the data acquisition system through an optical fiber;
– the so-called air power board, that provides first order passive filtering of the detector and the preamplifier bias voltage and also a monitor of the absorbed current.

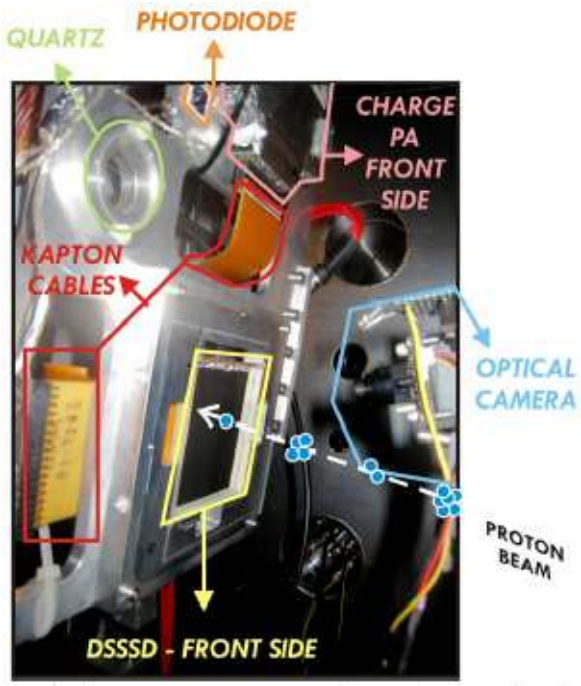


**Figure 4.1:** *Photo of the DSSSD housed on the mechanical frame located inside the DEFEL experimental chamber. Image taken from [47].*

Figure 4.1 shows the photograph of the DEFEL vacuum chamber. The detector under test is mounted on the X-Y stages and connected to the charge preamplifiers by means of the Kapton cables. The PCB detector frame is housed on a dedicated Aluminum holder fixed to a metallic mounting frame coupled to the 2D motion stages. The pn-diode detector, quartz glass and the optical camera are also visible (refer to 2.2, p. 30, for a description of the DEFEL experimental chamber).

The signals from the AAAs are digitized with a set of sampling ADC boards, hosted in a VME crate located in the controlled area. 8 SIS3301 boards for digitizing the 64 channels of the detector, and one SIS3302 board for sampling the external trigger signal from the beam-line deflector elec-

tronics have been used (refer to Figure 3.17, p. 81). The SIS3301 and the SIS3302 are 8-channels, 100 MSamples/s digitizers, with a dynamic range of 5 V and a resolution of 14 bits (SIS3301) and 16 bits (SIS3302), both produced by the SIS (Struck Innovative Systeme) GmbH. The VME crate is connected to the host PC located in the acquisition room with a VME-to-PCI bridge, composed of a SIS3100 VME board and a SIS1100 PCI board (SIS GmbH), connected via 30 m optical fiber.

The trigger signal is built by exploiting the auto-trigger function of the SADC boards. A trigger output signal is generated by each board based on software-defined conditions on the input signals. The trigger outputs from all boards are then OR-ed together and the result is fed back to the STOP input of each board. Since also the external trigger is sampled as an acquisition channel, triggering the acquisition system on the external trigger or on the threshold crossing event of any user-defined combination of channels is possible. The acquisition control software uploads the configuration parameters on the boards, starts the acquisition and downloads the acquired pulse shapes.

Since each board runs independently, there is no *a priori* guarantee that every trigger signal is processed by all boards, because different boards can be in different acquisition states at the same time. In order to avoid that multiple-event sequences become uncorrelated because of this, the boards operate in single event mode, after each trigger event the pulse shapes are downloaded from the boards and the acquisition restarted from the host PC. The system is able to operate up to a trigger frequency of about 100 Hz and a data bandwidth of about 30 MB/s using all the nine boards. Several custom developed pieces of software are then used to process the pulse shapes with various configurable algorithms in order to extract the relevant event parameters, visualize the data in a graphical way and further process the spectra.

The vacuum level in the experimental chamber was kept below $1 \times 10^{-4}$ mbar during all the measurements. The pulsed beam repetition rate was kept constant for all the measurements and equal to 100 Hz. The vertical slits opening that defines the beam spot size was 150 $\mu$m. The DSSSD was biased at 5 V over-depletion in all the measurements. Over-bias voltages up to 20 V have been successfully tested.

### 4.1.2 Amplitude calibration

Taking advantage of the proton bursts technique, it is possible to obtain an accurate energy calibration of each strip and of the corresponding preampli-

fier in a wide energy range from MeV up to even GeV energies, depending on the intensity of the incident beam. The energy spectrum under different conditions of proton beam energy has been collected. Since the charge collection time of the detector is much longer than the beam pulse duration, each bunch gives rise to a single event of amplitude proportional to the bunch multiplicity.

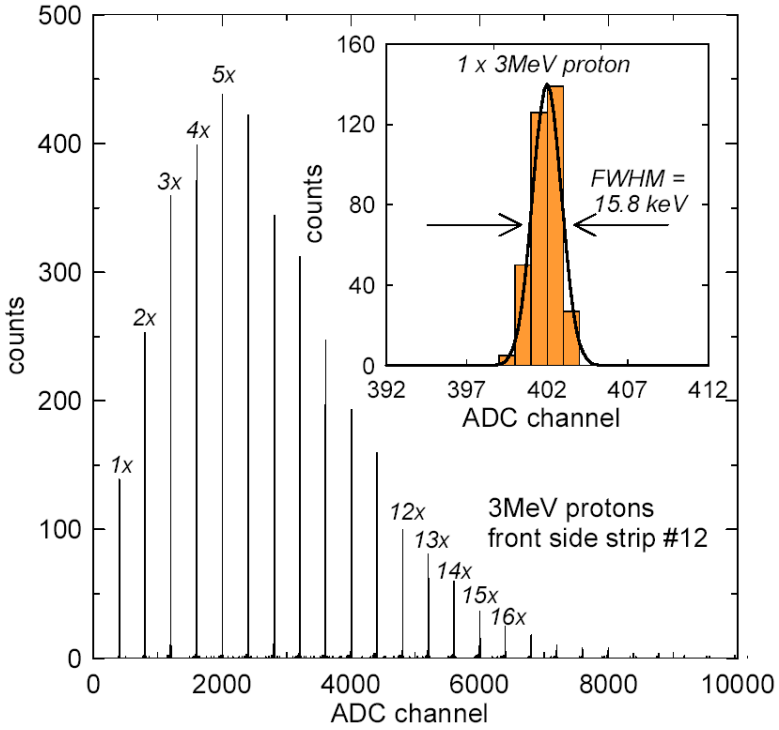


**Figure 4.2:** *Energy spectrum collected in the case of 3 MeV proton bunches injected on a single 300 μm-thick DSSSD strip from the front side. The visible peaks correspond to the proton bunch multiplicity. The inset shows a detail of the single proton peak and its Gaussian fit performed to extract the peak centroid.*

The digitized waveforms have been post-processed off-line with a digital triangular filter with 201 taps kernel length and the amplitude, expressed in ADC bins, has been calculated. Figure 4.2 shows the collected energy spectrum on one junction side strip of a 300 $\mu$m-thick DSSSD in case of interaction with a 3 MeV proton beam. Each peak corresponds to a different multiplicity of the proton bunch, up to 16$\times$, i.e. an energy range over 40 MeV has been spanned with 3 MeV protons. By least-square Gaussian fitting each peak of the spectrum and extracting its centroid it is possible to derive the ADC bins/energy correspondence and hence the calibrating

curve. The inset in Figure 4.2 shows the Gaussian fitting of the single 3 MeV proton peak. The FWHM of the Gaussian shape fitting peak is the energy resolution of the overall system.

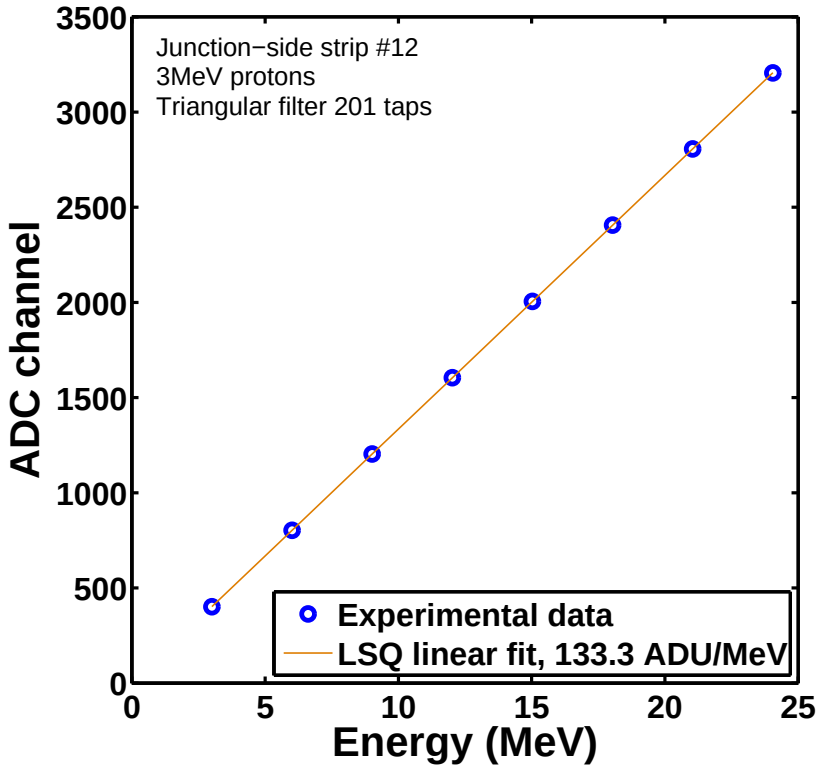


**Figure 4.3:** *Energy calibration of a front side strip, performed in an energy range up to 24 MeV with 3 MeV proton bunches.*

Figure 4.3 shows the result of the calibration of one strip of the junction side, performed with 3 MeV proton bunches.Proton bursts can also be used to measure the linearity of the overall system, including Si-detector, preamplifier, anti-aliasing amplifier and digitizer, or, more in general, the deviation from a desired calibration curve. Fig. Figure 4.4 shows the obtained integral-non-linearity for the strip calibrated in Figure 4.3.

This kind of qualification of the performance of the silicon detector is extremely useful since it allows obtaining a precise ad accurate independent calibration of each strip and of the corresponding preamplifier over a wide level of charge injection for the on-beam measurements.

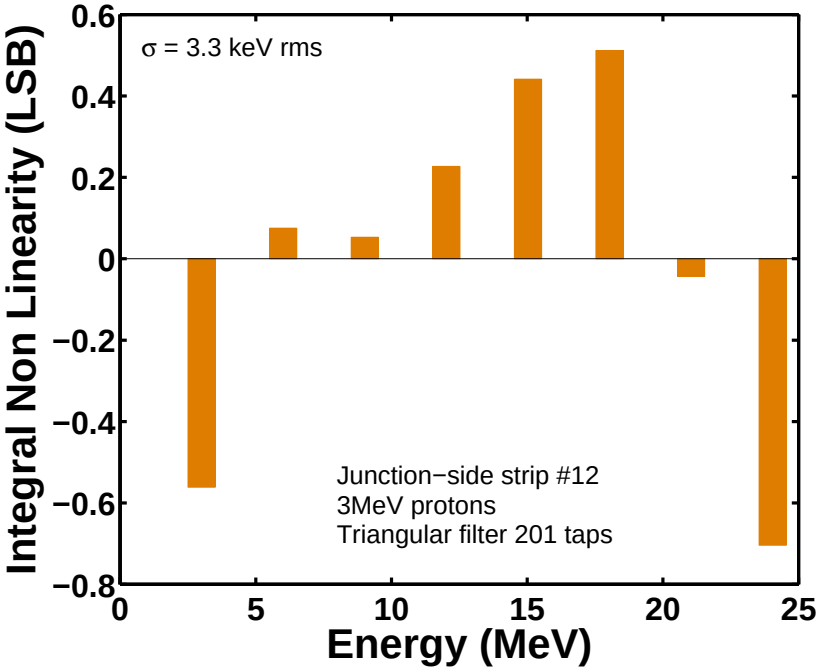


**Figure 4.4:** *Integral non-linearity of the energy calibration performed in Figure 4.3.*

### 4.1.3 2D position response matrix

Profiting of the high spatial resolution of the proton beam several scans have been performed across the strips to record the waveform response and to investigate their shape as a function of the position of interaction. Considering the single proton peak, it is possible to derive the strip profile and evaluate the amount of sharing events between neighbor strips.

Figure 4.5 (a) shows the scatter plot of the amplitude of the signals collected at three neighbor strips of the front (junction) side, called F11, F12, F13 (different colors for different strips) as a function of the beam position. The proton energy was set to 3 MeV and the injection performed in the front side; single proton bunches events have been selected off-line. As schematically shown in the inset, the scan has been performed across the three front strips in correspondence of the gap between two back (ohmic side) strips. The points have been artificially spread over a region as wide as the DEFEL final slit aperture (150 $\mu$m). The scatter plot shows a full charge collection

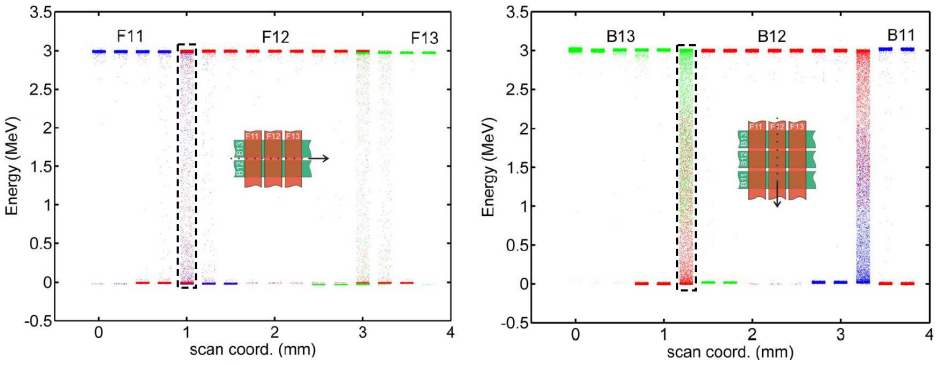


(a) Front side strips profile

(b) Back side strips profile

**Figure 4.5:** *Scatter plot of the amplitude of the collected signals with a scan (a) across three neighbor strips (different colors for different strips) of the junction side in correspondence of the gap between two ohmic strips and (b) across three neighbor strips (different colors for different strips) of the ohmic side in correspondence of the center of a strip of the junction side, as schematically shown in the inset. The single proton energy was set to 3 MeV and the injection performed on the front side.*

(amplitude corresponding to 3 MeV energy) all over the strip when the proton bunch is injected within the strip region. Charge sharing phenomena occur in case of inter-strip irradiation, highlighted in the black dashed rectangle between strips F11 and F12 and also evident between strips F12 and F13.

Figure 4.5 (b) shows an analogous scatter plot of the amplitude, obtained, in this case, with the signals collected at three neighbor strips of the back (ohmic) side, called B11, B12, B13 and in correspondence of the center of a strip of the junction side, as schematically shown in the inset. Like in the previous case the proton energy was set to 3 MeV and the injection performed in the front side. In this case the charge sharing is more relevant due to the wider size of the electron cloud reaching the ohmic side strips and to the wider inter-strip gap.

To gain a better insight in the sharing phenomena, that could greatly spoil the pulse shape analysis capability of the system, the amplitudes of all the signals collected at the two neighbor strips - with no off-line selection - when the beam was impinging at the coordinate highlighted by the dashed rectangle in Figure 4.5 have been scatter plotted.

The results are shown in Figure 4.6. The figures on the left show the amplitude correlation scatter plot between two adjacent front strips (Figure 4.6 (a)) and two adjacent back strips (Figure 4.6 (b)) in the case of inter-strip

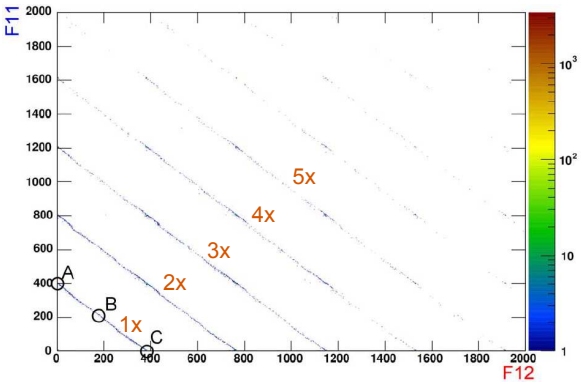


(a) Amplitudes correlation scatter plot between front strips F11 and F12.

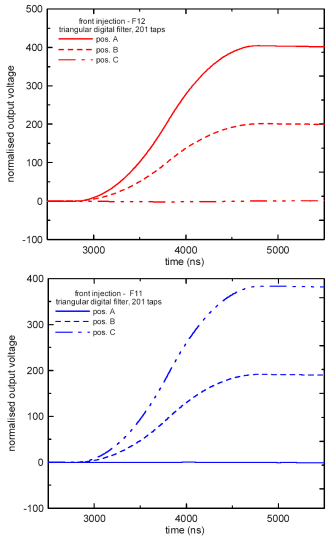


(b) Signals corresponding to the events highlighted as A (solid line), B (dashed) and C (dot-dashed).

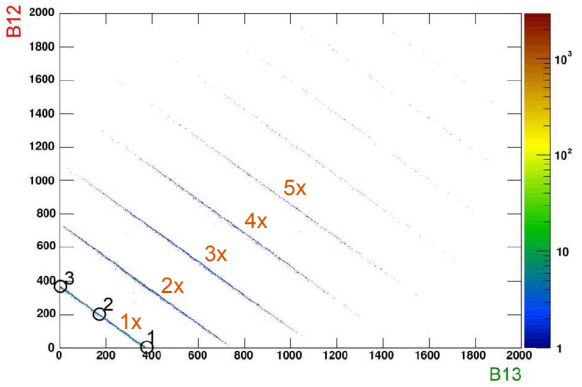


(c) Amplitudes correlation scatter plot between back strips B12 and B13.

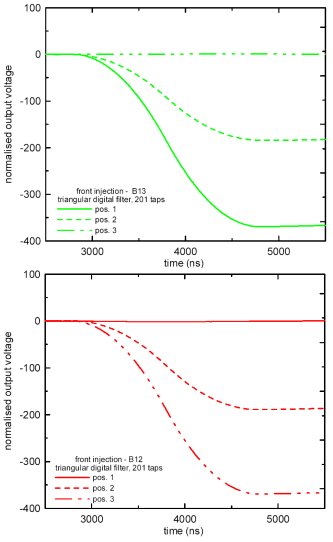


(d) Signals corresponding to the events highlighted as 1 (solid line), 2 (dashed) and 3 (dot-dashed).

**Figure 4.6:** *Amplitudes scatter plot of the signals collected at two neighbor (a) front and (c) back strips (beam impinging in the inter-strip region). The signals corresponding to the events highlighted as (A,B,C) and (1,2,3) are showed in (b) and (d) respectively.*

incidence. It is clearly visible a linear trend due to the charge sharing, for different proton bunch multiplicity. On the juntion (front) side the clusters related to the full collection on one of the strips and also all the possible pairs (i.e. one proton at each strip in the case of two-proton bunches, one proton at one strip and two protons at the other or the revers in the case of three-proton bunches and so on.) are clearly distinguishable. This is not the case for the back (ohmic) side strips owing to the aforementioned motivation regarding the wider electron cloud size.

The output waveforms corresponding to the events scatter plotted can be further analyzed in each region in order to find useful parameters for the pulse shape analysis. For low-energy particles, stopping in the first detection stage, the information about the energy (the signal amplitude) is not sufficient to identify the particle, so pulse shape analysis is very useful in this case because the different ionization profile of different particles. Because the sharing phenomena the pulse shape could be very different in case of particles impinging in the inter-strip region and in the center-strip region, so the response matrix of the detector have to be evaluated not only in terms of amplitude or time but more generally in terms of the full shape.

The possibility to acquire the full shape of the strip output signals with a DAQ system is essential for this purpose. As a trivial example in Figure 4.6 (b) and (d) the output waveforms of the events highlighted as (A, B, C) and (1, 2, 3) respectively are showed. It has to be noted that, due to the connectors arrangement on the flange of the vacuum chamber there is an inversion of the polarity of the preamplifier's output that has not been corrected for. In both cases three events, relative to the collection of the single 3 MeV proton, have been selected. The events highlighted as A (3) and C (1) refer to full collection on one of the two adjacent front (back) strips, coherently the output signal amplitudes are respectively maximum on one strip and zero on the other. The events highlighted as B (2) refer to charge sharing across the two adjacent front (back) strips, the output signals allow to quantify the effect of charge sharing on the pulse shape on both the probed strips. This trivial example shows the normal expected behavior, by changing the ion type and/or the energy the strips can behave in a different way [49], that can be qualified with the application of the method just described.

## 4.2 Characterization of a 4×4 DePFET matrix

DePFETs (Depleted P-Channel Field Effect Transistor) are very versatile devices [50]. They behave as amplifying elements in macropixels silicon drift detectors [51]; are proposed as charged particle detectors [52] and ma-

trices are suitable as X-ray imaging detectors with extremely high energy resolution [53]. In addition the signal charge confined in the potential well of the internal gate is not destroyed when read out and multiple readout of the signal charge is therefore possible, reaching sub-electron noise [54].

The DSSC consortium (DePFET Sensor with Signal Compression) funded by XFEL GmbH is developing a large format X-ray imager with hybrid DePFET readout based pixels for the European XFEL, already discussed in Chapter 1. In this design the sensitive cell is based on a DePFET featuring an internal gate able to reproduce a non-linear charge-current relationship with gain compression as signal level increases.

A DSSC DePFET matrix prototype (in standard technology PXD5), not featuring the gain compression mechanism, has been qualified over a wide range of charge injection levels. In the following will be exposed the results of the experimental characterization including the development of the dedicated experimental setup. This work has been already presented in a publication of which I am coauthor [55].

### 4.2.1 The DePFET principle

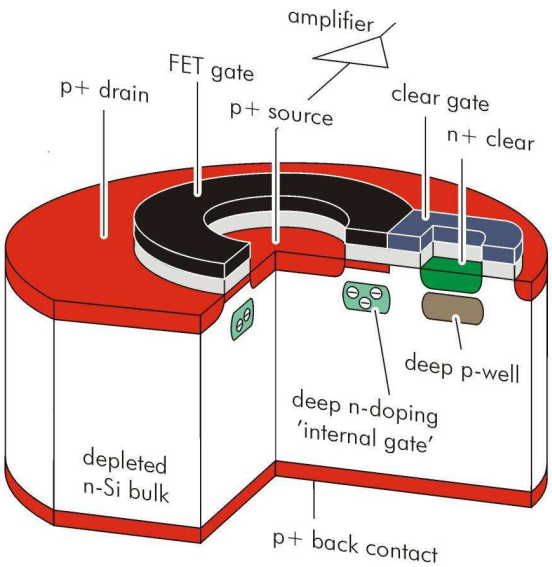


**Figure 4.7:** *Scheme of principle of a DePFET device.*

The DePFET is a unique structure since the detector is simultaneously the amplifier. Figure 4.7 illustrates the basic principle of the DePFET device. A field effect transistor is integrated on the top surface of a n-type

high-resistivity fully-depleted silicon bulk, in which a suitable tailoring of deep implants and of applied voltages creates a buried potential minimum for electrons near the surface of the bulk, confined to the area underneath the transistor channel. Radiation-generated hole pairs are separated by the electric field and the electrons drift towards this potential minimum. Hence the collected charge has a steering effect on the transistor current, where from the name of internal gate given to the potential minimum. In Figure 4.8 an electrical equivalent circuit of the DePFET is shown for better clarity.

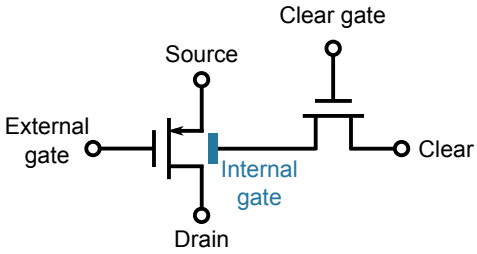


**Figure 4.8:** *DePFET equivalent circuit.*

After the measurement of the transistor current, the charge stored in the internal gate has to be removed by lowering the potential barrier that isolates the internal gate from the n+ clear contact. The clear region here consists of an additional n-MOSFET composed of the clear contact and a surrounding MOS structure, the so-called clear gate. Applying a positive voltage to both the clear and clear gate contacts remove the accumulated charge. The clear contact is separated from the detector bulk and the internal gate by an additional deep-p implantation, to prevent charge loss to the clear. After the clear phase the clear and clear gate signals can be lowered and the device is ready for a new irradiation.

Since no connections exist between the detector and the amplification section (that is built-in the device itself), the DePFET structure is intrinsically free of parasitic capacitance arising from the connection between the detector and the amplifier and in addition the gate capacitance can be reduced to very small values, with positive impact on both the noise [56] and the amplification level.

### 4.2.2 The matrix under test and the experimental setup

The matrix under test is the 4 $\times$ 4 DePFET pixel matrix showed in Figure 4.9. The single pixel has a circular geometry (75 $\mu$m size, Figure 4.10 shows an artistic view of the layout of a single pixel) and the probed pixels

are one border pixel and one central pixel, highlighted as pixel (2,1) and (2,3).

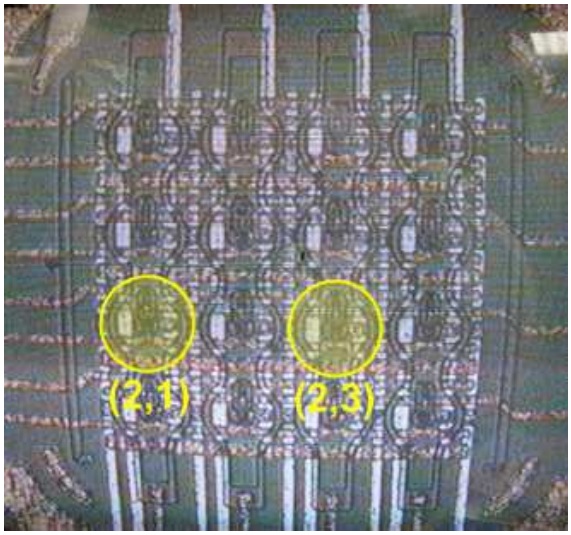


**Figure 4.9:** *The DSSC DePFET prototype matrix under test. The probed pixels are highlighted.*

The matrix electrical scheme is reported in Figure 4.11. The external gate (G), clear (C) and clear gate (R) signals are distributed row-wise providing for row addressing while signal readout (source, (S)) is connected column-wise providing for (4) column parallel readout. The drain contact (D) is common to all the 16 transistors of the matrix.

The device requires different bias voltages as well as some logic signals for the clear operation, and also requires appropriate readout electronics. A dedicated experimental setup has been developed made up of two different printed circuit boards, responsible of the accommodation of the DePFET pixel matrix and of its proper biasing.

The first, called POWER BOARD (Figure 4.12), is designed to generate and control all the DC voltage levels in a wide range required to study the operation of the detector and for the readout electronics. In particular are managed readout electronics power supply, high and low levels of the clear and clear gate signals, detector back contact depletion voltage, DePFET transistor biasing. All the bias voltages are first order passive filtered and test points allows to check chip currents while operating in vacuum. This board is housed in a metal box with BNC connectors for feeding external power supply.

The second, called MOTHER BOARD (Figure 4.13), accommodates

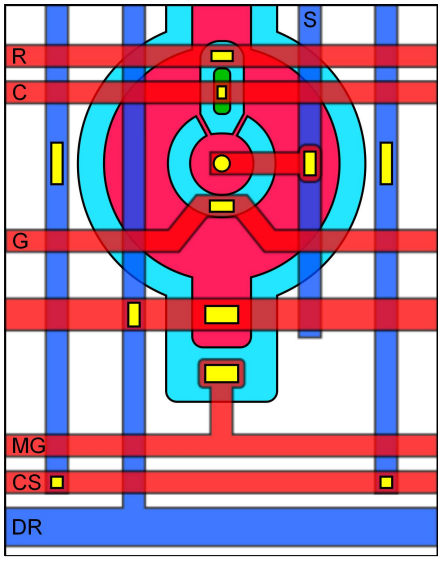


**Figure 4.10:** *Layout of the DSSC DePFET prototype single pixel of the 4x4 matrix. Source (S) and Drain (DR) are p+ implants and are represented in magenta, they correspond to the inner circle and to the outer ring respectively. The green area is the Clear (C) n+ implant. Two different metal lines are represented in blue and red, while the yellow areas are every kind of contact. The cyan area is polysilicon. Other contacts such as the DePFET Gate (G), Clear Gate (R), Mos Gate (MG) and Channel Separator (CS) are also visible.*

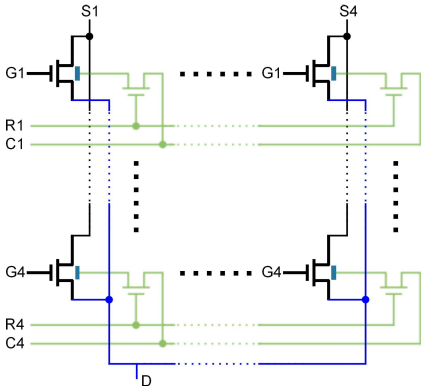


**Figure 4.11:** *Electrical scheme of the 4×4 pixel matrix under test.*

the ceramic carrier (Figure 4.14) holding the chip itself and is designed to handle the signals necessary to the clear operation, as well as to distribute all DC levels and signals from/to the chip. This board provide 4 slots for the insertion of different preamplifiers for the readout of the matrix columns.

**Figure 4.12:** *The POWER BOARD, responsible for the generation and control of all the DC voltage levels required for the operation of the detector and of the readout electronics.*

The MOTHER BOARD is housed on a mechanical frame and can be easily mounted on movement stages for fine pixel scans.

The clear operation requires the application of a fast pulse to both the clear and the clear gate contacts with a given and precise timing sequence. To this aim a fast high-voltage analog switch circuit has been implemented on the MOTHER BOARD and is driven by a four channel digital delay/pulse generator (Model DG535, Stanford Research Systems, inc.). The high and low levels (i.e. ON and OFF) of the clear and the clear gate pulses can be regulated on the power board, even during device operation in vacuum.

Due to the wide range of probed charge injection levels, the analog front-end has to show a very large dynamic range with very good linearity. Figure 4.15 and Figure 4.16 show the scheme of principle of the two developed readout electronic front-ends. The first one operates in voltage-mode with an nJFET buffer followed by a voltage amplifier and is suitable for low levels of charge injection. The second operates in current-readout mode and is based on an AC-coupled transimpedance amplifier, designed to handle

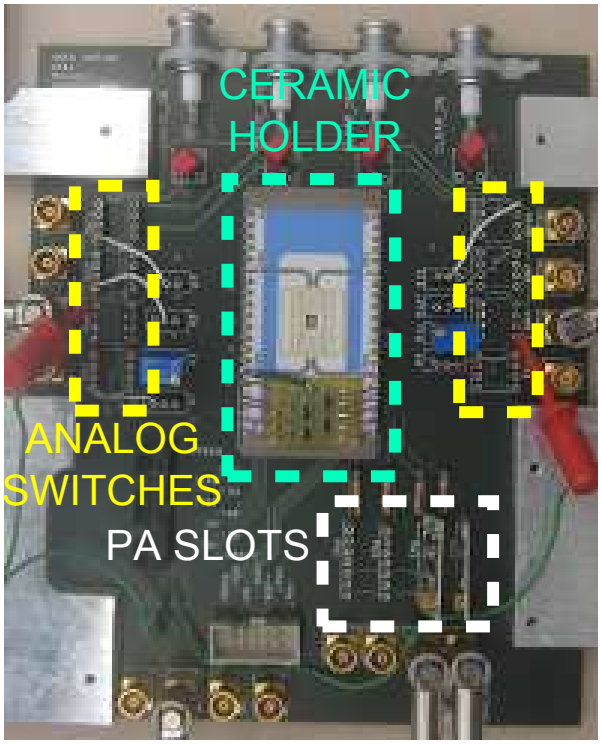


**Figure 4.13:** *The MOTHER BOARD that accommodates the chip and the readout electronics, distributes the DC levels and signals from/to the chip and handles the signals necessary to the clear operation.*

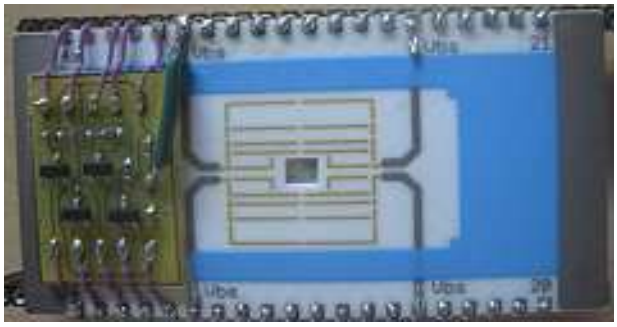

**Figure 4.14:** *Ceramic sample holder. The chip is visible in the central hole. Readout electronics is housed on the small PCB on the left.*

high levels of charge injection and able to keep the source of the DePFET at virtual ground for the signal.

For both circuits, the first stage of the front-end electronics has been developed on a thin separate printed circuit board, directly glued on the ce-

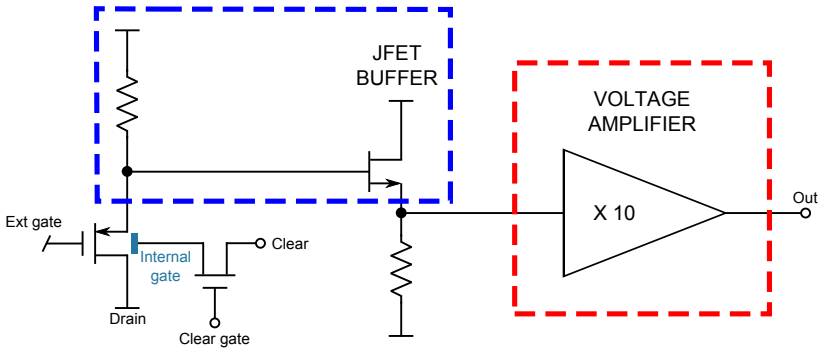


**Figure 4.15:** *Voltage readout scheme. The blue line highlights the first stage placed on the ceramic holder close to the chip, the red rectangle highlights the preamplifier inserted in the dedicated slot on the MOTHER BOARD.*

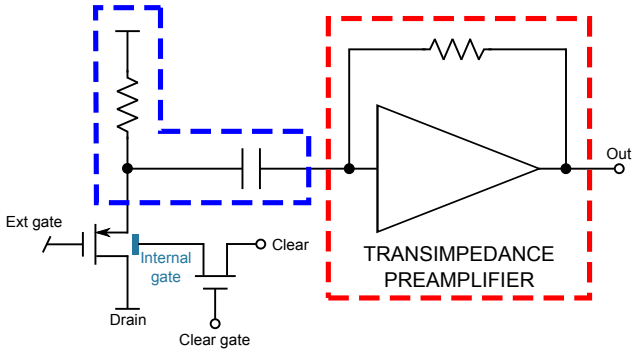


**Figure 4.16:** *Current readout scheme. The blue line highlights the first stage placed on the ceramic holder close to the chip, the red rectangle highlights the preamplifier inserted in the dedicated slot on the MOTHER BOARD.*

ramic holder as close as possible to the chip to minimize stray capacitance given by interconnections (see Figure 4.14).

### 4.2.3 Characterization with the laser test suite

A qualification of the DePFET pixels with the infrared laser source has been performed and will be here presented. The pixels have been probed as a function of different biasing conditions, different charge injection levels and modalities and different timing of the clear signal.

This experimental characterization, besides providing a deeper understanding in the properties of DePFET detectors, offers a detailed data-set useful to predict the detector response as a function of operating conditions and design properties and to be used for comparison with device simulation.

#### 4.2.3.1 2D Mapping of the pixel amplitude and time response

A detailed characterization of the detector amplitude response and charge collection time with a fine scan of the detector surface (exposing the uniform p+ implant of the back side to the laser beam at $\lambda$ = 905 nm) with 10 $\mu$ $\times$ 10 $\mu$m steps in the area pertaining to the two pixels highlighted in Figure 4.9 has been carried out.

For all the measurement, the device has been periodically cleared and, shortly (few $\mu$s) after each clear signal, an optical pulse has been applied releasing the corresponding injected charge. The laser intensity has been set in order to keep a constant charge injection level equal to $170\times10^3$ electrons, while the clear frequency was 10 kHz. The channels have been instrumented with the voltage mode readout and the output has been fed to a pseudo-Gaussian shaper (SILENA 7614) with 250 ns shaping time constant. The shaper provides a unipolar output and a bipolar output. At each scan position the pulse amplitude (of the unipolar output) and the time of arrival (zero crossing time of the bipolar output) have been measured. The detector has been biased with two different back voltages (150 V and 170 V). The measurement settings are summarized in Table 4.1.

**Table 4.1:** *DePFET Matrix 2D scan settings.*

| | |
|---|---|
| Irradiation side | p-side (back) |
| Laser wavelength | 904 nm |
| Scan step | 10 $\mu$m $\times$ 10 $\mu$m |
| Vback | 150, 170 V |
| Q | constant: 170 x $10^3$ el. |
| Readout | Voltage mode, no G=10 preamplifier |
| $\tau_{sh}$ | 250 ns |
| Clear frequency | 10 kHz |

Figure 4.17 shows the measured amplitude maps for the two pixels and the two probed back voltages. As it readily seen in the figure the pixel at the border shows an asymmetric response due to the end of the active area. The increase of the back voltage sharpens the pixel 2D profile.

Figure 4.18 depicts the same data in a contour plot, with the addition of the collection time information. It is clearly evident the asymmetry between amplitude and collection time within the same pixel. Amplitude is maximum at the pixel center and decreases evenly moving to the boundary of the pixel (this is not so true for the border pixel because the edge of the matrix), unlike the collection time that is much more influenced by the pixel layout.

In order to evaluate the asymmetry of the collection time (that is the

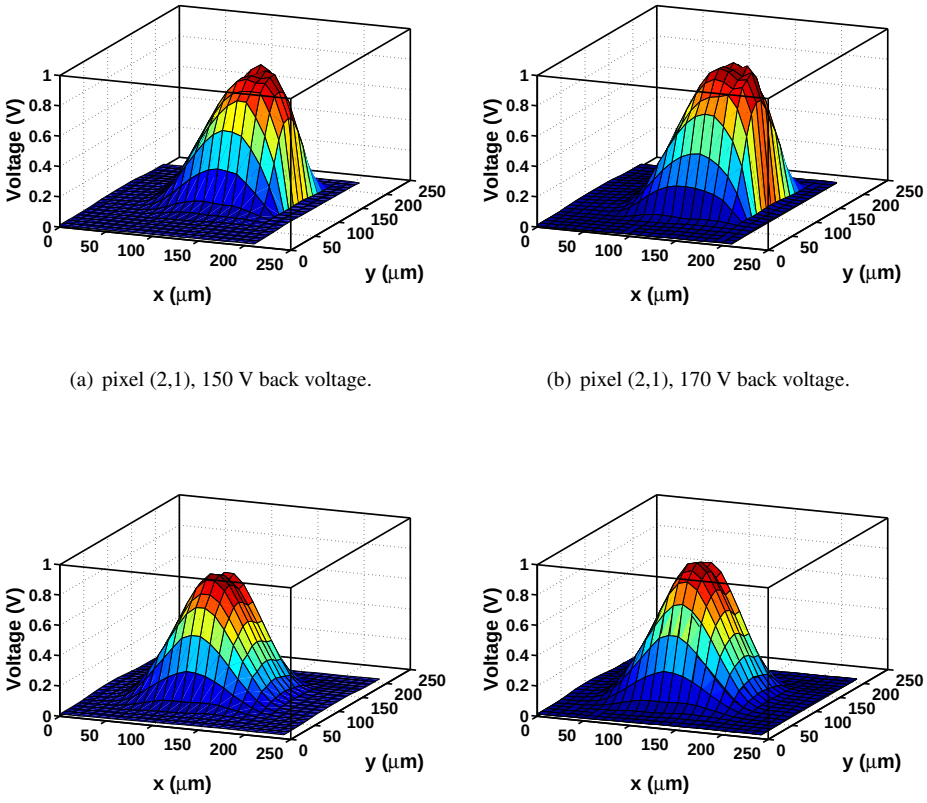


(a) pixel (2,1), 150 V back voltage.

(b) pixel (2,1), 170 V back voltage.

(c) pixel (2,3), 150 V back voltage.

(d) pixel (2,3), 170 V back voltage.

**Figure 4.17:** *2D profiles of the amplitude response of pixel (2,1) for a back voltage of (a) 150 V and (b) 170 V and pixel (2,3) for a back voltage of (c) 150 V and (d) 170 V.*

combination of a constant term, due to the readout electronics and the shaper delay, and a variable term, due to the pixel layout, that depends on the pixel injection coordinate) between the x and y directions a region of interest (ROI) has been defined around the coordinate that corresponds to the maximum amplitude of the response (the blue cross in Figure 4.18). Figure 4.19 shows the collection time of the two probed pixels for the back voltage of 170 V. The asymmetry is especially evident for the pixel (2,3) that is located in the center of the matrix. In this case the collection time is quite constant along the x direction (with a variation that is less than 10 ns) while shows a greater variation along the y direction. The pixel (2,1) be-

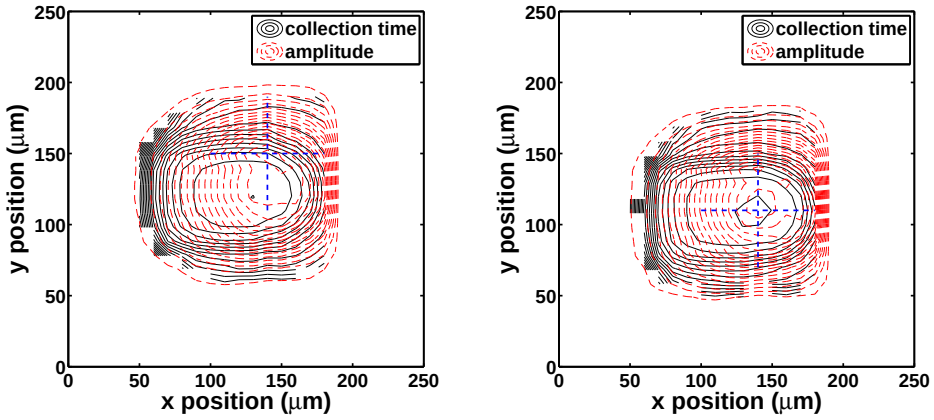


(a) pixel (2,1), 150 V back voltage.

(b) pixel (2,1), 170 V back voltage.

(c) pixel (2,3), 150 V back voltage.

(d) pixel (2,3), 170 V back voltage.

**Figure 4.18:** *Contour plots of the signal amplitude and collection time ($\Delta V$ = 50mV, $\Delta t$ = 10ns) of pixel (2,1) for a back voltage of (a) 150 V and (b) 170 V and pixel (2,3) for a back voltage of (c) 150 V and (d) 170 V. The blue cross is 80 μm wide along both the x and y directions, it stands for the pixel occupation area (75 μm size) around the maximum amplitude coordinate, that corresponds to the center of the cross.*

haves in a different way because its position at the matrix edge that affects the collection time along the x direction. In this case the pixel coordinate that corresponds to the maximum signal amplitude is located near the border and the collection time shows a great variation going toward the edge. The y direction is quite unaffected obviously because the two pixels are positioned at the same y coordinate.

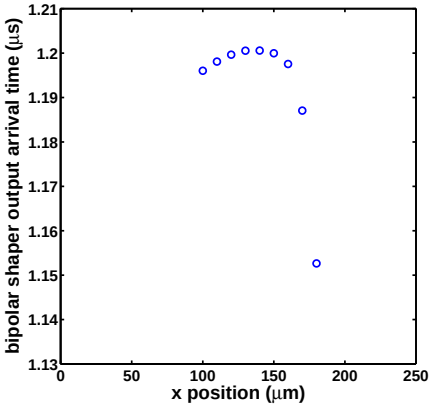


(a) pixel (2,1), 170 V back voltage, x position.

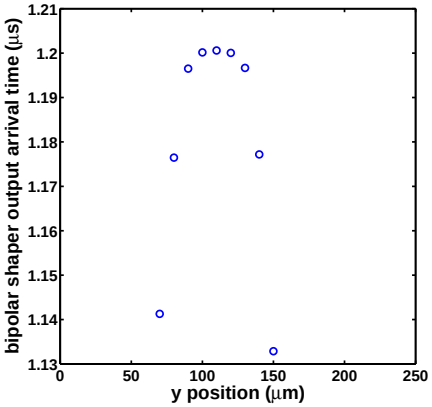


(b) pixel (2,1), 170 V back voltage, y position.

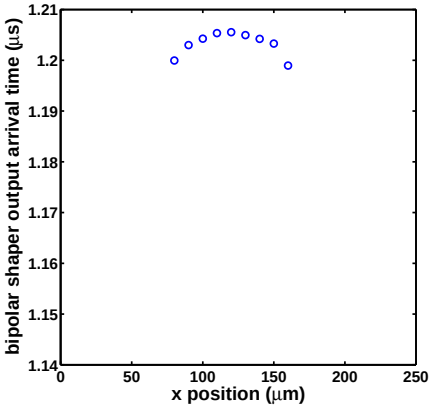


(c) pixel (2,3), 170 V back voltage, x position.

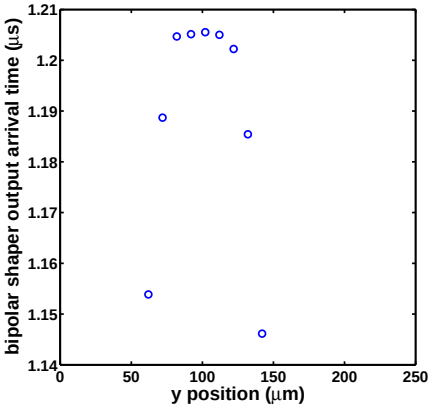


(d) pixel (2,3), 170 V back voltage, y position.

**Figure 4.19:** *Bipolar shaper output arrival time as a function of the position for the border pixel (2,1), along (a) the x direction and (b) the y direction and for the center pixel (2,3), along (c) the x direction and (d) the y direction. The experimental data correspond to the coordinates highlighted by the blue cross in Figure 4.18.*

For each contour plot the collection time has been extracted, obtaining different plots like the ones visible in Figure 4.19, and the collection time difference, defined as the difference between the maximum and the minimum collection times within the ROIs, has been calculated for both x and y directions. The results are summarized in Table 4.2

**Table 4.2:** *Collection time difference summary.*

| | $\Delta$t x (ns) | $\Delta$t y (ns) |
|---|---|---|
| pixel (2,1), 150V back voltage | 65.5 | 95.2 |
| pixel (2,1), 170V back voltage | 47.9 | 67.7 |
| pixel (2,3), 150V back voltage | 9 | 60.4 |
| pixel (2,3), 170V back voltage | 6.6 | 59.4 |

#### 4.2.3.2 1-D pixel profile as a function of the charge injection level

One dimensional scans at 10 $\mu$m step, varying the charge injection level (from $9.1\times10^3$ up to $1.9\times10^5$ electrons) and back voltages for the central channel (2,3), have been carried out to better study the pixel response. A back voltage from 110 V to 170 V has been applied, in order to highlight the different behavior of the pixel as a function of the depletion level. Measurement settings are reported in Table 4.3.

**Table 4.3:** *DePFET 1-D scan settings*

| | |
|---|---|
| Irradiation side | p-side (back) |
| Laser wavelength | 904 nm |
| Scan step | 10 $\mu$m |
| Back voltage | (110, 120, 130, 140, 150, 160, 170) V |
| Q | (9.16 21.43 51.23 93.29 191.5) $\times$ $10^3$ el. |
| Readout | Voltage mode, $G = 10$ preamplifier present |
| $\tau_{sh}$ | 250 ns |
| Clear frequency | 10 kHz |

Figure 4.20 shows the lateral scans of the pixel (2,3) comparing the results obtained with two (110 and 150 V) of the applied back voltages as a function of the charge injection level. Due to charge broadening during the motion towards the internal gate, the lateral profile of the pixel spatially enlarges at increasing levels of charge injection, at a given voltage applied to the back contact. At fixed level of charge injection, the increase of the back voltage sharpens the pixel profile and a plateau due to full charge collection in the central part of the pixel becomes visible.

Assuming a rectangular shape for the pixel weighting function and a Gaussian shape for the charge cloud profile, the measured 1D pixel profile can be least square fitted (dashed lines in Figure 4.20) with the convolution of the pixel weighting function and the charge cloud profile:

$$F(A;x_0;\sigma;L;x) = \frac{A}{2}\left[erf\left(\frac{x-x_0+L}{\sqrt{2}\sigma}\right) - erf\left(\frac{x-x_0-L}{\sqrt{2}\sigma}\right)\right] \tag{4.1}$$

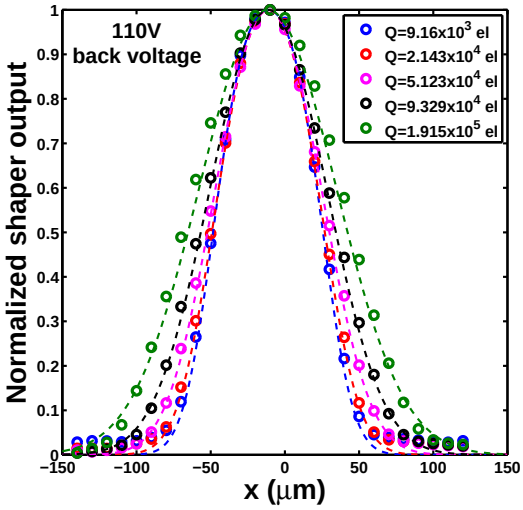


(a) 110 V back voltage.

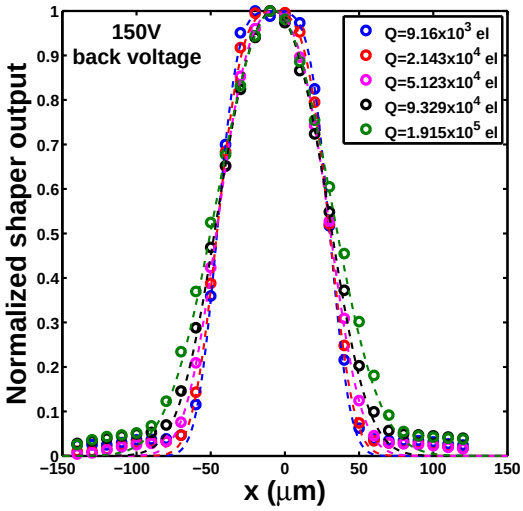


(b) 150 V back voltage.

**Figure 4.20:** *1D measured profile of the pixel (2,3) at (a) 110 V back voltage and (b) 150 V back voltage as a function of the charge injection level. Each curve is normalized to its maximum. The dashed lines show the corresponding least square fit according to equation* (4.1)

where A is the area, $x_0$ the centroid, $\sigma$ the standard deviation of the Gaussian function and L is half of the pixel size.

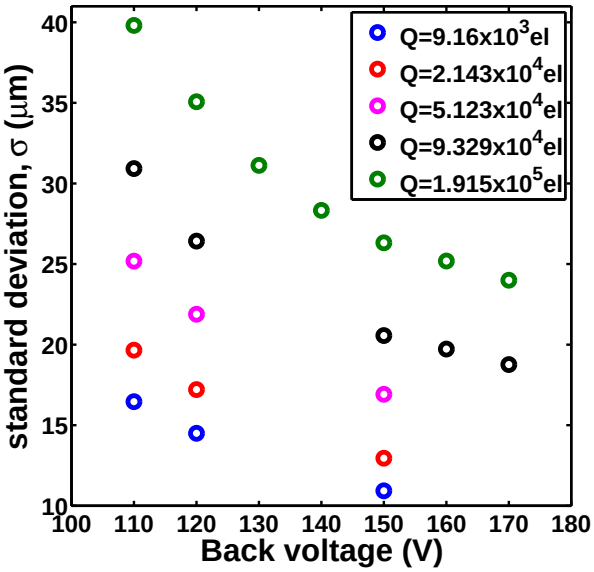


**Figure 4.21:** *Standard deviation of the charge cloud, obtained from the least square fitting of the experimental data.*

Figure 4.21 shows the standard deviation of the charge cloud, extracted with the fitting algorithm, as a function of the back voltage and for different charge injection levels.

The function 4.1 is the injected charge (corresponding to the parameter A) times a factor, included between 0 and 1, that is the collection fraction of the pixel. Considering the pixel center $x_0$ where the maximum value is obtained, the maximum charge collection fraction is given by:

$$Q_{collfrac} = erf\left(\frac{L}{\sqrt{2}\sigma}\right) \tag{4.2}$$

and can be easily calculated, being known L and $\sigma$ from the fit performed with the experimental data.

Figure 4.22 summarizes the charge collection fraction as a function of the back voltage and for different injected charges. At lower back voltages the collection fraction is less than 100% in all conditions, while increasing the back voltage the pixel perform better charge handling capability and full charge collection is observed.

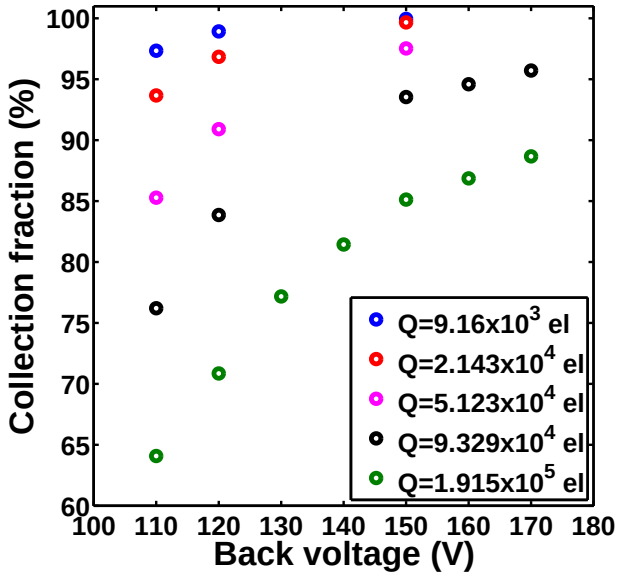


**Figure 4.22:** *Charge collection fraction of the pixel derived from the standard deviation of the charge cloud.*

#### 4.2.3.3 Amplitude response: single pulse injection vs burst mode

The impact on the amplitude response of two different modalities of increasing the charge injection level has been studied. The compared techniques, as schematically shown in Figure 4.23, are:

- varying the intensity of a fast single laser pulse able to provide the required level of charge injection (henceforth referred to as *single pulse*);
- full charge injection by means of a burst composed by a given number of laser pulses of equal intensity able to reproduce the desired injection level (henceforth referred to as *burst of pulses*).

The two techniques deliver the same total amount of charge level, however the dynamics is fully different.

The IR laser ($\lambda$ = 905 nm) has been focused in the maximum of the amplitude response on the detector back side, while the clear frequency (and hence the burst period) was 10 kHz. The matrix was instrumented with the voltage readout electronics without the G = 10 amplifier. The charge injection level was monitored with a separate reference photodiode. In burst mode different pulse repetition frequencies have been probed, with

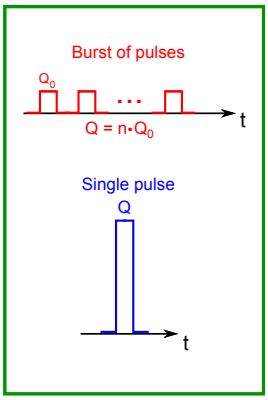


**Figure 4.23:** *Schematic drawing of the two probed injection modalities.*

a pulse duration of 10 ns. Also the effect of the back voltage (150 and 170 V) and the dependence on the charge injected with a single pulse in the *burst of pulses* modality have been assessed.

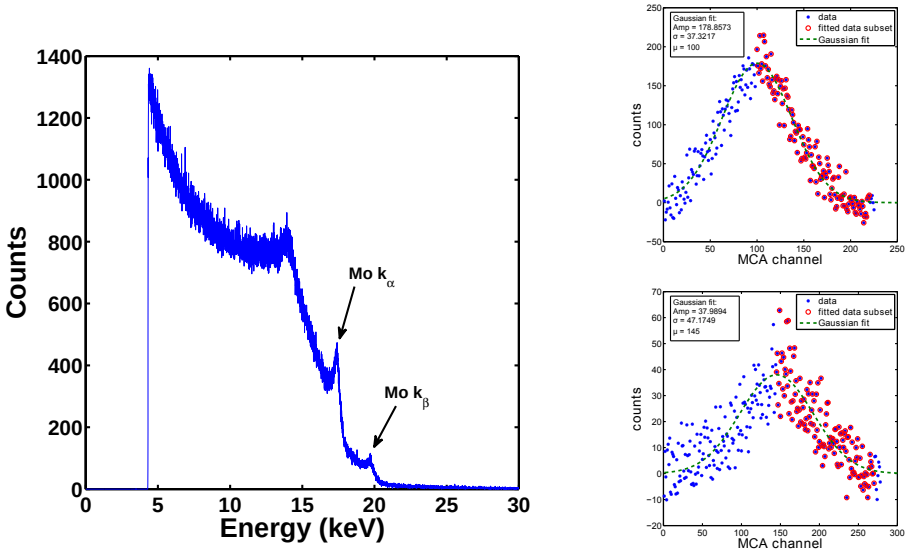


(a) Energy spectrum with X-ray photons (table-top Mo-anode source) injected on the back side of the DePFET pixel (back voltage 150 V).

(b) Gaussian fit of the $k_\alpha$ and $k_\beta$ peaks.

**Figure 4.24:** *(a) Energy spectrum obtained with a table-top Mo X-ray tube source irradiating the DePFET on the back side, the back voltage was set to 150 V. The Molybdenum $k_\alpha$ and $k_\beta$ peaks are highlighted. (b) Experimental data after background subtraction and Gaussian fit of the $k_\alpha$ (top) and $k_\beta$ (bottom) peaks.*

Before the presentation of the experimental results a discussion about the calibration is worthwhile. As exposed in Chapter 2 the laser intensity needs a calibration, obtained with a radioactive sources acting as energy absolute reference. To this aim the DePFET pixel has been irradiated, on the back side, with a X-ray table-top Mo-anode source tube, obtaining an energy spectrum like the one showed in Figure 4.24 (a). The pixel has been read out in voltage mode with the G = 10 amplifier, the output of the amplifier has been fed to a pseudo-Gaussian shaper SILENA 7614 (nominal gain set to 20, measured gain 19.08, shaping time set to 2 $\mu$s) and the output of this latter to a multichannel analyzer (Amptek MCA-8000A). The Molybdenum $k_\alpha$ and $k_\beta$ peaks, highlighted in the figure, have been least square fitted with a Gaussian function after background subtraction. For the calculation of the background the spectrum has been filtered with a running average (average window of 25 channels), for each peak a region of interest (ROI) has been selected and the background has been approximated as the linear function that interpolates the filtered spectrum counts at the ROI boundaries. The peaks obtained after the background subtraction are showed in Figure 4.24 (b), (the peak x-axis is shifted to 0 cause the software implementation of the Gaussian fit routine), the blue stars are the experimental data after background subtraction, a data subset has been selected for the least square fitting (red circles) and the green dashed line is the obtained Gaussian fit. The obtained fit parameters are shown in the insets, the calibration is obtained with a linear least square fit of three points: the origin and the centroids at the corresponding energy (data taken from [57]) of the $k_\alpha$ and $k_\beta$ peaks. The relation between the sum of the counts within the respective ROI of the $k_\alpha$ and $k_\beta$ peaks, considering the uncertainty introduced by the background subtraction and the few counts of the $k_\beta$ peak, is compatible with the relative intensity of the two peaks (data taken from [57]). The spectrum collection and calibration, here showed just in the 150 V case, has been carried out for both the 150 V and 170 V back voltages. The output voltages of the DePFET readout chain (JFET buffer + voltage amplifier + shaper) corresponding to the centroids, normalized by the voltage amplifier and the shaper gains in order to be comparable with the output voltage of the amplitude response (measured at the JFET buffer output), and the obtained calibration coefficients $\Delta V_{DePFET}/\Delta E$ are summarized in Table 4.4. The quantization error of the multichannel analyzer (8192 channels and 5 V power supply) reported to the JFET buffer output is equal to $Q_{err}$ = 5/8192/10/19.08 = 3.2 $\mu$V.

Figure 4.25 (a) shows the DePFET amplitude response, obtained with the *single pulse* modality in case of 150 V back voltage, as a function of

**Table 4.4:** *$k_\alpha$ and $k_\beta$ peaks voltage and calibration coefficient $\Delta V_{DePFET}/\Delta E$ at the JFET buffer output for the two probed back voltages.*

| Back voltage | $k_\alpha$ voltage | $k_\beta$ voltage | $\Delta V_{DePFET}/\Delta E$ |
|---|---|---|---|
| 150 V | 12.73 mV | 14.4 mV | $7.608 \cdot 10^{-7}$ V/eV |
| 170 V | 12.7 mV | 14.38 mV | $7.606 \cdot 10^{-7}$ V/eV |

the laser intensity. By means of a reference silicon photodiode the injected charge corresponding to the laser intensity has been monitored in the two injection modalities. For the calibration, as will become clear in the following, the linearity of the diode readout chain, composed of the diode, a charge preamplifier and a pseudo-Gaussian shaper (SILENA 7614) is a focal point. The non linearity of the readout chain (charge preamplifier + shaper) has been previously characterized and is <0.5%. Being the diode linear, any non linear effect that arise from the monitoring of the laser intensity is related to the laser. Figure 4.25 shows the diode output as a function of the laser intensity (b) and of the number of pulses with equal intensity (d) for two laser intensities. In the first injection modality (*single pulse*) the control knob of the laser, that provide a linear graduated scale, has been gradually rotated and the corresponding diode output amplitude measured as a function of the knob position (indicated as laser intensity, the probed values are the same of Figure 4.25 (a)). In spite of the linear scale of the control knob the curve in Figure 4.25 (b) is not linear, in other words the injected charge is not proportional to the control knob value, this means that the x-axis in Figure 4.25 (a) is not proportional to the injected charge.

Similar conclusions can be drawn from Figure 4.25 (d), the pulses are supposed to be equal, in other word in case of two pulses the charge injected (and the diode output amplitude) should be two times the charge injected with a single pulse, three times in case of three pulses and so on, resulting in a perfectly linear behaviour. The curves are clearly non linear, therefore the laser is not able to generate equal pulses in a single burst. The non linearity of the laser in both case can be corrected for by means of the linearity of the reference photodiode. Being the amplitude response of the diode linear with the injected charge the x-axis in Figure 4.25 (a) has been replaced with the corresponding diode output voltage in Figure 4.25 (b). Figure 4.25 (c) shows the DePFET amplitude response as a function of the diode output amplitude (that is proportional to the injected charge), the amplitude response shows a clear non linear behaviour (the shape of the amplitude response is discussed hereinafter), however the linear behaviour at low output voltages makes the calibration obtained with the Mo X-ray

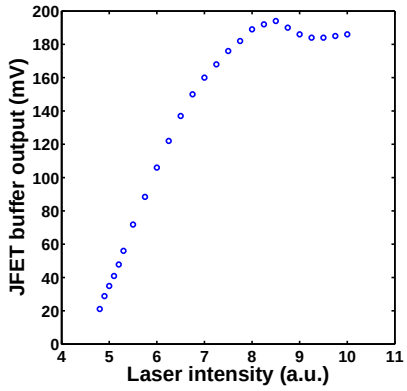


(a) DePFET amplitude response as a function of the laser intensity (150 V back voltage).

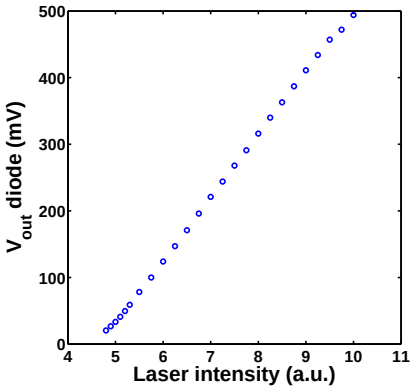


(b) Diode output amplitude a a function of the laser intensity.

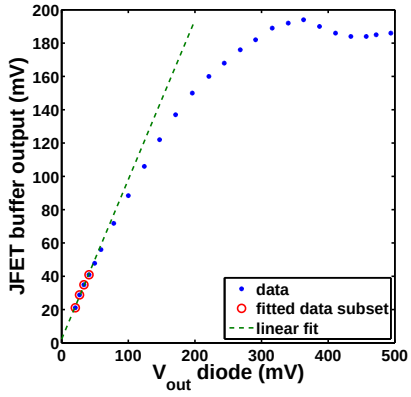


(c) DePFET amplitude response as a function of diode output voltage amplitude (proportional to the injected charge) and linear fit of the low voltage region.

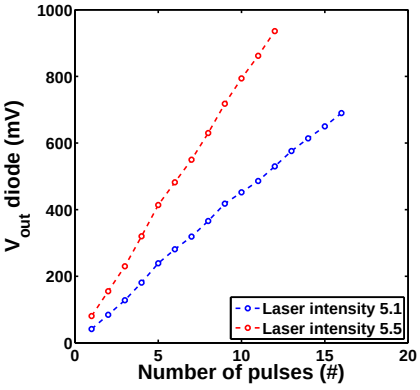


(d) Diode output amplitude as a function of the number of light pulses per burst, at a given laser intensity of the single pulse.

**Figure 4.25:** *Amplitude response of the DePFET pixel obtained with the* single pulse *injection modality (back voltage 150 V) (a). The laser intensity has been monitored, in case of* single pulse *(b) and* burst of pulses *(d) modalities, with a reference silicon photodiode. A non linear behaviour of the laser is evident in both cases. The laser intensity (x-axis of (a)) has been replaced with the corresponding diode voltage amplitude, that is proportional to the injected charge (c). A linear least square fit is performed in the linear region of the DePFET amplitude response, obtaining the conversion factor* $\Delta V_{DePFET}/\Delta V_{diode}$ *from the diode output voltage amplitude to the DePFET output voltage amplitude.*

tube is still valid in this region (compare the data reported in Table 4.4 with the JFET buffer output).

A linear least square fit in the linear region, as shown in Figure 4.25 (c), provide the conversion factor $\Delta V_{DePFET}/\Delta V_{diode}$ from the diode output voltage amplitude to the DePFET output voltage amplitude. This conversion factor, and the calibration factor $\Delta V_{DePFET}/\Delta E$ calculated before, are valid, for the DePFET, just in the linear region of the amplitude response. However the ratio between these two factors give the conversion between energy and diode output amplitude $\Delta V_{diode}/\Delta E$, that is ever valid thanks to the linearity of the diode. Table 4.5 summarize the $\Delta V_{DePFET}/\Delta V_{diode}$ and $\Delta V_{diode}/\Delta E$ for the two probed back voltages.

**Table 4.5:** *Conversion factor $\Delta V_{DePFET}/\Delta V_{diode}$ from diode output voltage amplitude to DePFET output voltage amplitude and from energy to diode amplitude $\Delta V_{diode}/\Delta E$.*

| Back voltage | $\Delta V_{DePFET}/\Delta V_{diode}$ | $\Delta V_{diode}/\Delta E$ |
|---|---|---|
| 150 V | 0.958 | $7.941 \cdot 10^{-7}$ V/eV |
| 170 V | 0.985 | $7.724 \cdot 10^{-7}$ V/eV |

The $\Delta V_{diode}/\Delta E$ of the diode should be obviously independent on the DePFET back voltage, however the two obtained values differ by the 2.8%, so the two $\Delta V_{diode}/\Delta E$ factors have been used ,respectively for the measurement carried out at 150 V and 170 V back voltages, to convert the x-axis in Figure 4.25 (b) and (d) to the corresponding injected charge. For the calibration has been implicitly assumed, given the laser intensity, that the generated charge in the DePFET pixel and in the diode is the same. This is not guaranteed because the unknown optical reflection losses of the two detectors, that can be obviously different. This affects the precision of the absolute value of the injected charge in the DePFET pixel, but not the conclusions presented in the following because the optical reflection losses are independent on the two probed injection modalities.

Figure 4.26 shows the dependence of the signal amplitude on the charge injection level in the two probed modalities, for different back voltages and for different amounts of charge ($14.7 \cdot 10^3$ and $28.2 \cdot 10^3$ electrons) delivered with a single pulse in the *burst of pulses* modality. The roll-back of the signal amplitude may be explained with the spill of the generated charge in a first over-flow region located at the center of the DePFET. As soon as even this overflow region is filled, the signal amplitude starts rising again but with a smaller slope as a function of the injected charge because the charge generated is accumulated not only in the internal gate where the induction effect with the channel is maximum but also in the central region where the induction is less efficient. The impact of the two charge injection techniques on the DePFET amplitude response can be summarized as

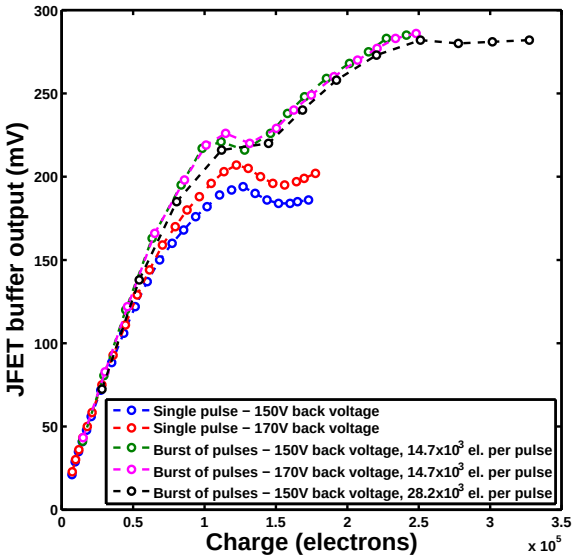


**Figure 4.26:** *Amplitude response of the DePFET pixel for the two probed injection modalities as a function of the injected charge. These curves shown the effect of different parameters such as the back voltage and the amount of charge delivered with a single pulse in* burst of pulses *injection modality.*

follows:

- the curves are superimposed at low level of charge injection, no difference appears between the two techniques, but, two different curves have been measured at high level of charge injection. The DePFET shows a higher value of the so-called charge transconductance $g_{mq}$ (i.e. the ratio between output signal amplitude and injected charge) in the *burst of pulses* injection modality, as should be evident by a comparison of the blue curve (*single pulse*) with the black or the green one (*burst of pulses*) for the 150 V back voltage or comparing the red curve with the magenta one for the 170 V back voltage;

- the amplitude response depends on the back voltage in the *single pulse* injection modality, in particular at high level of charge injection the pixel charge transconductance is higher at 170 V back voltage, as can be deduced from the comparison of the blue curve with the red one. In *burst of pulses* injection modality the amplitude response is quite independent on the back voltage, the green curve and the magenta one, that differ just for the back voltage being the amount of charge

delivered with a single pulse the same, are superimposed except for the roll-back region.

- the amplitude response is dependent on the amount of charge delivered with a single pulse in *burst of pulses* injection modality, in particular increasing the amount of charge the pixel charge transconductance decrease, as can be inferred from the comparison of the green curve with the black one.

The foreseen operation mode (at the European XFEL source) of the detector is the *single pulse* one, in fact during the readout phase of a burst of pulses every single pulse is readout separately. The effects on the amplitde response highlighted with the present test will reduce the possibilities of detector calibration, that can not be performed with a burst of pulses technique (that is a simple way to obtain a self calibrated source known the injected charge delivered by a single pulse).

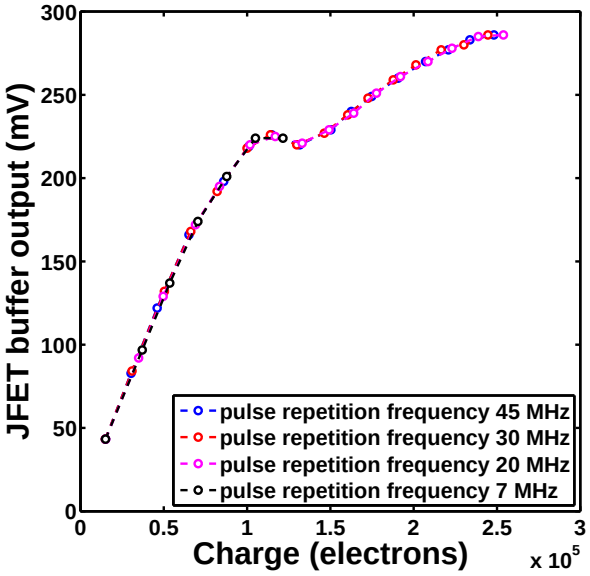


**Figure 4.27:** *Amplitude response of the DePFET pixel as a function of the injected charge for different burst rates.*

Finally also the dependence of the amplitude response on the pulse repetition rate in *burst of pulses* mode has been probed. Figure 4.27 shows the amplitude response, in case of 170 V back voltage, as a function of the injected charge for 4 pulse repetition rates, 45 MHz, 30 MHz, 20 MHz,

7 MHz, corresponding to a time separation of the pulses in a single burst of 22.2 ns, 33.3 ns, 50 ns and 143 ns respectively. The curves are superimposed in the whole injected charge range, resulting the amplitude response independent, in the probed range, on the pulse repetition rate.

#### 4.2.3.4 Single pulse response

The impact of the clear frequency on the operation of the device has been investigated over 3 orders of magnitude, from 10 Hz to 10 kHz. For each clear frequency, a set of waveforms has been acquired for five different levels of charge injection, from no charge injected to $1.25\times10^5$ electrons.

The IR laser ($\lambda$ = 905 nm) was focused on the detector back side, while the back contact voltage was set to 150 V. The DePFET matrix was instrumented with the voltage-mode front end electronics, but without the voltage preamplifier, so the output waveform has been digitized directly at the output of the nJFET buffer by a digital oscilloscope (Tektronix DPO4104, 8 bits, 1 GHz analog bandwidth, 5 GSamples/s sampling frequency).

Figure 4.28 shows a first set of acquired waveforms, in a wide time-scale, at two levels of charge injection (no charge and $5.4\times10^4$ electrons). These waveforms give quantitative information about the DC behavior of the DePFET, that depend on the average charge stored in the internal gate, which has an effect on the bias current of the device, hence on the nJFET buffer output signal. The stored charge increases the DePFET bias current therefore lowering the DC output level. The mean charge in the internal gate depend on three factors: the leakage current of the device, the clear frequency and the laser pulse intensity. The accumulation in the internal gate of the charge due to the collection of the leakage current causes the saw-tooth shape, clearly visible in the enlarged views. When the clear frequency is lower the DC level also decrease because the higher quantity of charge stored in the internal gate. Also the laser pulse play a role contributing to the mean charge collected in the internal gate, in fact, at a given clear frequency, the DC level is lower in the case of injected charge equal to $5.4\times10^4$ electrons. At the lowest clear frequencies (10 and 20 Hz) the saw-tooth shape is no more visible, this is a saturation effect, due to the ineffectiveness of the clear mechanism at this low frequencies.

Figure 4.29 shows a second set of waveforms, that are the same of the previous case but acquired in a shorter time- scale, in order to highlight the clear pulse, that is the big pulse with a duration of 1 $\mu$s, and the signal step caused by the laser injection occurring at t = 0 s, 4 $\mu$s after the clear pulse. The saw-tooth shape is obviously no more recognizable, on this short time the baseline is constant, however the leakage current effect is evident com-

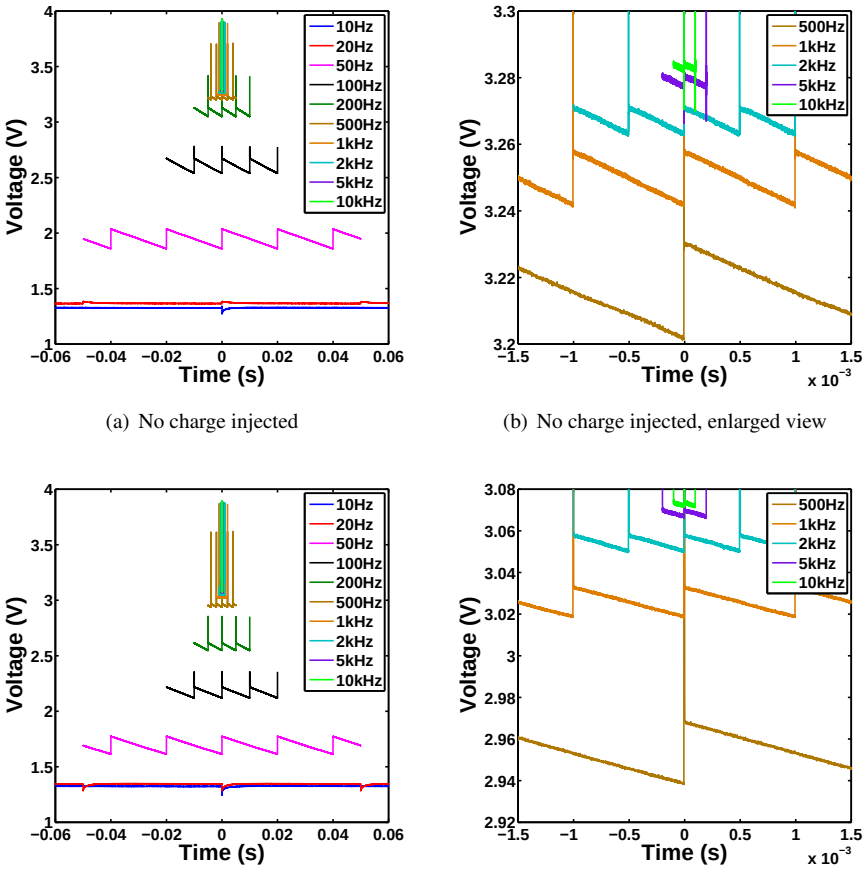


(a) No charge injected

(b) No charge injected, enlarged view

(c) $5.4\times10^4$ electrons

(d) $5.4\times10^4$ electrons, enlarged view

**Figure 4.28:** *Waveforms acquired as a function of the clear frequency and the injected charge, here showed in case of no charge injected (top) and in case of $5.4\times10^4$ electrons (bottom). The waveforms show the DC behavior of the DePFET, that depend on the average charge stored in the internal gate due to different effects such as the leakage current, clear frequency and the intensity of the laser pulse.*

paring the baseline on the right of the clear pulse after the laser injection and the DC level on the left of the clear pulse. From these waveforms the dependence of the amplitude of the signal step and of the DC level, calculated as the voltage level before the clear pulse, on the clear frequency has been derived.

The DC level, showed in Figure 4.30, is independent on both the clear frequency and the injected charge at lower frequencies, cause the aforementioned saturation effects. Increasing the clear frequency the DC level

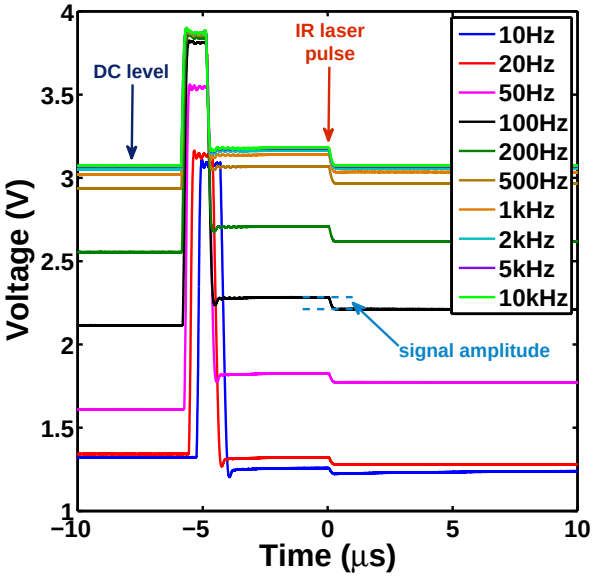


**Figure 4.29:** *Waveforms acquired as a function of the clear frequency and the injected charge, here showed in case of charge injected of $5.4\times10^4$ electrons. The DC level, IR laser shot time and the signal due to the injected charge are highlighted. The big pulse with a duration of 1 μs is the clear pulse and the IR laser pulse is injected 4 μs after the clear operation.*

shows an excursion of ∼2 V at low levels of injected charge, while at higher levels the excursion is less pronounced. Also a saturation effect of the DC level curves is noticeable at high clear frequency. An explanation of the behavior of the device can be provided. The average charge in the internal gate depends on two contributes, the accumulation of the leakage current, that is directly proportional to the clear period and the laser pulse intensity, independent on the clear frequency. At high clear frequency the integration time of the leakage current is reduced, hence the prevalent effect on the average charge stored in the internal gate is given by the intensity of the laser pulse. This is visible in the constant trend of the DC level curves at high clear frequency, with a saturation level dependent on the charge generated by the laser pulse and stored in the internal gate.

The signal amplitude, in Figure 4.31, gives information about the small signal behavior of the device as a function of the clear frequency. If there is a certain amount of charge already stored in the internal gate, than the signal charge from the laser pulse has a reduced impact on the device current. This is verified at low clear frequency, when there is a great leakage

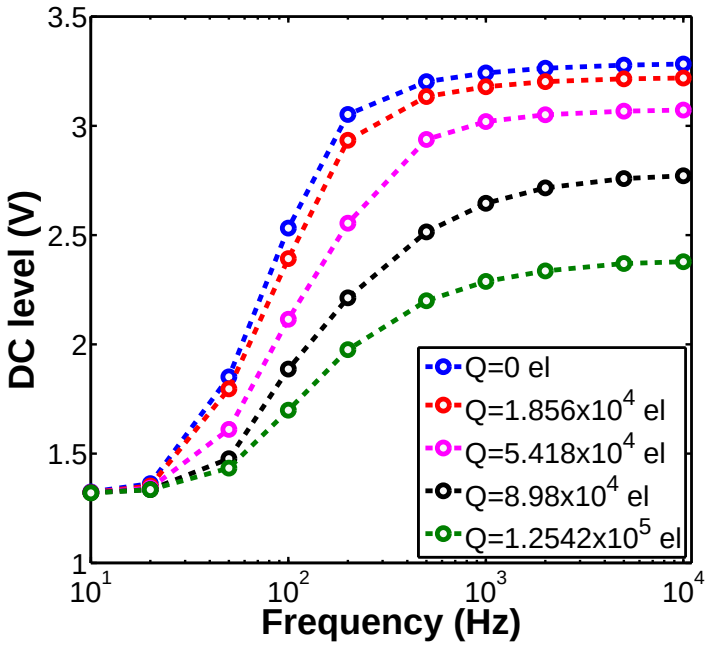


**Figure 4.30:** *DC level, calculated just before the clear pulse (see Figure 4.29), as a function of the clear frequency and for different levels of charge injection.*

current contribution, and means a lower amplitude signal. At higher clear frequency the leakage current contribution is negligible and the internal gate is empty when the laser pulse generated charge is collected, hence the signal amplitude is maximum and constant.

### 4.2.4 Test with mono-energetic proton beam

In order to widen the range of probed injection levels, the detector response has been measured in the case of interaction with mono-energetic 1 MeV protons during a beam time at the DEFEL beam line @ LABEC, Florence, Italy, in September 2011. The master trigger for the detector operation was provided by the predeflectors of the DEFEL beam line, responsible of the creation of the single proton bunches. Proton pulse, and hence clear, frequency was 200 Hz and the detector has been depleted with 170 V back voltage. The pixel under test was the (2,3), instrumented with the voltage readout electronics. The preamplifier output waveforms are digitized with a remotely controlled digital oscilloscope (Tektronix DPO4104, 8 bit) and acquired via ethernet by a dedicated Matlab® code.

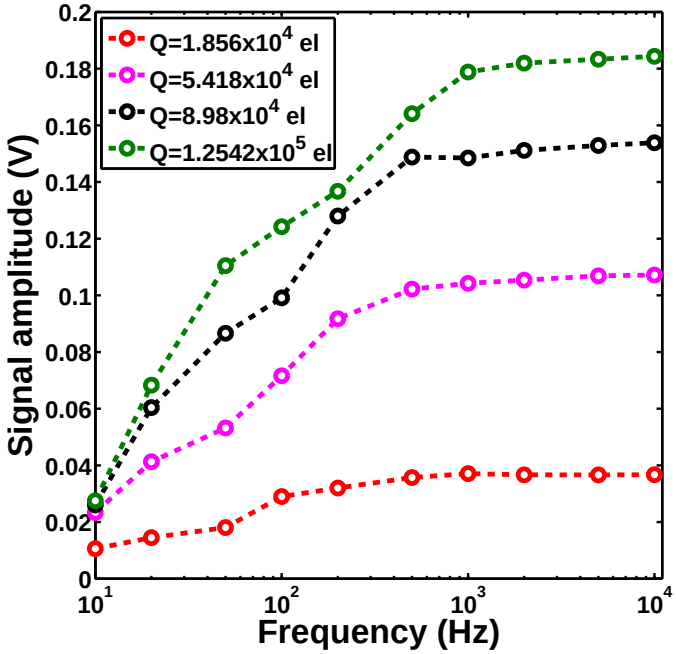


**Figure 4.31:** *Signal amplitude due to the laser pulse (see Figure 4.29), as a function of the clear frequency and for different levels of charge injection.*

Figure 4.32 shows the acquired waveforms at the voltage buffer output (no G = 10 voltage amplifier was inserted in the readout chain) in the case of full single 1 MeV proton collection (gathering of several curves) and in the case of charge sharing with neighbor pixels. Due to the spatial resolution of the proton beam (limited to $\sim$100 $\mu$m in the 2011) comparable with the pixel size (75 $\mu$m), the single proton interaction points spread all over the pixel area. Therefore only a small fraction of the collected events refer to full charge collection while a large percentage of the output waveforms at one pixel are related to split events.

The amplitudes of the digitized waveforms are computed off-line. Figure 4.33 shows the scatter plot of the waveform amplitudes versus the waveform number together with the histogram of the amplitudes.

A peak at a voltage of about 660 mV is visible, that could correspond to the full collection of single 1 MeV protons, the shoulder towards lower amplitudes relates to split events.

However the effectiveness of the test with mono-energetic protons has been clearly limited by the spatial properties of the proton beam with re-

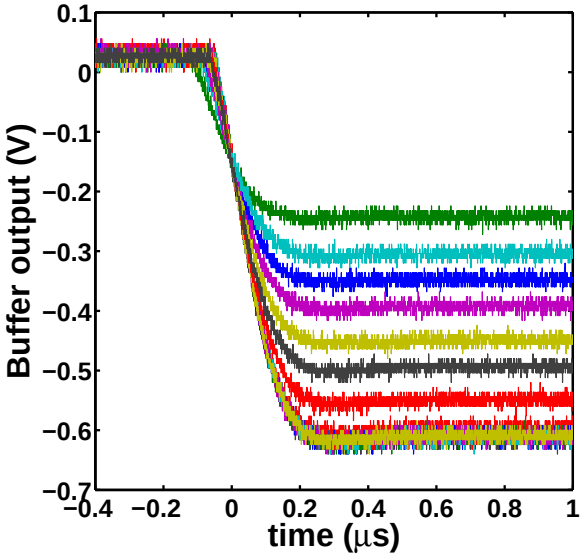


**Figure 4.32:** *Measured output waveforms of pixel (2,3) in case of 1 MeV proton interaction.*

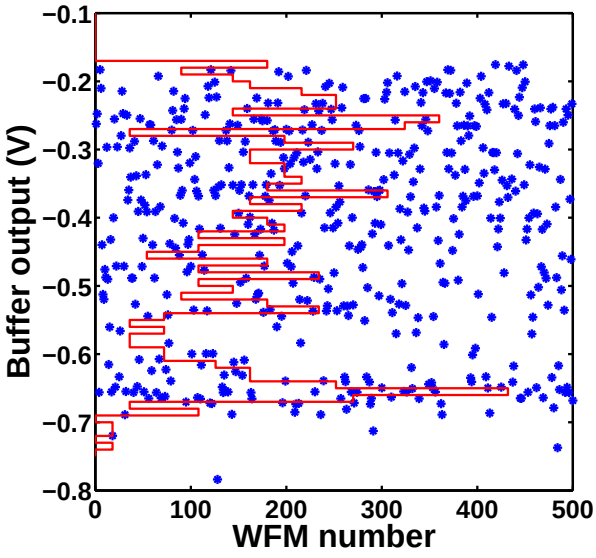


**Figure 4.33:** *Scatter plot of the amplitude of the acquired waveforms vs. the waveform number. The red line is the histogram of the measured amplitudes. The peak due to single 1 MeV protons collection and the shoulder due to split events are visible.*

spect to the small size of the pixel, but this is a useful example that point out how much important is the availability of a high resolution test probe. With the recent upgrade of the DEFEL beam line the spatial distribution of the proton beam has been narrowed to $\sim$10 $\mu$m allowing the exploration of lower spatial scale and it will be possible in the next future to perform a fine scan of the pixel response.

CHAPTER 5

# Conclusion and future perspectives

In this work a high - timing and spatial - resolution test suite, for radiation detectors characterization over a wide range of charge injection levels, has been presented. This suite is based on an infrared laser system for the lower charge levels and on mono-energetic proton bunches for the higher levels of charge injection.

The laser system has been expanded with new linear motorized stages, with the relative controller, in order to make it more flexible and adaptable to the test of different radiation detectors, and upgraded with the introduction of a new digital oscilloscope with sampling rate up to 5 GSample/s. This upgrade has required further development of the dedicated *control software* of the whole system, that has been moreover improved introducing the acquisition of the waveforms collected at the device under test readout chain output, digitized by means of the digital oscilloscope, for off-line analysis.

The spatial resolution of the DEFEL proton beam line has been upgraded with the installation of novel remotely controlled in-vacuum hi-resolution profiling slits, moreover a CMOS sensor has been installed as bi-dimensional beam monitor for beam quality and position assessment. The profiling slits are remotely controlled by means of a custom made con-

troller, that has been optimized in order to make it compatible with both slits equipped with incremental encoders and slits with motors unprovided of the encoders. The performances of the beam line have been qualified in terms of the proton energy calibration and time resolution, showing excellent results, and, after the upgrade, in terms of the spatial resolution. Regarding the spatial resolution a qualification of the spatial properties of the proton beam, by means of the CMOS sensor has been carried out, showing a good improvement with respect to the beam size obtained with the old profiling slits. However there is the possibility of further improvement of the spatial resolution and a future work is the optimization of the beam profile by means of a systematic study of the beam line parameters.

A great effort has been devoted to the implementation of a general purpose multichannel data acquisition system, 500 Msample/s 12 bit, capable of full shape digitization of the output signals coming out from multi output devices, like segmented or pixelated detectors. The management software has been developed in order to be as user friendly as possible and, at the same time, to give to the user the possibility of fully exploits the features offered by the sampling boards, in order to adapt the data acquisition system to different experimental conditions. A first satisfactory test of the developed system (hardware and software) has been carried out at the DEFEL beam line, however in this test the data transfer was not efficient, making the data acquisition system slow. This first negative result has pushed the efforts toward the optimization of the software, greatly enhancing the acquisition rate of the system in its later version. Up to now the system is well-functioning except the timestamp feature of one of the two modules of the system, that is affected by a malfunctioning when the module is externally clocked. This can be fixed by using the internal clock, however a future activity will be the the understanding and solving of this problem. In the future the system, limited to 8 channels by the available hardware, can be easily expanded with the insertion of additional sampling modules. This can be achieved thanks to the care taken in the development of the software, which is able to manage a system with an arbitrary number of boards (with reasonable limitations, for example the slot capability of the VME crate).

The developed suite has been probed through qualification campaigns on two relevant case studies:

- the Double Sided Silicon Strip Detectors (DSSSDs) used as first and second detection stages of the telescopes that constitute the FARCOS array. The calibration of the strip detectors in a wide range of charge injection levels, up to $\sim 3 \cdot 10^7$ electrons, achieved with 5 MeV pro-

ton bunches, has been carried out during a beam time at the DEFEL beam line, a great result that clearly shows the capability of the mono-energetic proton bunches as a powerful and absolute calibration tool. During the beam time also several scans have been performed across the strips, recording the full shape of the output waveforms. The shape can be investigated in order to assess the effect of the sharing phenomena, visible in case of inter-strip injection, on the pulse shape analysis capability of the particle identification system;

- a first prototype of a DSSC-type pixel matrix with DePFET readout. An experimental campaign has been carried out at low levels of charge generation (up to $\sim 10^5$ electrons) with the laser test suite (laser head with $\lambda$ = 905 nm). Bi-dimensional in-pixel mapping of the amplitude and the charge collection time of two pixel has been performed, showing an asymmetry between the amplitude and the collection time within the pixel.

  From one-dimensional fine scans, performed as a function of the back voltage and of the injected charge, the study of the pixel charge collection capability has been carried out.

  The impact of the clear frequency of the device on both the DC level and the signal amplitude has been investigated. In the probed frequency range these parameters are affected by the clear frequency at low frequency whereas show a saturation effect at high frequency.

  Finally the amplitude response has been qualified for two injection modalities (*single pulse* and *burst of pulses*), showing a different behavior at higher levels of charge injection for the two probed modalities, that are also affected in a different way by the applied back voltage. Moreover the amplitude response, in *burst of pulses* injection modality, depends on the charge delivered by a single pulse of the burst while seems to be unaffected, in the probed frequency range, by the time separation of the pulses. These effects on the amplitude response of the DePFET pixel will reduce the possibilities of detector calibration.

  A test has been carried out with mono-energetic 1 MeV protons at the DEFEL beam line, but ist effectiveness has been limited by the spatial properties of the proton beam.

  Future activities, regarding the characterization of the DePFET pixels, include further tests with the IR laser using the other available laser head with wavelength of $\lambda$ = 705 nm and pixel scans performed with

mono-energetic protons at the upgraded DEFEL beam line, in order to extend the probed range of charge injection levels and cover the ionization levels foreseen at the European XFEL.

# List of Figures

# List of Tables

# Bibliography


[1] C. Pellegrini, J. Stöhr, "X-Ray Free Electron Lasers: Principles, Properties and Applications," *Nucl. Instr. and Meth. A*, vol. 560, pp. 33–40, 2003.

[2] B. W. J. McNeil N. R. Thompson, "X-ray free-electron lasers," *Nature Photonics*, vol. 4, pp. 814–821, 2010.

[3] R. Bonifacio, L. De Salvo, P. Pierini, N. Piovella, and C. Pellegrini, "Spectrum, temporal structure, and fluctuations in a high-gain free-electron laser starting from noise," *Phys. Rev. Lett.*, vol. 73, pp. 70–73, Jul 1994.

[4] V. Ayvazyan et al., "Study of the statistical properties of the radiation from a VUV SASE FEL operating in the femtosecond regime," *Nucl. Instr. and Meth. A*, vol. 507, pp. 368–372, 2003.

[5] "Lcls conceptual design report," *SLAC-R-593*, vol. UC-414, 2002.

[6] http://www.xfel.eu/research/instruments/

[7] M. Altarelli, "The European X-ray free-electron laser facility in Hamburg," *Nucl. Instr. and Meth. B*, vol. 269, pp. 2845–2849, 2011.

[8] G. Grübel, "X-Ray Photon Correlation Spectroscopy at the European X-Ray Free-Electron laser (XFEL) facility," *C. R. Physique*, vol. 9, pp. 668–680, 2008.

[9] L. Strüder et al., "Large-format, high-speed, x-ray pnCCDs combined with electron and ion imaging spectrometers in a multipurpose chamber for experiments at $4^{th}$ generation light sources," *Nucl. Instr. and Meth. A*, vol. 614, pp. 483–496, 2010.

[10] M. Porro, "Development of the DEPFET Sensor with Signal Compression: a Large Format X-ray Imager with Mega-Frame Readout Capability for the European XFEL," *IEEE Nuclear Science Symposium Conference Record*, pp. 1424–1434, 2011.

[11] www.cxro.lbl.gov

[12] L. Strüder, P. Holl, G. Lutz, J. Kemmer, "Device modeling of fully depletable CCDs," *Nucl. Instr. and Meth. A*, vol. 253, pp. 386–392, 1987.

[13] G. Potdevin, U. Trunk, H. Graafsma, "Performance simulation of a detector for 4th generation photon sources: The AGIPD," *Nucl. Instr. and Meth. A*, vol. 607, pp. 51–54, 2009.

[14] B. H. et al., "The adaptive gain integrating pixel detector AGIPD a detector for the European XFEL," *Nucl. Instr. and Meth. A*, vol. 633, pp. S11–S14, 2011.

[15] Andrew Blue, M. French, P. Seller, V. O'Shea, "Edgeless sensor development for the LPD hybrid pixel detector at XFEL," *Nucl. Instr. and Meth. A*, vol. 607, pp. 55–56, 2009.

[16] J. Kemmer, G. Lutz, "New detector concepts," *Nucl. Instr. and Meth. A*, vol. 253, pp. 365–377, 1987.

[17] G. Lutz, P. Lechner, M. Porro, L. Strüder, G. De Vita, "DEPFET sensor with intrinsic signal compression developed for use at the XFEL free electron laser radiation source," *Nucl. Instr. and Meth. A*, vol. 624, pp. 528–532, 2010.

[18] M. Porro et al., "Expected performance of the DEPFET sensor with signal compression: A large format X-ray imager with mega-frame readout capability for the European XFEL," *Nucl. Instr. and Meth. A*, vol. 624, pp. 509–519, 2010.

[19] Y. Blumenfeld, "Radioactive ion beam facilities in Europe," *Nucl. Instr. and Meth. B*, vol. 266, pp. 4074–4079, 2008.

[20] H. Sakurai, "Present and future radioactive ion beam facilities in the Middle East and East," *Nucl. Instr. and Meth. B*, vol. 266, pp. 4080–4085, 2008.

[21] A. Lépine-Szily et al., "Scientific program of the Radioactive Ion Beams Facility in Brasil (RIBRAS)," *Nucl. Instr. and Meth. A*, vol. 834, pp. 491c–494c, 2010.

[22] C. Konrad Gelbke, "NSCL-Ongoing activities and future perspectives," *Prog. Part. Nucl. Phys.*, vol. 62, pp. 307–312, 2009.

[23] M. S. Wallace et al., "The high resolution array (HiRA) for rare isotope beam experiments," *Nucl. Instr. and Meth. A*, vol. 583, pp. 302–312, 2007.

[24] B. Davin et al., "LASSA: a large area silicon strip array for isotopic identiï¬¬$cationofchargedparticles,''$ $Nucl.Instr.andMeth.A, vol.$ $473, pp.$ $302 - -318, 2001.$

[25] http://pro.ganil-spiral2.eu/laboratory/detectors/charged-particles/must2/

[26] Y. Blumenfeld, "MUST: A silicon strip detector array for radioactive beam experiments," *Nucl. Instr. and Meth. A*, vol. 421, pp. 471–491, 1999.

[27] E. Pollacco et al., "MUST2: A new generation array for direct reaction studies," *Eur. Phys. J. A*, vol. 25, pp. 287–288, 2005.

[28] E. Pollacco et al., "MUST II: Large solid angle light charged particle telescope for inverse kinematics studies with radioactive beams.," *AIP Conf. Proc.*, vol. 680, pp. 313–316, 2003.

[29] A. Castoldi, C. Guazzoni, "Impact of detector parameters on light charged particle and intermediate mass fragments identification through pulse-shape analysis," *Nucl. Instr. and Meth. A*, vol. 624, pp. 317–320, 2010.

[30] M. Alderighi et al., "Charge Identification in Large Area Planar Silicon Detectors, Using Digital Pulse Shape Acquisition," *IEEE Trans. Nucl. Sci.*, vol. 53, no. 1, pp. 279–285, 2006.

[31] S. Aiello et al., "Chimera: a project of a 4Π detector for heavy ion reactions studies at intermediate energy," *Nucl. Phys. A*, vol. 583, pp. 461–464, 1995.

[32] A. Pagano et al., "Fragmentation studies with the CHIMERA detector at LNS in Catania: recent progress," *Nucl. Phys. A*, vol. 734, pp. 504–511, 2004.

[33] Emilio Gatti, Antonio Longoni, Pavel Rehak, Marco Sampietro, "Dynamics of electrons in drift detectors," *Nucl. Instr. and Meth. A*, vol. 253, pp. 393–399, 1987.

[34] P.A. Tove, W. Seibt, "Plasma effects in semiconductor detectors," *Nucl. Instr. and Meth.*, vol. 51, pp. 261–269, 1967.

[35] Julian Becker, Klaus Gärtner, Robert Klanner, Rainer Richter, "Simulation and experimental study of plasma effects in planar silicon sensors," *Nucl. Instr. and Meth. A*, vol. 624, pp. 716–727, 2010.

[36] Gerhard Lutz, *Semiconductor Radiation Detectors*. Springer-Verlag, 2007.

[37] Glenn F. Knoll, *Radiation Detection and Measurement (3rd Edition)*. New York: John Wiley Sons, Inc., 2000.

[38] D. Mezza, "Mappatura delle proprietÃ  di trasporto e deconvoluzione del profilo della nuvola elettronica in rivelatori a deriva multilineari," *Master Thesis, Politecnico di Milano*, 2009.

[39] Simon Ramo, "Current Induced by Electron Motion," *Proc. IRE*, vol. 27, pp. 584–585, 1939.

[40] G. Rizzo et al., "Self-consistent optical parameters of intrinsic silicon at 300 K including temperature coefficients," *Sol Energ Mat Sol C*, vol. 92, pp. 1305–1310, 2008.

[41] http://www.srim.org/

[42] P. A. Mandó, "INFN-LABEC, Nuclear Techniques for Cultural Heritage and Environmental Applications," *Nuclear Physics News*, vol. 19, pp. 5–12, 2009.

[43] F. A. Mirto, L. Carraresi, "The pulsed beam facility at the Tandetron accelerator in Florence," *Nucl. Instr. and Meth. B*, vol. 266, no. 10, pp. 2113–2116, 2008.

[44] A. Castoldi, C. Guazzoni, D. Mezza, G. V. Montemurro, L. Carraresi, F. Taccetti, "Upgrade of the DEFEL proton beam line for detector response mapping," *2013 IEEE Nuclear Science Symposium and Medical Imaging Conference, N46-7, Seoul, South Korea, Oct. 27 - Nov. 2*, 2013.

[45] L. Acosta et al., "FARCOS, a new array for femtoscopy and correlation spectroscopy," *EPJ Web of Conferences*, vol. 31, pp. 1–8, 2012.

[46] L. Acosta et al., "FARCOS: a versatile and modular Femtoscopy Array for Correlation and Spectroscopy," *IEEE Nuclear Science Symposium Conference Record*, pp. 1547–1553, 2012.

[47] L. Acosta et al., "Mapping the Amplitude and Position Response of Double Sided Silicon Strip Detectors with Monochromatic Single Protons," *IEEE Nuclear Science Symposium Conference Record*, pp. 1358–1364, 2012.

[48] http://www.micronsemiconductor.co.uk/

[49] A. Castoldi, C. Guazzoni, T. Parsani, F. Riccio, P. Zambon, C. Boiano, L. Carraresi, F. Taccetti, L. Acosta, G. Cardella, T. Minniti, G. Verde, L. Quattrocchi, A. Trifiró, "Experimental Investigation of the Impact of Inter-Strip Incidence on the Signal Shape in Double Sided Silicon Strip Detectors for Particle Identification," *2013 IEEE Nuclear Science Symposium and Medical Imaging Conference, N26-4, Seoul, South Korea, Oct. 27 - Nov. 2*, 2013.

[50] M. Porro, "DEPFET Detector-Amplifier Structure: Properties, Achievements and New Developments, Concepts and Applications," *IEEE Nuclear Science Symposium Conference Record*, pp. 988–994, 2007.

[51] Chen Zhang et al., "Development of X-type DEPFET Macropixel detectors," *Nucl. Instr. and Meth. A*, vol. 588, pp. 389–396, 2008.

[52] Stefan Rummel, Ladislav Andricek, "The DEPFET active pixel sensor for vertexing at ILC and Super KEKB," *Nucl. Instr. and Meth. A*, vol. 623, pp. 189–191, 2010.

[53] J. Treis et al., "MIXS on BepiColombo and its DEPFET based focal plane instrumentation," *Nucl. Instr. and Meth. A*, vol. 624, pp. 540–547, 2010.

[54] Stefan Wölfel et al., "Sub-electron noise measurements on repetitive non-destructive readout devices," *Nucl. Instr. and Meth. A*, vol. 566, no. 2, pp. 536–539, 2006.

[55] A. Castoldi, C. Guazzoni, P. Lechner, D. Mezza, G. Montemurro, L. Carraresi, F. Taccetti, "Mapping of the response function of DePFET-based pixel sensors at different levels of charge injection," *IEEE Nuclear Science Symposium Conference Record*, pp. 1747–1753, 2011.

[56] M. Porro et al., "Spectroscopic Performance of the DePMOS Detector/Amplifier Device With Respect to Different Filtering Techniques and Operating Conditions," *IEEE Trans. Nucl. Sci.*, vol. 53, no. 1, pp. 401–408, 2006.

[57] Albert Thompson, Ingolf Lindau, David Attwood, Yanwei Liu, Eric Gullikson, Piero Pianetta, Malcolm Howells, Arthur Robinson, Kwang-Je Kim, James Scofield, Janos Kirz, James Underwood, Jeffrey Kortright, Gwyn Williams, Herman Winick, *X-Ray data booklet*. Lawrence Berkeley National Laboratory, 2009.